THE HEAT AND SALT BALANCES OF THE UPPER OCEAN BENEATH A SPATIALLY VARIABLE MELTING SEA ICE COVER

Daniel Reiner Hayes

A dissertation submitted in partial fulfillment of the
requirements for the degree of

Doctor of Philosophy

University of Washington

2003

Program Authorized to Offer Degree: Oceanography

ProQuest Information and Learning Company
300 North Zeeb Road
P.O. Box 1346
Ann Arbor, MI 48106-1346

In presenting this dissertation as a partial fulfillment of the requirements for the Doctoral degree at the University of Washington, I agree that the Library shall make its copies freely available for inspection. I further agree that extensive copying of the dissertation is allowable only for scholarly purposes, consistent with "fair use" as prescribed in the U.S. Copyright Law. Requests for copying or reproduction of this dissertation may be referred to Bell and Howell Information and Learning, 300 North Zeeb Road, Ann Arbor, MI 48106-1346, to whom the author has granted the "right to reproduce and sell (a) copies of the manuscript in microform and/or (b) printed copies of the manuscript made from microform."

Signature Dan Hayes

Date 7/31/03

University of Washington
Graduate School

This is to certified that I have examined this copy of a doctoral dissertation by

Daniel Reiner Hayes

and have found that it is complete and satisfactory in all respects,
and that any and all revisions required by the final
examining committee have been made.

Chair of Supervisory Committee:

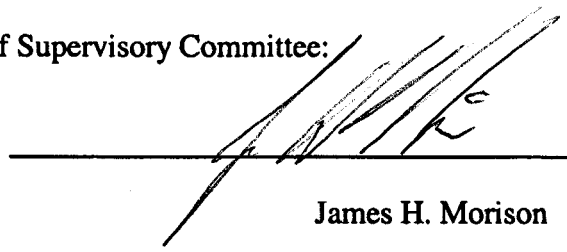

James H. Morison

Reading Committee:

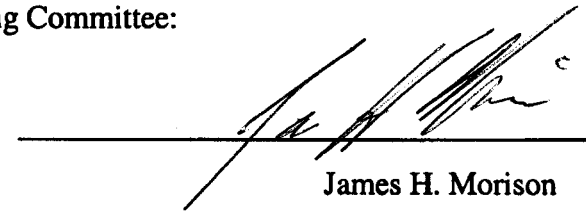

James H. Morison

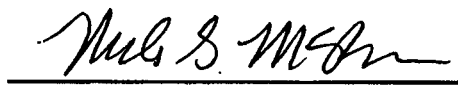

Miles G. McPhee

Peter B. Rhines

Date: 7/31/03

University of Washington

ABSTRACT

THE HEAT AND SALT BALANCES OF THE UPPER OCEAN BENEATH A SPATIALLY VARIABLE MELTING SEA ICE COVER

Daniel Reiner Hayes

Chairperson of the Supervisory Committee: Affiliate Professor James H. Morison
School of Oceanography

The aim of this study is to paint a picture of the evolution of the horizontally variable ice-ocean boundary layer throughout summer. Observations were made during the drifting Surface HEat Balance of the Arctic (SHEBA) experiment in the summer of 1998. The ice-ocean boundary layer near leads is studied with an Autonomous Underwater Vehicle (AUV) and a novel technique to use vehicle motion data to calculate turbulent vertical water velocity along the vehicle path. Vertical fluxes are obtained and extend from the energy-containing wavenumber range and continue into the inertial subrange. This study is the first to measure horizontal profiles of turbulent fluxes in the ice-ocean boundary layer. AUV data are used in conjunction with fixed-mast turbulent fluxes at discrete levels in the boundary layer, Conductivity-Temperature-Depth data (vertical casts and lead surveys), and a suite of measurements made by other investigators.

The results indicate that scalars and their fluxes, as well as vertical stability, varied in the horizontal direction. AUV run-averaged turbulent stress in the boundary layer agrees well with the free-drift estimate. In early summer, fluxes were weak as ice velocity was low, and fresh meltwater was trapped at the

upper ice surface. Also, surface melt was directed into leads rather than entering the ocean uniformly, resulting in a highly stable fresh layer. Near the end of July, a storm flushed leads, and the mixed layer freshened and deepened. The AUV observed strong fluxes under and downstream of rough, ridged ice. After the storm, heat and salt fluxes were strongest under leads.

The results are simulated with 1-D and 2-D time-varying numerical models. The 1-D model produces a shallow, overly fresh mixed layer during the storm period. Simulations from the 2-D model suggest that both mechanical forcing from ice topography and a dynamic instability near downstream lead edges may enhance vertical mixing. AUV data agree well with the 2-D model after the storm and suggest mechanical forcing is important. The timing and strength of meltwater flux and the horizontal variability in interfacial fluxes have implications on large scales through the seasonal cycle of mixed layer depth and the surface heat budget.

TABLE OF CONTENTS

LIST OF FIGURES

LIST OF TABLES

ACKNOWLEDGEMENTS

I would like to thank Jamie Morison for initiating and sustaining this research project and inviting me to work on it. Thank you to Miles McPhee for sharing ideas, numerical model code (1-D), SHEBA data (CTD, TIC, ice velocity and more), and even instruments (lead TIC). Peter Rhines introduced me to laboratory experiments and provided an excellent teaching assistant experience. All three were also members of the reading committee. John Wettlaufer supported my work and intellectually stimulated me on a wide range of topics. Thanks to Mark Warner and Stephen Warren for being on the doctoral committee. David Smith provided the original 3-D model with support and encouragement.

Thanks to the Polar Science Center: Mark Ortmeyer, Wendy Ermold, Rebecca Woodgate, Mike Steele, Knut Aagaard, Roger Anderson, Bonnie Light, Jinlun Zhang, Sue Huney, Mari Forster, and many others for technical, scientific and moral support. Other APL staff were helpful: Don Percival and Bradley Bell in developing the Kalman Smoother; Russ Light and John Elliot in developing the AMTV. Russ was also kind enough to reveal his "Arctic humor" at SHEBA.

Thanks to: Hajo Eicken and Don Perovich for helping me learn about sea ice, the crew of the *CCGS Des Groseilliers* for support during SHEBA, the SHEBA Project Office (Dick Moritz) for providing the wind and radiation data, and David Morison for collecting lead TIC data.

Thank you to the financial supporters of this project and my graduate studies: the Office of Naval Research, the National Science Foundation, the Applied Physics Laboratory, and National Defense Industrial Association (tuition scholarship). Thank you to Adrian Jenkins and the British Antarctic Survey for support and flexibility in the final weeks.

Finally, I would like to express deep gratitude to my family and friends for all of their support, especially my wife Sophia (who also helped with figures). Special thanks go to my parents for encouraging my math and science education as well as a general desire to learn.

DEDICATION

To Sophia and Constantinos, sorry I wasn't home earlier.

1. INTRODUCTION

This study investigates the redistribution of thermal energy and fresh meltwater entering the planetary boundary layer of the Arctic Ocean in summer. The fluxes of heat and salt at the ocean surface vary greatly over distances as small as a few meters. While openings in sea ice (leads) typically only cover a few percent of the surface, they are responsible for much of the energy exchange of the ocean and atmosphere during winter [*Badgley*, 1966; *Maykut*, 1978]. Because ice forms in the leads during winter, they are also sites of the strongest brine rejection. In summer, leads are the "windows to the ocean" since they absorb over 90% of the incident solar radiation, compared to transmittances of less than 5% for bare ice surfaces (even less for snow-covered ice, more for ponded ice; see *Light et al.* [2003]). The manner in which fresh water from snow and ice melt enters the ocean is dependent on the ice permeability, which varies considerably over the summer and within a single floe [*Eicken et al.*, 2002]. The latter study also finds that ice permeability also affects the coverage of melt ponds, which in turn contributes to the variability of transmittance.

Numerical models of the planetary boundary layer generally assume horizontal homogeneity, a poor assumption for ice-covered regions in light of the variability due to leads and different ice types. In large-scale Arctic and global models, the fine scale structure of the ice cover cannot be resolved, so parameterization of the effects of spatial variability is required. Parameterization is impossible without measurements and understanding. For example, a naïve parameterization of surface salt budget during winter freeze up might be to assume that the saline water formed in leads is uniformly distributed throughout the mixed layer. However, wintertime lead convection has been observed to be highly variable, depending on ice speed and surface buoyancy (salt) flux [*Morison et al.*, 1992]. In typical Arctic conditions, one may observe either a "free convection" or a "forced convection" regime. In the latter case, the mixed layer becomes more saline and remains well-mixed, with a potential to deepen the

mixed layer under strong surface stress. The uniform mixing parameterization is reasonable. Under the "free convection" regime in which ice speeds are low, saline plumes do not blend into the mixed layer uniformly, but sink to the mixed layer base, perhaps decreasing the mixed layer depth. The uniform mixing parameterization qualitatively fails. This phenomenon has been simulated with a two-dimensional numerical model [*Smith and Morison*, 1998] and is consistent with observations [*Morison and McPhee*, 1998]. It is a direct result of spatial variability of surface buoyancy flux: if the total salt rejection were distributed uniformly over the surface instead of focused in leads, it would be much weaker, and the criterion for convective instability would not be met. That is, the lead number of *Morison et al.* [1992] or the Rayleigh number modified for turbulent diffusivities as in *Smith and Morison* [1998] would be too small. The effect of a strong flux in a relatively small region is not the same as a weaker flux over a proportionately broader region. Without measurements of the horizontal variability in the mixed layer, it would be difficult to assert that wintertime lead convection results in a shallower, more stratified mixed layer.

The effect of horizontally variable fluxes on the planetary boundary layer has not been studied in detail for the stable case. Horizontal variability of ice-ocean heat flux over a portion of a single floe (less than 1 km^2) has been discussed by *Wettlaufer* [1991]. He attributes the variability to coupling of topographic features with the structure of the boundary layer turbulence. It has long been known that the ice underside is not uniform but consists of relatively smooth areas punctuated by ridges and rubble fields. It is, of course, known that these features affect the momentum transfer from the ice to the ocean via form drag [*Steele et al.,* 1989], and that variation in ice roughness leads to widely variable estimates of Reynolds stress at a given depth [*Morison et al.,* 1987]. While the variation in ice roughness is important in the overall ice-ocean momentum transfer and ice-ocean heat flux, the variability in boundary conditions due to open water during summer is even larger. As will be discussed, the effect of summer leads on the planetary

boundary layer is also relevant in large-scale and climate studies of the Arctic, and the measurements and models presented here are relevant to those studies.

It is well established that solar radiation through leads in summer warms the polar ocean mixed layer [*Maykut and Perovich,* 1987; *Ebert and Curry*, 1993; *Maykut and McPhee*, 1995]. However, the exact fate of this thermal energy is essentially unknown. It appears that much of the energy often goes into melting of sea ice [*Maykut and Perovich*, 1987; *Maykut and McPhee*, 1995; *Holland et al.,* 1997; *Nihashi and Ohshima*, 2001], but the proportion between basal and lateral melting of floes is unclear, or more generally, the distribution of melting among the thickness classes is unclear. The quantity and residence time of thermal energy stored in the ocean is also unclear, although *Maykut and McPhee* [1995] show that this is important. The spatial distribution of thermal energy in the Arctic Ocean on relatively small scales is important in understanding the evolution of the sea ice cover. Because water heated by the sun often melts ice, which generally allows more heating (the ice-albedo feedback), it is important to understand if, where, and when the energy absorbed by the ocean is released.

The ice-albedo feedback is an example of how spatially varying fluxes in the ocean boundary layer can have large-scale, long-time significance. The ice-albedo feedback needs to be better understood for accurate modeling of the Arctic sea ice cover evolution under climate change scenarios [*Curry et al.*, 1995; *Perovich et al.*, 2002a and references therein]. A global climate model (GCM) shows the mode of the response to increased greenhouse gas concentrations of ocean to ice heat transfer (a heated mixed layer, heated leads, or heated ice) has a large influence on ice extent in the Northern Hemisphere [*Rind et al.*, 1995]. One-dimensional models also illustrate the importance of ice-albedo feedback. *Holland et al.* [1997] show that the ice thickness distribution (particularly the lead and first-year ice portion) has a large effect in their model in summer because of the solar heating it allows and the resulting ice melt. They report that ignoring ice

thickness variability or decoupling the ice thickness distribution from ocean conditions will result in an inaccurate response to general model forcing.

The Arctic influence on the global climate also depends upon the correct treatment of the storage and release of thermal energy by the upper ocean [*Uttal et al.*, 2002; *Randall et al.*, 1998]. In many global circulation models, increased atmospheric CO_2 results in above-average warming in the polar regions due to less extensive and thinner sea ice, known as polar amplification (e.g. *Manabe et al.* [1991]). The warming (among other things) varies widely among models due to the models' inability to accurately simulate near-surface temperature structure and energy exchange [*Randall et al.*, 1998]. Sea ice feedbacks have been shown to play a major part in the global simulations [*Rind et al.*, 1995] and play a part in the polar amplification of climate warming trends [*Manabe et al.*, 1991].

Changing conditions in the Arctic since about 1990 have added urgency to understanding the storage and release of thermal energy in the upper ocean. The *SEARCH Scientific Steering Committee* [2001] describes pan-Arctic change in the atmosphere, ice, ocean, and land both over the last decade and over the last several decades. Some of the postulated changes most relevant to this study are the 43% reduction in mean sea ice thickness [*Rothrock et al.*, 1999], the change in atmospheric pressure (mean and spatial pattern) [*Walsh et al.*, 1996; *Serreze et al.*, 2000], a longer melt season [*Smith*, 1998], and a warmer, fresher upper ocean [*McPhee et al.*, 1998]. *Proshutinsky and Johnson* [1997] find that two modes of wind-driven ice and ocean circulation exist (cyclonic and anticyclonic) in numerical studies. The seasonal cycles in these two regimes are very different, and *Polyakov et al.* [1999] argue that the current Arctic climate state is a cyclonic regime that in their model causes more summer leads and increased ice export out of Fram Strait. The more divergent ice pack allows more open water and absorption of solar radiation, potentially giving the ice-albedo feedback more influence. The result in the numerical model is a warmer upper ocean, a longer melt season, and thinner, weaker, less extensive sea ice cover, in agreement with

observations, particularly in the Canadian Basin. In fact, there has even been conjecture that an observed shift in Arctic atmospheric circulation could enhance melting to the point of a drastically different sea ice regime [*McPhee et al.*, 1998].

The evolution of the Arctic sea ice cover is not only important for the surface energy exchange of the Northern Hemisphere, but also for its effect on the world ocean. Sea ice export ultimately freshens the upper waters of the sub-Arctic seas. The amount and distribution of fresh water in the sub-Arctic likely affects the location and strength of overturning thermohaline circulation in the Atlantic Ocean [*Aagaard and Carmack*, 1989; *Carmack*, 2000]. The thermohaline circulation is a major component of the global heat budget since it is responsible for a large fraction of the global poleward heat transport.

Despite the importance of the ice-albedo feedback, it has been difficult to study due to the sparse observations complicated by strong horizontal variability in ice conditions and horizontal advection in the ocean. In their study of ocean heat storage and release, *Maykut and McPhee* [1995] were unable to account for lateral melting, effects of melt ponds, and lateral advection of water heated far away from the experimental site. They were still able to conclude that the majority of oceanic heat flux to the ice in the central Arctic comes from solar heating of the mixed layer. The Surface Heat Balance of the Arctic Ocean (SHEBA) was designed to improve understanding of physical processes controlling the vertical and horizontal exchanges of energy in the ocean-ice-atmosphere system [*Uttal et al.*, 2002]. The SHEBA experiment was executed from the Canadian Coast Guard ship, the *Des Groseilliers*, which was "docked" in an ice floe in the Beaufort Sea in September of 1997. It was allowed to drift with the floe until September of 1998. The ship provided a base for an extensive program of meteorological, snow and ice, and oceanographic measurements. The field program provided an excellent platform on which to carry out a summer lead study, both scientifically and logistically. Ultimately, the goal of SHEBA is to improve Arctic climate models by improving parameterizations of the physical

processes governing surface energy exchange. As illustrated above, without detailed observations on small spatial scales, the physical processes such as the ice-albedo feedback would remain a mystery. The present study, while suffering some of the previous problems, presents new information and insights on the planetary boundary in the summer Arctic.

The net effect of the observed melting patterns on the aggregate scale (order 100 km) is very difficult to estimate, not only because of strong variability of surface conditions on much smaller scales, but because of the unknown role of mixed layer heating and complex ice-ocean interactions on small scales. It is known that the thermal energy of the mixed layer is not strictly dependent on the local history of lead fraction [*Maykut and McPhee*, 1995]. The relative motion of ice and ocean give rise to a horizontally variable distribution of mixed layer temperature often independent of the local rate of heating. Since the oceanic heat flux to the ice depends both on mixed layer temperature elevation above freezing and local stress, horizontal gradients in heat flux can be large. Indeed, *Wettlaufer* [1991] observed horizontal variability in Arctic sea ice melt rate (proportional to oceanic heat flux) on scales between 10 cm and 100 m. Not only is the oceanic absorption of solar radiation strongly variable between ice and open water, but surface roughness changes drastically among first-year ice, multi-year ice, under-ice melt ponds, and leads.

The small-scale horizontal variability in upper ocean properties and ice roughness during the melt season has not been observed until now. Horizontal variability has been measured on the top surface of the ice, both in regard to thermal and mass balance. Ice draft has been collected along stake lines and with submarine-mounted echo sounders, but until now no high resolution transects of ice draft were available. Temperature, salinity, and optical properties have been collected in leads, but until now have not been related to the surrounding mixed layer. Heat fluxes at discrete depths in the mixed layer have been measured at discrete locations on the ice with turbulence sensors, but the dependence of ocean

heat flux on horizontal position and surface type has not been studied until now. Vertical profiles of ocean temperature and salinity in the mixed layer have been collected during the summer, but tell an incomplete story because they can suffer from the unknown effects of advection into different water mass systems and do not shed light on mixed layer horizontal structure. All of these improvements in studying the ice-ocean system are made possible in this study by use of an Autonomous Underwater Vehicle (AUV).

With new measurement technology come complications and opportunities in data interpretation. For the present study, an AUV has been developed for the measurement of ice draft, small signals of temperature and salinity and their fluxes in the polar mixed layer. The first attempt at taking under-ice horizontal profiles of temperature, salinity, and their turbulent fluxes with an AUV was a wintertime study by *Morison and McPhee* [1998]. The concept proved useful, and valuable scientific and technical insight were gained. An improved technique for estimating turbulent flux from AUV platforms has been developed for this study. The new technique and instrument allow collection of a unique data set pertaining to the distribution of thermal energy, salt, and even momentum in the summertime Arctic mixed layer.

This dissertation addresses Arctic mixed layer evolution and interaction with the surface during the summer melt season with AUV and other SHEBA observations and with numerical simulations. Section 2 describes the observational study, including methods used to observe the upper ocean and ice system, the observations themselves, and a brief discussion of the most important results which motivates the numerical studies in section 3. Both one-dimensional and two-dimensional models are used to simulate various conditions and to compare to observations. Section 4 provides a summary of the SHEBA summer story, with input from observations and simulations. Implications of this work on larger scales as well as future work and improvements are discussed.

2. OBSERVATIONAL STUDY

2.1 GENERAL DESCRIPTION

With the success of the Autonomous Conductivity Temperature Vehicle (ACTV) in the winter Lead Experiment (March and April 1992; see *LeadEx Group* [1993]) the idea of pursuing the study of spatial variability in the planetary boundary layer in the summer case was the logical next step. Very little is known of the effect of spatial variability on a boundary layer stabilized by buoyancy flux in small patches and bounded by a surface of variable roughness. The solar heat flux is also horizontally variable, and the resulting spatial pattern of ice melt is unknown. Besides an AUV, other techniques to measure horizontal profiles of the under-ice boundary layer do not exist.

The summer lead sampling strategy is based on previous experience with autonomous vehicles in the polar mixed layer. In LeadEx, *Morison and McPhee* [1998] used a complimentary system of fixed and mobile sensors to characterize the effects of unstable convection from leads. The set of fixed sensors (turbulence instrument clusters or TICs) was placed at a lead's edge, while the ACTV traveled back and forth at several depths under the lead of interest and surrounding ice. The ACTV and cluster data showed similar flow statistics when the ACTV was upstream and at about the same depth as the cluster. In particular, salinity and temperature spectra from the two instruments showed good agreement and a wavenumber, k, dependence proportional to $k^{-5/3}$. The TIC observations were in this sense "ground-truth" and allowed the ACTV to accurately map the spatial variability of fluxes in areas not upstream of a TIC.

Figure 2.1 shows the typical summer sampling strategy, along with many of the instruments used in this study. Since the buoyancy flux is typically stabilizing and therefore suppresses mixing, the depths of the mixed layer and fully-developed turbulence are much shallower than in winter. In fact, they are often on the order of the deepest ice features, complicating AUV measurements. Fortunately, the AUV has an upward-looking altimeter that is useful for mapping

ice draft prior to shallow transects. In this study, AUV measurements were collected at depths less than 25 m, more often 5-10 m, and for horizontal domains approaching 1 km. Once again, fixed sensors were utilized to provide lead-edge flow statistics concurrent with cross-lead transects. The spatial variability of ice cover was measured with the AUV so that it could be related to the variability of the ocean beneath. Numerous Conductivity-Temperature-Depth (CTD) profiles near the lead and in the floe interior characterized the vertical ocean structure throughout the summer. A Remotely-Operated Vehicle (ROV) collected near-surface CTD data. Auxiliary measurements like downwelling radiation, ice velocity, wind velocity, melt rates, and aerial surveys place the lead measurements in context.

2.2 METHODS

2.2.1 AUTONOMOUS MICROCONDUCTIVITY TEMPERATURE VEHICLE

The Autonomous Microconductivity Temperature Vehicle (AMTV) was developed to make horizontal profiles of turbulent properties under sea ice. The AMTV carries out pre-programmed missions to measure conductivity, temperature, depth, ice draft, salinity, turbulent heat and salt flux, magnetic heading, and pitch and roll angles and rates. It is based on the REMotely-operated Underwater measurement System (REMUS) vehicle developed at the Woods Hole Oceanographic Institution. The AMTV is 1.6 m in length, 19 cm in diameter, and displaces 33 kg. A photograph is in Appendix B. Pairs of elevator planes and rudder planes at the tail control its motion. The AMTV carries a precision Paroscientific pressure sensor and a Systron Donner Motion Pack package of accelerometers and sensitive pitch, roll, and yaw rate sensors. It employs fast-response Sea-Bird Electronics, SBE 7-02 microconductivity and SBE 7-01 microtemperature probes, as well as an upward-looking Tritech precision acoustic altimeter to measure ice draft. It operates at speeds from 1.0 to 1.6 m s^{-1} under program control. A three-dimensional course is programmed into the AMTV. This may be a combination of dead-reckoning, acoustic navigation,

and homing to one of two Benthos acoustic transponders. The AMTV has the capability to home in on acoustic beacons, either to reach a desired checkpoint during a run, or to be recovered in a submerged panel of netting. The two-dimensional position relative to a user-defined origin of the AMTV is displayed and recorded by a 100-m baseline portable acoustic tracking range developed at the Applied Physics Laboratory. In this experiment, the origin was the hut location.

The AMTV has been developed to take advantage of a Kalman smoothing scheme that uses vehicle motion to calculate vertical water velocity. The Kalman smoother makes an estimate of system state (here, vehicle state) that is an optimum combination of a dynamic model-based extrapolation and noisy measurements of a few components of the state [*Gelb*, 1974]. The smoother is founded on a linear state space representation of the dynamic system being studied. That is, the system evolution is determined by multiple first-order differential equations for the rate of change of a vector of state variables. In our case, the position and velocity of the AMTV at one time, along with the equations of motion allow us to predict its position and velocity at any later time. The motion of the vehicle is predicted from the sum of the forces acting on it, including buoyancy, the action of water flowing by it vertically, and forces exerted by the control surfaces. Because forces on the vehicle and measurements have random parts, the system model must include a random forcing function for vertical water velocity and an estimate of sensor noise to completely specify the system. The smoother uses the vehicle model and noisy observations to produce an optimal estimate of the true, unobservable state of the system. In other words, the smoother will estimate the portions of the system variability due to unforced motion of the body and due to noise. The vehicle forcing (vertical water velocity) is calculated to account for what remains. For a complete description of the AMTV and the method for estimating vertical water velocity see Appendix B. It

is also shown in Appendix B how the vertical water velocity spectra from the AMTV and TIC agree over all observed wavelengths.

Covariances of vertical velocity with temperature and salinity are calculated to estimate vertical heat and salt fluxes along the vehicle path. A "realization" of turbulence quantities is formed by detrending a 100-m segment of data (w', T', and S') and calculating the covariance estimates of heat flux, and salt flux:

$$HF = \rho C_p < w'T' > \tag{2.1}$$

$$SF = \rho < w'S' > /1000 \approx < w'S' > \tag{2.2}$$

The brackets indicate averaging. The 100 m interval is suitable for a realization because in that distance the vehicle samples a sufficient number of turbulent eddies to produce meaningful flow statistics, yet the distance is not so long that the mean conditions change. To determine if the correlation between velocity and temperature or salinity is significant, we calculate the correlations at random lags and assume they are distributed normally. If the observed correlation falls outside of two standard deviations, it is significant [*Fleury and Lueck*, 1994; *Morison and McPhee*, 1998; *Lueck and Wolk*, 1999].

Spectra of vertical water velocity are useful because they allow the calculation of two key turbulent parameters: maximum mixing length and friction velocity. The AMTV vertical velocity spectra are calculated from 100 m segments of data and are averaged in equally spaced bins on a logarithmic wavenumber axis. A multi-taper method is used with NW=12 [*Percival and Walden*, 1993]. For each segment, the log of the smoothed weighted spectrum [log ($kS_{ww}(k)$] is fit with a 10^{th} order polynomial as a function of the log of wavenumber (log k).

The maximum mixing length is the vertical scale over which the energy-containing turbulent eddies transport momentum, heat and salt. The location of

the peak in the spectrum of vertical water velocity (in cycles per meter) is taken from the 10^{th} order polynomial fit and used to calculate the maximum mixing length [*McPhee* 1994].

$$\lambda = \frac{0.85}{2\pi k_{\max}} \tag{2.3}$$

The relationship is based on observations that suggest the mixing length does not scale with distance from the boundary in the outer boundary layer (outside the logarithmic surface layer in the top few meters), but rather with the length scale associated with the peak in the wavenumber spectrum of vertical velocity [*McPhee and Smith*, 1976].

The friction velocity is a key turbulence parameter representing momentum flux

$$u_* \equiv \sqrt{\tau} = \sqrt[4]{< u'w' >^2 + < v'w' >^2} \quad , \tag{2.4}$$

where τ is the local kinematic stress. Friction velocity is the scale representing the overturning speed of the energy-containing eddies. Friction velocity can be multiplied by maximum mixing length to produce reasonable estimates of eddy viscosity in the entire boundary layer [*McPhee and Smith*, 1976]. The AMTV cannot directly measure friction velocity since the horizontal components of velocity are not available. However, an indirect method can be applied as follows.

The spectra of vertical water velocities collected by the AMTV can be used in a novel calculation of friction velocity using a technique developed by *McPhee* [2003], which is recapitulated in some detail in Appendix A. If the spectrum contains a wavenumber range where the turbulent kinetic energy depends only on production of energy and wavenumber of disturbance (an inertial

subrange), then it can be shown that there exists a universal, non-dimensional spectrum in this range. The friction velocity is calculated as the value that nondimensionalizes the observed spectrum to the universal spectrum. This technique is similar to the inertial dissipation method [*Edson et al.*, 1991] in that it uses spectral densities of turbulent vertical velocity to calculate momentum flux (stress). However it does not require the simplified turbulent kinetic energy equation of production equals dissipation, nor does it require specification of the Kolmogorov constant. Rather, simple dimensional analysis in the inertial subrange is used. The calculation is described in Appendix A.

2.2.2 SETTING AND AUXILIARY MEASUREMENTS

The present study relies heavily on data gathered during a SHEBA intensive summer observation period from July 10 to August 10, 1998. The ship track and ocean bathymetry for the SHEBA drift period are shown in Fig. 2.2. June, July, and August are the blue, pink, and black segments near the end of the drift. At the beginning of the summer, the ship drifted from the Beaufort Sea onto the Chukchi Cap, where it drifted slowly until late July, when a rapid drift off the Cap began.

During the intensive summer observation period a suite of measurements was taken near "Sarah's Lake", a lead that opened in late-May in an area of first year ice previously used as the airstrip. The base of operations was a hut located about 1 km off the port bow of the *Des Groseilliers*, near the lead edge. Outlines of the lead at different times are shown in Fig. 2.3. The perimeter of the lead was traversed with a small boat towing an acoustic beacon that was being tracked. The lead remained approximately the same size and shape for most of July, and it closed in the first few days of August. It opened to a much larger size by Aug. 4 (day 217), and even larger size by day 219 (not shown).

The basic oceanographic measurements took place at "ocean city" which was in nearly continuous operation throughout the SHEBA year. A continuously-

operating CTD (SBE 911+) collected profiles to 150 m several times per day with the exception of a few instrumental problems in July.

Data on ice-ocean exchange of momentum, heat, and salt were collected at ocean city, and they provide a valuable comparison with the lead measurements. From mid-July to mid-August, the ocean city TIC was operating between days 211 and 215 and for days 219-221. Low ice speeds and biofouling led to the data dropouts. Turbulent Instrument Clusters (TICs) consist of a rigid stainless steel mast holding two instrument clusters at set depths (both less than 10 m in our case). Each cluster consists of a set of orthogonal partially ducted current meters, a standard SBE-04 conductivity cell or SBE 07-2 microconductivity probe, a SBE 07-1 microtemperature probe, and a pressure sensor to collect mean quantities of velocity, temperature, salinity, and depth. The microtemperature and microconductivity probes have a fast response, sampling at 6 Hz and averaging over a 1- to 4-second period prior to recording to computer disk. The instruments allow the calculation of turbulent quantities of variance and covariance in the velocity components, temperature and salinity. In particular, we are interested in the vertical fluxes of momentum, heat, and salt, which are calculated using Eqs. 2.1, 2.2, and 2.4. An averaging interval of 15 minutes is used in forming the covariances, analogous to the 100 m AMTV segments. The speed of the ice relative to the ocean at the cluster depths must be greater than about 5 cm s^{-1} to overcome the rotor threshold. *McPhee* [1989] gives a more complete description of the TIC, and *McPhee* [1992] establishes the TIC as a reliable system for measuring turbulent quantities in the under-ice boundary layer.

At the lead site, a TIC using SBE-03 temperature probes and SBE-04 conductivity probes collected data near the lead edge. A cluster was typically located at the same depth as the AMTV operating depth. Flow statistics from the TIC could be compared to upstream AMTV segments. The relative ice-ocean velocity at the cluster depths did not generally exceed the threshold until day 205, corresponding to a small peak in wind velocity, then again on 208 when the wind

began to increase. The TIC was damaged by a ridging event on day 208. On days 205 and 208 there was a cluster at 3.5 m and 5.5 m from the surface. The lead TIC was resurrected on days 219-220, with a cluster at about 5.5 m. In the latter period the water traversed most of the lead before reaching the TIC.

Also at the lead site, we operated a SBE-19 CTD in mooring and profiling modes to help describe the local temporal and spatial variability during the summer observation period. The vertical profiles were useful in field calibrations of the AMTV temperature and conductivity probes, as well as numerical model initialization. They provided profiles more representative of conditions in the lead than the ocean city profiles, which were collected almost one kilometer away. The CTD was suspended from the ice at AMTV operating depths to serve as a check on the advective variability.

Yet another SBE-19 CTD was attached to a small Remotely Operated Vehicle (ROV) to sample the upper few meters of the ocean under various surface types. The ROV had a video link to the hut, along with a real-time display of the CTD data. Visual ice properties, ice draft and surrounding water properties were observed. These data were saved to videotape and computer disk. We obtained many short vertical profiles with the ROV under the ice and lead by driving it to 10-12 m, then allowing it to float to the surface. The ROV was operated from the same hut as the AMTV. The ROV was also used to aid in or observe the recovery of the AMTV after each mission.

Auxiliary measurements included ice velocity, wind velocity, downwelling solar radiation, area coverage by surface type (ice, melt pond, lead), lead albedo, ice and melt pond transmittances, surface, lateral, and basal melt rates, ice permeability, large-scale ice deformation, and a host of others related to atmospheric processes.

Ice velocities are based on Global Positioning System (GPS) measurements made at the ocean city site. In the calculations and plots here, inertial motion has been removed with a complex demodulation algorithm

[*McPhee*, 1986a, *Morison et al.*, 1987, *McPhee et al.*, 1987]. It has been shown that the interfacial stress due to inertial oscillations is generally not significant, i.e., the ice and mixed layer tend to oscillate together [*McPhee*, 1986b]. Mean velocity is calculated at a time interval of three hours.

Ten-meter wind velocity and downwelling broadband "shortwave" radiation were measured by the SHEBA Project Office meteorological tower and averaged over one hour. The shortwave detector was an Eppley PSP with a range of 285-2800 nm. The amount of surface area covered by ice, leads, and melt ponds was measured from photographs collected on helicopter surveys throughout the summer [*Perovich et al.*, 2002b]. The surveys were roughly every week from May to October of 1998, and the flight path was a 50 km by 50 km box centered on the ship. Full coverage flights on a 10 km by 10 km box centered on the ship were conducted on 17 May and 25 July. A few radiation measurements were made under ice for the purpose of spectral transmittance calculations [*Light et al.*, 2003]. The albedo of the lead at the SHEBA site was measured [*Pegau and Paulson*, 2001]. The changes in thickness and extent of the ice pack due to surface, basal, and lateral melting were observed at several sites and are summarized by *Perovich et al.* [2003]. Many types of ice (ridges, ponds, first-year, multi-year, etc.) were instrumented with ablation stakes and thickness gauges and thermistor strings.

2.3 OBSERVATIONAL RESULTS

The early and middle summer periods at SHEBA (mid-June to late-July 1998) were characterized by low wind and ice velocity, strong downward radiative fluxes, and intense surface melt that collected in leads and ponds. The snow depth averaged only 3 cm by the end of June. In late July and early August, high wind and ice velocities rapidly mixed the fresh surface waters downward and rearranged the ice cover. Surface melt tapered off, and basal melt increased along with lead fraction. By late August, the leads began to freeze.

2.3.1 GENERAL RESULTS

Wind stress and melting control the behavior of the ice pack over the summer season. The atmosphere-ocean interface in summer leads is characterized by strong solar radiation, less stress than the ice-ocean interface, and pooling of fresh water due to lateral flow of meltwater. Here we examine the observed exchanges of thermal energy, fresh water, and momentum across the various types of upper boundaries of the ocean. We begin with the bulk exchange of properties.

The surface friction velocity, u_{*0}, is a defining characteristic of the planetary boundary layer and is shown for SHEBA in Fig. 2.4a. The surface friction velocity is defined in terms of the surface stress,

$$\tau_0 = \rho u_{*0}^2, \tag{2.5}$$

where ρ is the water density. For Fig. 2.4a, the surface stress is estimated from the 10-m wind speed, U_{10}, and ice speed U_i, according to Eq. 2.6 [*McPhee*, 1990]. (Bold indicates a vector quantity.) This assumes that internal stress gradients in the ice are negligible, a good assumption during summer in the Arctic when the percentage of open water is increased. Steady state ice motion is assumed; an assumption that may be poor when the wind changes quickly over an inertial period. Horizontal homogeneity is also assumed (open water is not accounted for).

$$\boldsymbol{\tau}_0 = \rho_a C_{Da} \mathbf{U}_{10} U_{10} - if\rho_i h_i \mathbf{U}_i \tag{2.6}$$

The density of air, ρ_a, is 1.3 kg m^{-3}; the drag coefficient, C_{Da}, is 1.5x10^{-3}. The drag coefficient was shown to vary from 1.1 to 2.0x10^{-3} during SHEBA [*Andreas et al.*, 2001]. This range results in upper and lower bounds on friction velocities during the storm events of ±15% (less during quiet periods). Density (ρ_i) and

thickness (h_i) of ice are approximately 920 kg m^{-3} and 1 m. The Coriolis parameter, f, is approximately 1.4×10^{-4} s^{-1} at 80° N.

The heat available in the mixed layer to melt ice is proportional to δT, the elevation of the temperature, T, above the surface freezing temperature, T_f:

$$\delta T = T - T_f \tag{2.7}$$

The elevation of the observed 4-m temperature above freezing is shown in Fig. 2.4b, where $T_f \approx -mS$ and $m = 0.055\ ^{o}C\ psu^{-1}$.

The rate at which heat energy in the mixed layer reaches the ice, the heat flux, can be related to the temperature elevation and the surface stress through an empirical bulk relation.

$$\langle w'T' \rangle_0 = c_H \rho C_p u_{*0} \delta T \tag{2.8}$$

The exchange coefficient, c_H is approximately 0.006 over a wide range of conditions [*McPhee*, 1992]; C_p is the heat capacity of seawater at constant pressure (3980 J kg^{-1}). Figure 2.4c shows the ice-ocean heat flux (positive upward), calculated from the bulk exchange formula. Heat flux was upward at all times because the mixed layer was always above the freezing temperature. The solid line shows heat flux using a mixed layer temperature that has been interpolated to fill in missing data. The circles show heat flux when temperature elevation was actually observed.

Figure 2.4d shows the bulk estimate of salt flux at the ice-ocean interface that results from the ocean heat flux of Fig. 2.4c. Upward heat flux at the ice-ocean interface, if not compensated by conduction through the ice, causes ice melt. The rate of release of meltwater downward into the water column (upward

salt flux) due to the oceanic heat flux can be estimated using the salt balance equation [*McPhee*, 1992].

$$\langle w'S' \rangle_0 = \langle w'T' \rangle_0 (S_{ml} - S_{ice}) q_l^{-1} \tag{2.9}$$

For Fig. 2.4d, the ice salinity is taken to be 2 psu (varies from 0 to 4 psu depending on ice type and vertical position according to *Eicken et al.* [2002]), and the value of q_l is set at a representative value of 74 K. The assumption that there is no heat conduction from the ice to the atmosphere is reasonable because most of the ice is isothermal at the freezing temperature for most of the summer [*Perovich et al.*, 2003]. However, it is important to note that meltwater can also enter the ocean via runoff or percolation from surface melting, but it is not included here.

Ocean city CTD data for June, July, and August are presented in Fig. 2.5. Bathymetry during the SHEBA drift is shown with salinity contoured in depth and time (Fig. 2.5a). In Fig. 2.5b, the square of the buoyancy frequency, N^2, is contoured.

$$N^2 = -\frac{g}{\rho}\frac{\partial \rho}{\partial z}, \tag{2.10}$$

where g is the gravitational constant. The temperature is not used in the calculation of density gradient here because it affects the density very little near the freezing point. An objective, if arbitrary, definition of the mixed layer is arrived at by finding the depth at which the squared buoyancy frequency exceeds a specified value. The 1×10^{-4} s^{-2} contour is plotted in magenta and taken to be the mixed layer depth. (Choosing a value of 5×10^{-4} s^{-2} would lower the mixed layer 1 to 2 m.) Also shown in Fig. 2.5b are times and depths of AMTV runs (black circles). After day 210, most of the runs were in the mixed layer. Potential

temperature and elevation of potential temperature above surface freezing temperature are also shown (Figs. 2.5c and 2.5d).

2.3.2 SEQUENCE OF EVENTS WITH SPECIFIC AMTV EXAMPLES

The SHEBA summer experiment can be divided into two periods separated by a transitional period. The first period of mid-June to late-July was relatively calm: Fig. 2.4a shows the surface stress and wind were low until a moderate peak centered on day 208, followed by a large, sustained event from about 210-214 (the transitional period). The ice-ocean heat flux was also relatively weak before day 208 (Fig. 2.4c). The vertical structure of salinity from ocean city (Fig. 2.5a) changed little during the quiet period, with the exception of the period when the camp drifted onto the Chukchi Cap (days 159-165). In addition, the mixed layer shoaled from about 15 m to 6 m (Fig. 2.5b).

The mixed layer warmed in the pre-storm period, as shown by potential temperature (Fig. 2.5c) and elevation of potential temperature above surface freezing temperature (Fig. 2.5d). Other temperature features during the quiet period were concurrent with the drift onto Chukchi Cap.

In the pre-storm period, snow and ice melt was trapped near the surface in leads, cracks, and ponds. The small-scale vertical structure of salinity and temperature near the lead was measured with the ROV CTD and a CTD towed from a small boat [*Paulson and Pegau,* 2001]. *Paulson and Pegau* [2001] found that a warm, fresh layer of meltwater grew steadily in the SHEBA lead from mid-June to late-July and shrank rapidly during the main storm on days 210-214. The very fresh surface layer is not visible in the ocean city profiler data in Fig. 2.5 because the ice around the hole was thicker than the fresh layer. The ROV camera and CTD tracked the depth progression of the fresh-water interface in the SHEBA lead (Fig. 2.6a and 2.6b). On day 206 (July 25) the layer reached a maximum depth of 1.2 m in the lead while the ice draft surrounding the lead was slightly less. The layer had a salinity of about 2 psu and a temperature of 1.6 ^{o}C

[*Paulson and Pegau*, 2001]. The ROV was unable to sample the uppermost part of the layer because it was insufficiently buoyant in the low-density water there. Leads sampled within 30 km of SHEBA on day 203 showed similar warm, fresh layers around 1 m thick [*Richter-Menge et al.*, 2001], similar to observations from the SHEBA lead. The fresh water formed from surface melt did not appear to mix into the upper ocean during the quiet period.

The AMTV data collected during the quiet period (day 204) indicate that vertical mixing of temperature and momentum was weak. Figure 2.7 shows vehicle depth and ice draft in the first panel, temperature in the second and horizontal position in the third. The vehicle was at a depth of 10 m initially; it climbed to 6 m then back to 10 m (segments 1-3, respectively). The mean ice draft was just over 1 m, with a ridge of about 3 m draft. The temperature profile indicates a weak vertical temperature gradient: temperatures at 6 m (segment 2) were about 0.02 C^o lower than at 10 m. The outline of the lead is shown in the third panel. The star represents the starting point of the run, the circles and squares indicate the beginning and end of each run segment to be analyzed. On these "legs" the AMTV was not making maneuvers such as depth or heading changes, allowing one to obtain vertical water velocity using the Kalman smoother. The ice velocity of 6.4 cm s^{-1} (from demodulated GPS data) is shown as an arrow; the length of the arrow corresponds to the distance the ice traveled in 1000 sec (about 17 min). The thick line segments indicate open water acoustic returns. This run is typical of runs made from day 203 to day 208, as the lead geometry and direction of ice motion were fairly constant.

Figure 2.8 shows the deviation quantities of detrended temperature, vertical water velocity, heat flux, and friction speed. Unfortunately, the microconductivity sensor was damaged slightly in a recovery operation on day 195 and was not operating correctly. It was replaced on day 213. No salinity-related quantities at the lead are available from the AMTV from day 195 to 212. Temperature shows a smaller variance at 6 m (segment 2) than at 10 m (segments

1 and 3), and no effects of the lead are visible. Vertical water velocity fluctuations are fairly uniform with depth and horizontal position, with perhaps more variance at 10 m. The covariances of temperature and vertical water velocity are calculated from 100-m segments of data. A horizontal bar represents the value of each segment. Only the first two bins downstream of the lead (the 300 m to 500 m region in the distance coordinate) at 6 m depth are statistically significant at the 95% level. The fluxes there are 10 W m^{-2} upward followed by 3 W m^{-2} downward. The friction speed is shown with the surface friction speed of Fig. 2.4. The small dots represent the 95% confidence interval. Friction speed is steady at 0.5 cm s^{-1} except for one point near the end of the run. Mixing length is steady at about 1.2 m throughout the run (not shown). There were relatively low friction speeds and negligible or small heat fluxes at 6 and 10 m near the lead on day 204 (during the quiet period).

Large changes were observed in the ocean during the first major storm of the summer around days 210-214. The wind reached its highest velocity of the previous few weeks (Fig. 2.4a). The ice-ocean relative velocity increased enough around day 210 to detach long diatom strands from the ice underside. The strands had been growing under the ice near the lead and had reached lengths of up to 1 m. The release of the mucus-like strands was problematic for many instruments. (From day 206.5 to day 208.5 as the wind began to strengthen, the ocean city CTD was not functioning primarily due to biofouling.) The increase in wind speed was associated with an increase in bulk ice-ocean heat flux. The heat flux was the strongest of the summer from day 208 to day 212 (Fig. 2.4c). Although the wind event around day 208 was smaller than what followed, the mixed layer contained more thermal energy, which gave rise to a comparable flux magnitude. By the end of the storm, the mixed layer cooled to about 0.1 C^{o} above the freezing temperature (Figs. 2.4b and 2.5d) and deepened to about 16 m (Fig. 2.5b). A layer of warm water between 20 and 30 m in the pycnocline remained through the storm (Fig. 2.5c). Most dramatically, from day 209-214, the mixed layer

freshened more than 1 psu (Fig. 2.5a). As the camp drifted from Chukchi Cap into deep water during the storm, the pycnocline also freshened from 30-60 m (Fig. 2.5a).

The change in mixed layer salinity during the storm can be used to estimate the total salt flux at the ocean interface. The ocean city salinity profiles in Fig. 2.5a are used to calculate the rate of change in salt content of the top 30 m. This may include some advective changes not due to surface processes, especially during periods when the camp drifted over topographic features. The advective rate of change in integrated salt content is that estimated by assuming the whole water column salinity changed by an amount represented by the salinity change at 30 m. This is subtracted from the actual rate of change of salt content in the top 30 m to obtain the interfacial flux. We find a significant flux only from days 210 to 215: $4.6 \pm 1.5 \times 10^{-5}$ kg m^{-2} s^{-1}, corresponding to about 80 cm of fresh water mixing down over those 6 days. The 95% confidence interval is formed from the uncertainties in the linear best-fit model used to calculate the rates of change. We find a similar result with the CTD data from the lead edge. Because the salt flux includes meltwater stored in leads and percolating through the ice, it is about an order of magnitude larger than the instantaneous salt flux due to bottom melt shown in Fig. 2.4d.

The transition period is largely signified by this mixing away of the fresh layer of water in the lead. During the first wind event from 206.5-210.5, the layer receded from 120 cm to 65 cm (Fig. 2.6a and 2.6b). This is equivalent to a salt flux in the lead of $5.0 \pm 1.0 \times 10^{-5}$ kg m^{-2} s^{-1}. During the major wind event from day 210.5 to day 212.5, the remaining 65 cm of fresh water were mixed away, corresponding to a salt flux of about 12×10^{-5} kg m^{-2} s^{-1}. The 50 km x 50 km area around SHEBA began to diverge around day 209 [*Stern and Moritz*, 2002], but the SHEBA lead itself closed by day 213 before widening in the days following. The effect of divergence or convergence on the thickness of the fresh water layer is neither known nor accounted for in the salt flux calculation, however it is

possible that divergence could thin the fresh layer. In this case a vertical salt flux out of the lead is not implied.

The ROV video record clearly revealed the change under the ice as the fresh layer eroded. The diatom colonies were ripped from the ice underside, and ice crystals formed in the top few meters of the ocean as the fresh surface water interacted with the colder, saltier water on day 209. The frazil ice floated to the surface and encased what remained of the diatom colonies, before eventually melting away a day or so later.

An AMTV run from the storm period shows increased activity in the mixed layer: large momentum, heat, and salt fluxes were observed. Figure 2.9 illustrates the run setup. On day 213 (August 1), the major wind event of the summer was in full swing, with wind speeds of over 8 m s^{-1} (16 knots). The ice cover shifted around changing the geometry of the lead. Open water sections were no wider than about 50 m (Fig. 2.9a). In Fig. 2.9c, we see the AMTV initially traveled in the negative x-direction (segment 1) and returned past the origin to the positive x direction (segment 2), returning (segment 3) to make a final excursion in the negative y direction (segments 4 and 5). The ice velocity is shown: 21 cm s^{-1}. The AMTV was at a depth of 8 m, and observed a mean ice draft of about 1 m with a ridge approaching 4 m depth located at x=150 m, y=0 m (sampled in the last half of segment 2 and halfway through segment 3).

Deviatory data (now including salinity deviations) are plotted in Fig. 2.10. Absolute salinity is questionable due to a nonlinear drift in the microconductivity, and the first 500 m of conductivity data were unusable. The AMTV encountered large temperature variations as it traveled from -250 m to +250 m in the x-coordinate and returned to the origin (segments 2 and 3 in Fig. 2.10a—particularly near the ridge). Plots of salinity deviations and vertical water velocity show only slightly elevated activity in this region (Fig. 2.10b and 2.10c). Note the vertical water velocity amplitude was roughly twice that of day 204. Figure 2.11 shows significant turbulent fluxes from 500 m to 1100 m in the run

coordinate (the portions of segment 2 and 3 under and downstream of the ridge as indicated). The heat flux was 72-74 W m^{-2} upward for three 100-m segments and 31 W m^{-2} upward for one. Salt flux also had significance for four segments: one was 0.82 kg m^{-2} s^{-1} upward and three of them averaged 1.1 kg m^{-2} s^{-1} downward, an apparent paradox with the expected upward heat flux and upward salt flux under melting ice. Friction speed was high, especially for segments under and downstream of the ridge. Values were even above the surface value of about 1 cm s^{-1}. The friction speed was 2-3 times larger than on day 204. Maximum mixing length from vertical water velocity spectra was steady at 1.0 m, except for two extrema at 1.5 m and one at 0.2 m. The AMTV observed an active mixed layer on day 213 during the storm, particularly under and downstream of a ridge.

After the storm a brief quiet period around day 214-217 was followed by another wind event from 218-220 (Fig. 2.4a). Combined with a brief rise in temperature, this wind event corresponded to a smaller, briefer pulse of heat flux around day 218 (Fig. 2.4c). The mixed layer salinity and temperature were otherwise relatively steady (Figs. 2.5a and 2.5c), and the mixed layer depth was around 20 m except for a brief shoaling to 10 m (Fig. 2.5b). The layer of warm water in the upper pycnocline was maintained following the major storm and throughout the rest of the summer: the mixed layer was within 0.1 C^{o} of the freezing temperature, while the pycnocline was about 0.2 C^{o} above freezing (Fig. 2.5d). Another mid-depth temperature maximum was observed over the sloping bathymetry (Fig. 2.5c) as camp continued to drift off Chukchi Cap, presumably related to topographically steered currents along the shelf slope.

In the post-storm period, meltwater was not trapped near the surface but entered the ocean as the melting occurred. The fresh layer of meltwater did not reappear. The lead profiles of temperature and salinity generally resemble the day 219 (August 7) profile in Fig. 2.6. A detailed view (Fig. 2.6c and 2.6d) shows the lead surface had weak gradients, was stably stratified, and was above the freezing temperature.

For the post-storm period, the AMTV data indicate strong fluxes of momentum in the lead and under ice, but only strong heat and salt fluxes in the lead. The last day of AMTV observations was day 219-220 UT. The wind had increased again after a few days of relative calm, and the lead had grown dramatically in size around day 215. Figure 2.12 shows the run on day 219.9. Vehicle depth was 5 m, and ice draft averaged about 1 m with several ridges of about 3 m (Fig. 2.12a). After traveling for 800 m without leaving the lead (segment 1), the AMTV returned (segment 2) and continued to travel in the positive x-direction 200 m under the ice (segment 3) before returning to the origin (segment 4). See Fig. 2.12d. The ice velocity of 15 cm s^{-1} is shown. The temperature increased as the lead was approached from upstream (segment 2), peaked at the lead edge, then fell with distance under the ice (segment 3). See Fig. 2.12b. Nearly the same trends were observed on both the "out" and "back" legs. Salinity decreased over segment 2 then remained uniform under the ice. The overall slope of salinity (particularly segment 1) is biased due to the nonlinear drift in the conductivity. Figure 2.13 shows both temperature and salinity had much higher variances in the lead compared to under the ice. Also, temperature and salinity deviations were about four times bigger than on day 213, while vertical water velocity was slightly less energetic than day 213. Figure 2.14a and 2.14b show strong downward heat fluxes and upward salt fluxes under the lead and smaller fluxes under the ice. The lead fluxes of heat and salt averaged 98 and 144 W m^{-2} and 1.7 and 2.4×10^{-5} kg m^{-2} s^{-1} (segments one and two). Segment three did not pass the significance test for heat or salt flux, and segment four only had significant salt flux: 1.9×10^{-5} kg m^{-2} s^{-1}. The segment averages reported here are calculated from the covariances over each entire segment, not the average of the 100 m segments. The first 200 m of segment one were not included due to salinity drift contamination (see Fig. 2.13). Friction speed was close to the surface value and between the friction speeds of days 204 and 213 (Fig. 2.14c). Maximum mixing length averaged around 0.7 m with a

maximum of 1.8 m at the lead edge. AMTV data from after the major storm of the SHEBA summer show exchange at the ocean surface, especially in leads.

2.3.3 BULK, TIC, AND AMTV OBSERVATIONS

The bulk estimates of fluxes of Figure 2.4 are compared to the values just below the ice measured directly by the ocean city TIC in Fig. 2.15. The TIC measurement depths were 3.5-4 m (cluster 1) and 7.5-8 m (cluster 2), and the ice draft at ocean city averaged 1.4 m from day 210 to 220. Figure 2.15 shows the friction speed, heat flux, and salt flux from clusters 1 and 2 for the period along with the bulk estimates. Each data point represents an average of several 15-minute "realizations" of turbulent quantities (from 4 to 12 realizations per data point). The salt flux estimates from the deeper cluster were corrected for the temporal lag of the standard SBE-04 conductivity sensor [*McPhee and Stanton*, 1996] with output of a microconductivity cell.

Fluxes below the ice can be compared directly to the surface estimates and to a similarity prediction based on the surface values. The solid points in Fig. 2.15 are predicted for the TIC depths from the analytical similarity solution for the horizontally homogeneous, steady boundary layer forced by surface stress and buoyancy flux [*McPhee*, 1983]. The surface stress is determined from force balance, and the buoyancy flux (proportional to salt flux) only includes melt estimated from ice-ocean heat flux—no runoff. The theory predicts an exponential fall off with non-dimensional depth, ζ, of momentum and scalar fluxes.

$$u_{*sim}^2 = H(\zeta)u_{*0}^2 \tag{2.11}$$

$$\langle w'T' \rangle_{sim} = H(\zeta)\langle w'T' \rangle_0 \tag{2.12}$$

$$\langle w'S' \rangle_{sim} = H(\zeta)\langle w'S' \rangle_0 \tag{2.13}$$

$$\text{where } H(\zeta) = e^{b\zeta},\ b = (2\kappa\zeta_N)^{-\frac{1}{2}},\ \zeta = z(\frac{u_*\eta_*}{f})^{-1},\ \eta_*^{-2} = 1 + \frac{\Lambda_*\langle w'b'\rangle_0}{fR_c u_{*0}^2} \qquad (2.14)$$

$$\langle w'b'\rangle_0 = g\alpha_S\langle w'S'\rangle_0 - g\alpha_T\langle w'T'\rangle_0 \qquad (2.15)$$

The last equation is the buoyancy flux, and α_S and α_T are expansion coefficients for salinity and temperature. Constants are κ=0.4 (the von Karman constant), ξ_N=0.05, Λ_*=0.028, and R_c=0.2 (the critical flux Richardson number). See below for more discussion on length scales in turbulent boundary layers. The surface buoyancy flux enters the calculation through the stability parameter, η_*.

The friction speed and fluxes observed by the TIC are significantly lower than the surface values and those predicted by similarity theory for days 211-215. On days 219-220 the TIC friction speeds are close to the surface value and even higher at times (Fig. 2.15a). The lower and upper clusters measured similar stresses on all days. TIC heat fluxes are smaller than expected for days 219-220, and the lower cluster measured weaker fluxes (Fig. 2.15b). Contrary to the earlier period, salt fluxes on day 219-220 are much higher than estimated at the surface from the heat balance (Fig. 2.15c). Recall that the salt flux at the upper ocean boundary based on mixed layer salinity changes from day 210 to day 215 is about 10 times larger than the heat balance estimate shown in the solid blue line of Fig. 2.15c. Using the larger flux gives more strongly attenuated similarity predictions for stress and heat flux, which is addressed in numerical simulations to follow.

The AMTV run averages compare favorably to the surface values of Fig. 2.4 and lead-edge TIC values. The friction speed comparison is shown in Fig. 2.16. The blue line indicates values calculated from wind and ice velocities as in Fig. 2.4. While the AMTV-derived friction speeds vary greatly over any given run, the run averages of Fig. 2.16 agree reasonably well with the surface estimate. The average is computed from the 100-m segment values like those of Fig. 2.14. Pink crosses show the averages for each run. On many days, especially before day 209, the AMTV sampled multiple depths in the same run. Segments within a

run that were above a non-dimensional depth of 0.4 (see Eq. 2.14) based on bulk surface estimates (no percolation) were averaged to form the red squares. With only two exceptions this amounts to averaging segments that were above 10 m (see Fig. 2.5b for run depths). These points are considered to be in the boundary layer. Agreement with the surface friction speed is good, except for more extreme values of the peaks and valley on days 211-213. Lead-edge TIC data is shown with the blue stars (3.5 m depth) and green stars (5.5 m depth). Except for day 205, the TIC shows friction speeds at or above the surface value. On days 219-220, the lead edge TIC (only one at 5.5 m) mostly agrees with the AMTV. This can be contrasted to the ocean city TIC (Fig. 2.15) where the observed friction speed was typically less than the surface estimate except on day 219-220. On day 219-220 both TIC systems and the AMTV were operating, and there is considerable overlap.

Figure 2.17 is a similar AMTV plot for heat flux. The heat flux calculated from the bulk exchange formula is the solid blue line (as in Fig. 2.15). AMTV run averages for all depths and for depths in the boundary layer are shown by the pink crosses and red squares, as in Fig. 2.16. Only those 100 m segments that show a significant correlation between vertical water velocity and temperature are used in the averages. The AMTV averages are mostly upward but not as strong as the bulk estimate. One exception is day 213, where heat flux is much larger upward. Other exceptions are the data after days 215 when the AMTV heat flux is strong and downward. The ice fraction increased dramatically after day 215, so most of these segments are not under ice. The TIC heat flux from the downstream edge of the lead is always downward at both 3.5 m and 5.5 m depths. The ocean city TIC heat flux (Fig. 2.15b) is not comparable to the lead-edge TIC, but does show a suggestion of the high upward heat flux on day 213, followed by lower values on day 215, like the AMTV. However, at no time does the ocean city TIC indicate downward heat flux.

We suspect the strong downward heat flux at the lead after day 215 is due to radiative heating. Figure 2.18 shows the detail on days 219-220, when the downward heat flux at 5 m in the lead was especially strong. The additional solid blue line is the downward shortwave radiative flux as measured by the SHEBA Project Office. The lead TIC and AMTV are in fair agreement, and the TIC heat flux at 5.5 m is consistent with the shortwave flux, at 30-50% of the amplitude.

The AMTV average salt flux comparison is illustrated in Fig. 2.19. As mentioned above, the AMTV conductivity probe was not functional until day 213. Until day 219, very few AMTV runs showed significant correlation between vertical water velocity and salinity. The lead TIC showed upward salt fluxes on days 205 and 208, and those were especially large on day 208 when the first wind event was peaking. The AMTV salt flux on day 213 was downward, as described (Fig. 2.11). A strong upward salt flux was observed on day 215, and then small values prevailed until 219. For days 219-220, the AMTV and lead TIC both showed strong upward salt flux well above the surface heat balance estimate, as did the ocean city TIC on day 219 (Fig. 2.15c).

2.4 DISCUSSION

2.4.1 PERIOD I: SURFACE TRAPS MELTWATER

For much of the melt season, ice and snow meltwater was trapped near the surface. From day 152-190 (June to early-July), the mixed layer temperature and salinity were relatively steady (Fig. 2.5a and 2.5c), yet the surface was rapidly melting [*Perovich et al.*, 2003]. Since the ice was still not permeable, surface melt drained laterally into low-lying areas of melt ponds and leads [*Eicken et al.*, 2002]. Mid-July (days 190-207) saw that the mixed layer warmed in the top 30 m and shoaled but still did not freshen significantly. Higher ice permeability allowed more vertical percolation of melt in mid-July, but fresh water continued to build up in leads and cracks [*Eicken et al.*, 2002; *Paulson and Pegau*, 2001]. The buoyant melt probably tended to find the sea level (the lead surface) even

when it percolated through the ice underside. This means lateral flow of meltwater was still significant when vertical percolation was occurring.

There are two reasons why surface melt did not mix into the upper ocean during the quiet period. First of all, fresh water that entered the ocean often formed an underwater ice layer or false bottom when it came into contact with the colder seawater: false bottoms tended to trap the runoff near the surface [*Eicken et al.*, 2002]. Underwater ice forms when fresh water and seawater at or near their respective salinity-determined freezing temperatures contact each other under quiescent conditions [*Untersteiner*, 1961; *Martin and Kauffman*, 1974]. Because solar heating was larger in leads, the meltwater that was collected there and the seawater beneath it were above their respective freezing temperatures, and underwater ice could not form. The second reason fresh water did not mix vertically was because of the strong and stable density gradient near the lead surface and low ice speeds (typically 5 to 7 cm s^{-1} in mid-July). As described above and in *Paulson and Pegau* [2001], meltwater intermittently formed a fresh surface layer in the SHEBA lead from day 170 to day 184 and grew steadily to 1.2 m by day 207.

It is possible to quantify the tendency for a buoyant layer in a lead to form with an Obukhov length, L_0.

$$L_0 = \frac{u_{*0}^3}{\kappa \langle w'b' \rangle_0} \tag{2.16}$$

The Obukhov length is the distance from a boundary at which the buoyancy production or destruction of turbulent kinetic energy is balanced by shear production. At depths less than $|L_0|$, turbulence is generated by shear, and buoyancy effects are small, which is known as forced convection. In wintertime unstable or free convection, dense brine rejected during ice formation drives cellular convection and generates turbulence for depths greater than $|L_0|$. In the

summer, stabilizing meltwater tends to balance shear production. During periods of freshwater flux, mixing (shear-driven) is confined to depths shallower than $|L_0|$. During times of relatively high wind stress, the mixed layer may be shallower than $|L_0|$, and the mixed layer would tend to deepen.

An estimate of the Obukhov length beneath the lead can be made for days 190-207. The surface friction speed rarely exceeded 0.005 m s^{-1} and averaged 0.0035 m s^{-1} (Fig. 2.4a). An upper bound on the freshwater flux in the lead is found from the mean rate of surface ablation from day 190-207: 1.5 cm day^{-1} [*Perovich et al.*, 2003]. Assuming all of the melt from ice drained into leads (about 75% and 5% of area, respectively, from *Perovich et al.* [2002b]) gives an equivalent melt rate of about 23 cm day^{-1}. This rate of ice melt corresponds to a freshwater runoff flux into the lead by Eq. 2.17 of about $7\text{x}10^{-5}$ kg m^{-2} s^{-1} or $5.3\text{x}10^{-7}$ W kg^{-1} for buoyancy flux by Eq. 2.15.

$$\langle w'S' \rangle_0 = w_{perc}(S_{ml} - S_{ice}) = \frac{\rho_i}{\rho}\frac{dh_i}{dt}(S_{ml} - S_{ice}) \tag{2.17}$$

The above values result in Obukhov lengths of 0.59 m for the maximum friction velocity or 0.20 m for the average friction velocity. Assuming the fresh water uniformly enters the ocean (by using the spatial average of surface melt rate of 1.5 cm day^{-1}) the salt flux is reduced to a lower bound of $4.6\text{x}10^{-6}$ kg m^{-2} s^{-1}. In this case, Obukhov length was 8.9 m or 3.1 m for maximum or mean surface stress.

The Obukhov length estimates indicate that when the meltwater drained laterally into leads (upper bound) in the early summer, turbulent stress was too weak to mix it vertically: Obukhov lengths were less than the ice draft. Even using the average surface stress over days 190-207 and horizontally averaged fresh water flux (the lower bound) results in an Obukhov length (3 m) on the order of ridge keel depths. Only during periods of above-average surface stress and away from leads did the Obukhov length exceed the nearby ridge keel drafts.

The ratio of the neutral-stratification eddy size ($0.05u_{*0}/f$) to the Obukhov length is the "turbulent lead number" of *Morison et al.* [1992]. The turbulent lead number was developed for use in unstable convection from wintertime leads, but its basis in the turbulent kinetic energy equation does not require a particular sign for buoyancy flux. For freshwater fluxes in the lead near the upper bound ($7\text{x}10^{-5}$ kg m^{-2} s^{-1}), this lead number is less than one, implying that buoyant destruction of turbulence dominated the entire boundary layer in the lead. In other words, turbulent eddies generated by ice motion were inhibited by the stabilizing effect of meltwater at the lead surface. AMTV observations from day 204 (Fig. 2.8) support the low turbulence levels below 4 m in the lead: at 6 m the vertical water velocity and temperature fluctuations were small and heat flux at 6 m was very small or zero, despite the solar heating of the lead surface. Friction velocities were among the smallest observed with the AMTV in the mixed layer.

The persistence of the fresh layer in the lead can also be examined in terms of the internal Froude number:

$$Fr = \frac{U}{\sqrt{g' H_l}} \quad \text{where } H_l \text{ is the layer thickness and } g' = \frac{g(\rho - \rho_l)}{\rho} \tag{2.18}$$

We assume the layer moves with the ice and is contained by the ice draft. (The draft exceeds the layer depth.) When the velocity of the fluid below the layer (approximately the ice velocity) exceeds the wave speed at the interface, the ice can no longer block the flow of fresh water downstream. Under this supercritical condition, the layer begins to slide under the ice, is forced past a rough surface, and is entrained into the mixed layer. Prior to day 207, ice speeds were less than 10 cm s^{-1} and the layer salinity was less than 5 psu, compared to 31 psu for the seawater. For the Froude number to be greater than one and allow the layer to escape, the layer would have to be less than 0.06 m. The lead layer probably reached this depth or greater during a few hours of low ice velocity and survived

the next significant ice movement. In terms of Froude number criticality, as the layer grew it became more resilient to ice motion. By day 185, the interface was at a depth of 20-30 cm [*Paulson and Pegau*, 2001]. On day 208, the ice velocity finally exceeded 10 cm s^{-1}. By this time, the layer was 1.2 m thick. In this case Fr= 0.3 (ice speed of 0.12 m s^{-1}, layer thickness 1 m, and salinity jump of 26 psu). The Froude number suggests the fresh water in the lead was still stable, and indeed the layer remained in the lead as the ice began to move (until day 212.5 according to the ROV data).

However, the layer was shrinking at a rate of about 13 cm day^{-1} from day 206.5 to day 210.5 (based on ROV observations). The lead-edge TIC observed large heat and salt fluxes consistent with warm, fresh water mixing downwards on day 208 (Figs. 2.17 and 2.19). Apparently other mechanisms were acting to thin the fresh layer while the ice velocity remained sub-critical. It is likely that as the ice began to move on day 206.5, the layer was eroded away by turbulence generated upstream of the lead more quickly than the melt was supplied. After day 210 ice divergence also thinned the layer: ice divergence in a 50 km by 50 km box containing SHEBA became positive on day 210 (2.5% per day) and remained positive for the next several days [*Stern and Moritz*, 2002]. On day 211, the thickness was 36 cm, and the ice speed was up to at least 0.20 m s^{-1}, so that Fr=0.8. By the end of the day the layer was at 12 cm, and it was gone the next day. The order-one Froude number on day 211 suggests the layer finally became thin enough to be unstable and was rapidly flushed out of the lead. From day 206.5 to day 212.5, the fresh lead layer was destroyed by a combination of erosion from below, ice divergence, and hydrodynamic instability.

2.4.2 PERIOD II: MELTWATER ENTERS OCEAN

The transition stage at SHEBA (210-214) finally saw the mixed layer freshen dramatically (Fig 2.5a). The observed mixed layer change implies a surface salt flux over that period of 4.6×10^{-5} kg m^{-2} s^{-1}. To calculate the salt flux

from mixed layer salinity, one must assume that the change in salinity at 30 m is unaffected by the surface and that in the absence of surface processes the salinity profile above 30 m would hold its initial shape throughout the period. The latter assumption is questionable in such a variable region as the Chukchi Cap, i.e. there could be advective effects above 30 m that are not identical to those at 30 m. On the other hand, the total amount of freshening observed at SHEBA (minus the 30 m advective change) roughly corresponds to the total ice and snowmelt: 112 cm of fresh water similar to the observed 126 cm. *Perovich et al.* [2003] report the latter value for days 147-244. In addition, buoys about 20 km from SHEBA showed simultaneous mixed layer freshening of the same magnitude as the advection-corrected SHEBA CTD [*McPhee*, personal communication]. The freshening occurred 2-3 days before the SHEBA camp left shallow water, which also suggests that much of the mixed layer freshening was not linked to the drift into deeper water.

The flux implied by mixed layer freshening is much larger than the heat balance estimate (Fig. 2.4) and the lead flushing flux. From section 2.3.2, the lead salt fluxes were 5×10^{-5} kg $m^{-2} s^{-1}$ for day 206.5 to day 210.5 and 12×10^{-5} kg m^{-2} s^{-1} for day 210.5 to day 212.5. Since the lead fraction was about 5%, the mixed layer would experience fluxes about 5/95 or 5% of these magnitudes, not nearly enough to account for the observed salinity changes. The heat balance estimate of salt flux is also too small and shows little correspondence to changes in the mixed layer. Clearly surface retention and subsequent runoff were a major factor [*Eicken et al.*, 2002]. Using 4.6×10^{-5} kg m^{-2} s^{-1} and the maximum friction speed of 0.015 m s^{-1} results in an Obukhov length for the storm period of 24 m. Using an average friction speed of 0.01 m s^{-1} results in a value of 7.1 m. As expected, the high levels of shear-generated turbulence during the storm reached the mixed layer and deepened it despite the very large stabilizing buoyancy flux (Fig. 2.5b).

During the high winds on day 213 the AMTV showed particularly strong friction speed at 8 m (Fig. 2.11): the run average of 0.012 m s^{-1} was larger than

the surface value (Fig. 2.16). Heat flux was also much higher than the bulk estimate, averaging 60 W m^{-2} upward over the run (Fig. 2.17). The most interesting result is the strong *downward* salt flux, averaging $-1x10^{-5}$ kg m^{-2} s^{-1} (Fig. 2.19), despite a flux of $+4.6x10^{-5}$ kg m^{-2} s^{-1} estimated from ocean freshening during days 210-215. Most of the activity took place under and downstream of a ridge (Fig. 2.11). A second run also at 8 m a few hours later showed even stronger upward heat flux and downward salt flux under regions of ridges and small leads (run averages of 0.015 m s^{-1}, 100 W m^{-2} and $-2x10^{-5}$ kg m^{-2} s^{-1}). Because these two runs took place when the lead fresh layer had just disappeared (212.6 and 212.8), it is possible that the fresh warm plume from the lead was forced under adjacent ridges and under saltier, cooler water from the downstream side of the ridge. In general, this is a mechanism that may arise when a strong downward fresh water flux is upstream of a weak or small fresh water flux. If the less dense fresh water from the lead is forced downward as it is swept under the adjacent ice, it is possible that it undercuts denser, saltier water. This unstable situation could only occur if the horizontal density gradient has the same sign as the horizontal fluid flow relative to the ice, e.g. at the downstream edge of a summer lead. Such "over-running overturns" would enhance the turbulent mixing at the downstream lead edges causing an increase in the variance of vertical water velocity (implying a higher ice-ocean stress and possibly a deeper mixed layer) and an increase in its characteristic length scale. See *Crawford et al.* [1999] for a discussion of observations suggesting the presence of this mechanism in the mixed layer under land-fast ice. The over-running overturns may explain the downward salt flux and strong heat and momentum fluxes observed by the AMTV in this region.

2.4.3 PERIOD III: QUASI-STEADY BOUNDARY LAYER

The period after day 215 was characterized by weak freshwater fluxes and stronger winds. A brief period of low wind stress (around day 215) may have

allowed the surface melt to build up slightly in a layer in the lead, but not to a thickness to which it could be maintained through the next wind event. On day 215, the friction velocity and salt flux at the surface were 0.005 m s^{-1} (Fig. 2.16) and $4x10^{-5}$ kg m^{-2} s^{-1} (Fig. 2.19), respectively. The surface salt flux should be roughly a factor of two larger than the AMTV flux at 5 m in this range, according to similarity theory (Eqs. 2.13-2.15). The resulting Obukhov length for day 215 is about 1 m. By day 220, the friction velocity had increased to nearly 0.01 m s^{-1}, and the salt flux at the surface was about $2x10^{-5}$ kg m^{-2} s^{-1}. The Obukhov length increased to 16 m. No fresh layer was observed.

Despite highly permeable ice, the meltwater found the lead surface before mixing downward, presumably due to surface and internal drainage. Indeed, on day 220 the AMTV still observed the salt flux to be in the lead, not under the ice (Fig. 2.14). The heat flux at 5 m in the lead was downward. The lead surface was being warmed and freshened, and these properties were mixed downward by turbulence advected from upstream and generated by wind at the lead surface. The cumulative effect of the vertical convergence of fluxes on a particular water parcel in the lead was to warm and freshen it as it neared the lead edge (Fig. 2.12). At downstream distances greater than about 100 m under the ice, fluxes were smaller or did not pass the significance test, and the friction speed at 5 m increased. The variances of temperature and salinity were also reduced in the region (end of segment 3 and beginning of 4). The data seem to describe a steady internal boundary layer whose structure was determined from the time dependent surface boundary conditions of heat and salt fluxes, and stress.

One can make a simple estimate of the depth, h, of the internal boundary layer (IBL) as a function of distance downstream, x, from the change in roughness length. It is based on the change in roughness length from the lead "surface" to the ice surface [*Garratt*, 1990; *Kantha and Clayson*, 2000].

$$\frac{h}{z_0}\ln(\frac{h}{z_0})-\frac{h}{z_0}+1=2\kappa^2\frac{x}{z_0} \tag{2.19}$$

Simply put, one assumes that the "signal" of the new boundary roughness "diffuses" via turbulence away from the boundary with distance downstream, much like a spot of dye injected at the wall of a boundary layer flow would diffuse. In our case the signal is momentum. The bulk of the IBL work has been applied to the neutral atmospheric boundary layer, in which case one can safely assume as in the references cited above that the IBL is within a surface layer. In the ice-ocean boundary layer, the surface layer is much thinner, certainly less than 5 m, so the solution above is not appropriate once the IBL reaches this thickness. If one assumes the IBL continued to grow at the maximum rate found at the outer edge of the surface layer, one can constrain the IBL depth for a given distance downstream. For day 220, assuming a roughness length of 0.01 m, the IBL reaches a depth of 5 m at a distance of at least 81 m downstream, close to the visual estimate of 100 m in Fig. 2.12. The agreement with this simple scaling strengthens the argument for vertical mixing of momentum. It seems that the boundary layer at this time can be approximated by a one-dimensional (horizontally homogeneous), unsteady boundary layer.

2.4.4 BULK, TIC, AND AMTV INTERCOMPARISON

As described, the bulk estimates of surface fluxes disagree substantially with the TIC data, even when adjusted for attenuation with depth. See section 2.3.3 and Fig. 2.15. The attenuation factor was derived through a similarity solution for flux profiles in a boundary layer stabilized by buoyancy flux. The heat balance estimate of salt flux was used, which was seen to be too small to account for mixed layer salinity changes. Assuming a surface buoyancy flux that includes an estimate of runoff more strongly attenuates the surface friction speed and heat flux and produces good agreement between day 211 and day 215,

especially at the lower cluster (not shown). However, this buoyancy flux is an order of magnitude larger than any data in Fig. 2.15c. The TIC salt flux is called into serious question since it is far less than the flux required for the observed salinity changes and is inconsistent with the TIC-observed heat flux and stress. It is possible that biofouling led to poor conductivity measurements and/or that the turbulent scales were too small to be resolved by the SBE-04 conductivity cell.

On day 219 and day 220, it appears the TIC data were more reliable. Average surface buoyancy flux was probably much smaller as the mixed layer salinity was fairly constant over the period following day 215. It could be that the TIC being cleaned more regularly or the lack of biological matter combined with the smaller buoyancy flux (and so larger scales) allowed the conductivity cell to make an accurate measurement. If so, the fresh water flux from surface melt was enough to cause the actual flux to significantly exceed the heat balance estimate.

The AMTV-derived heat flux qualitatively makes sense. Before day 215, most of the AMTV data segments were obtained under ice. Very few runs showed significant heat flux before the wind increase on day 207. Between day 207 and 215, the AMTV generally showed mixed layer heat flux values less than the surface value but in the same direction (upward) consistent with the attenuation of the heat flux with depth predicted by similarity theory. The exception is day 213, see the discussion of over-running overturns in section 2.4.2. After day 215, when most of the AMTV data were obtained under open water, heat fluxes in the mixed layer were downward because of radiative flux at the surface and the lack of ice to absorb heat by melting. Of course the ocean city TIC did not indicate downward fluxes as the site was far from open water.

Finally, we note that the AMTV-derived friction velocity agrees very well with the steady-state force balance estimate. The AMTV samples many surface types, so it provides a more representative measurement of spatial-average stress than a point measurement. Point measurements of stress close to the underside of sea ice can be difficult to use as representative of large-scale values

[*Wettlaufer*, 1991; *Morison et al.*, 1987]. As the lead-edge TIC data confirm, the choice of location for a point measurement of stress may result in different values for friction velocity. At SHEBA the lead-edge stresses were not representative of the mean conditions. It is important that in a spatially varying boundary layer the AMTV can accurately measure ice-ocean stress in addition to exchanges of heat and salt.

2.4.5 NUMERICAL MODEL MOTIVATION

The first-order closure model of *McPhee* [1987; 1992; *McPhee and Kantha*, 1989] is described below and used to make the case that vertical turbulent "diffusion" driven by a time-varying surface condition dominate the quasi-steady period. The model will be used to judge whether the observed heat and salt fluxes and characteristics of vertical water velocity (variance and characteristic wavenumber) are quantitatively consistent with the one-dimensional view. The model is also used to investigate the largest oceanic flux event of the summer from day 207-215. As we will see, observations at SHEBA on days 207-215 indicate the observed vertical mixing was deeper than predicted by the one-dimensional model. During the period, the large salt and heat fluxes were likely to be the strongest under leads. If there were a time when horizontal gradients were important, this would be it. The three-dimensional time-dependent model described below is required to investigate the importance of the new mixing mechanism in both the strong and weak fresh water flux scenarios.

We begin with an analytical description of the ice-ocean system that expresses conservation of momentum, temperature, and salinity. A description of a 1-D model, its previous uses, and results of boundary layer simulations follows. A 3-D model is described and compared with boundary layer observations.

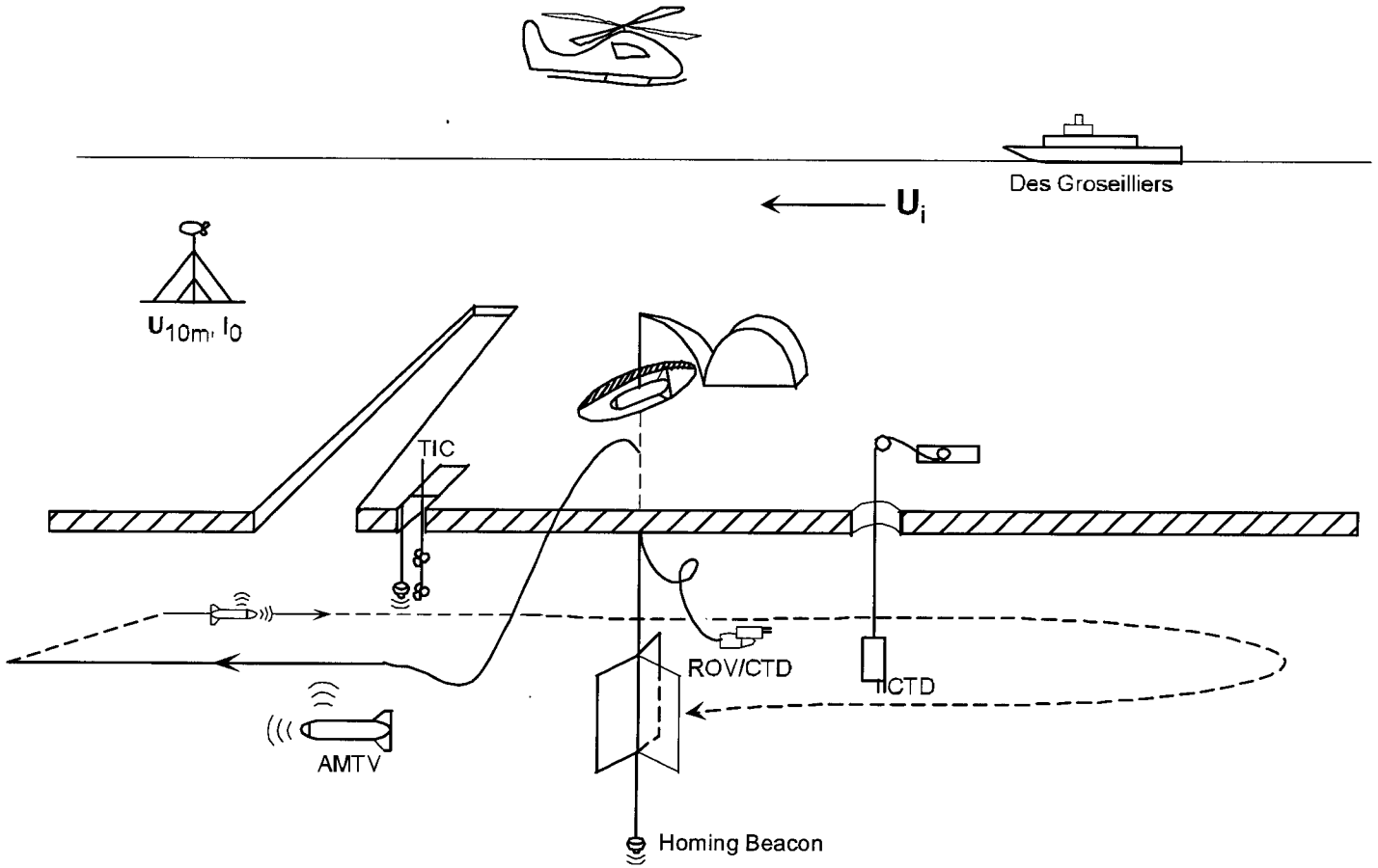

Figure 2.1. Cartoon of the summer lead sampling strategy. Instruments include an autonomous underwater vehicle (AMTV), remotely-operated vehicle (ROV--tethered), conductivity-temperature-depth (CTD) instruments, and turbulence instrument clusters (TIC). Other observations were: solar insolation, wind and ice velocity, aerial photography, and CTD and TIC deployments away from the lead.

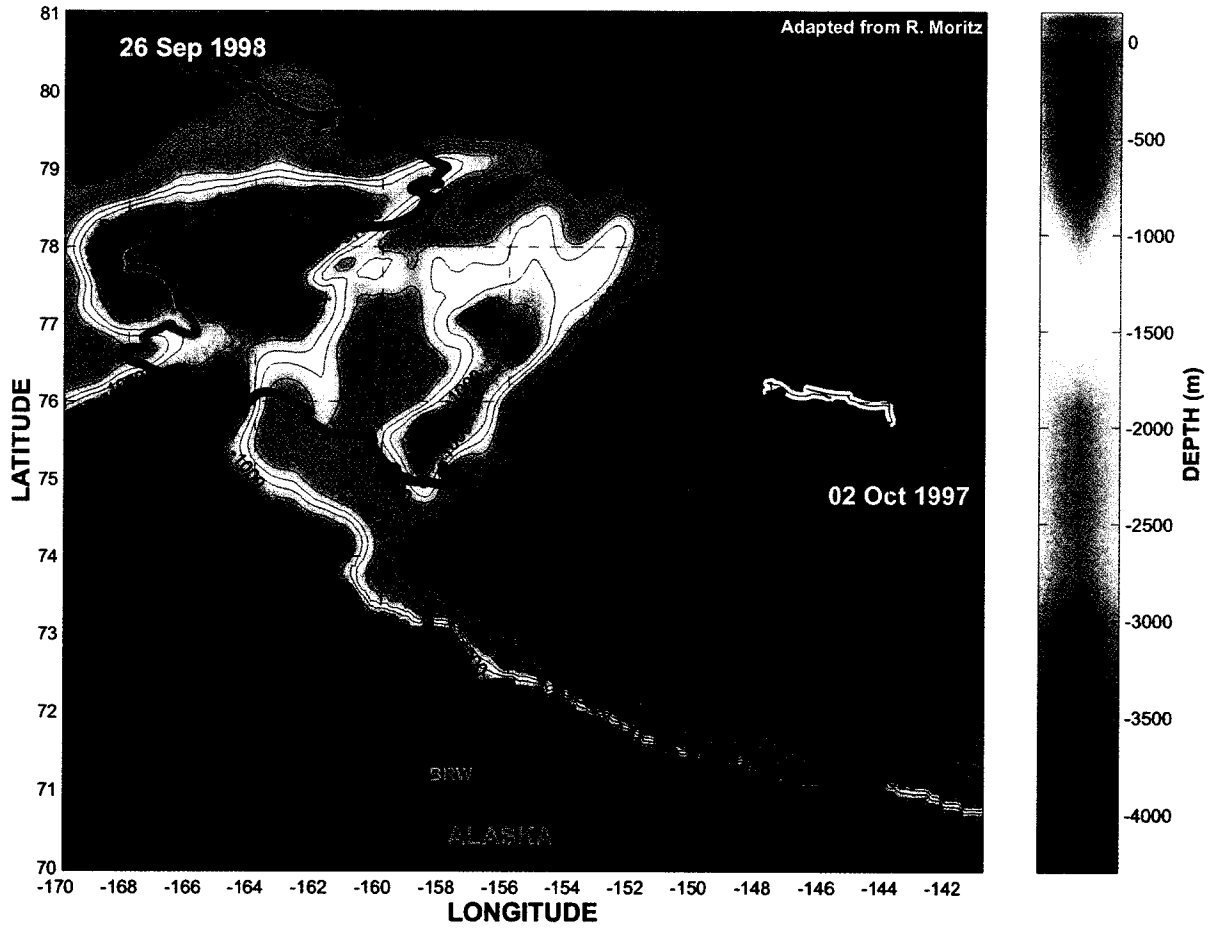

Figure 2.2. Drift of the SHEBA ice camp from October 2, 1997 to September 26, 1998. June, July, and August are blue, cyan, and black segments over Chukchi Cap. Positions: *Des Groseilliers* logbooks. Bathymetry: http://www7430.nrlssc.navy.mil.

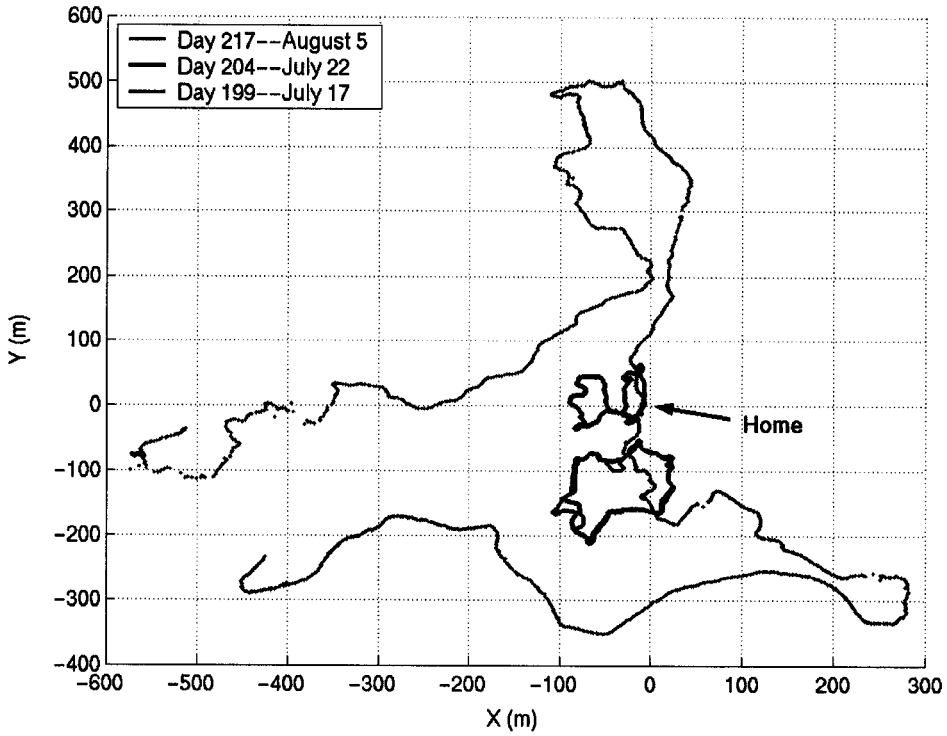

Figure 2.3. Outline of the SHEBA lead known as "Sarah's Lake" on three days in 1998. The location of the operations hut is at the origin. Lead perimeter was collected by tracking an acoustic beacon with the Applied Physics Lab tracking range. The beacon was towed with a small boat. The lead on day 217 was not mapped in its entirety.

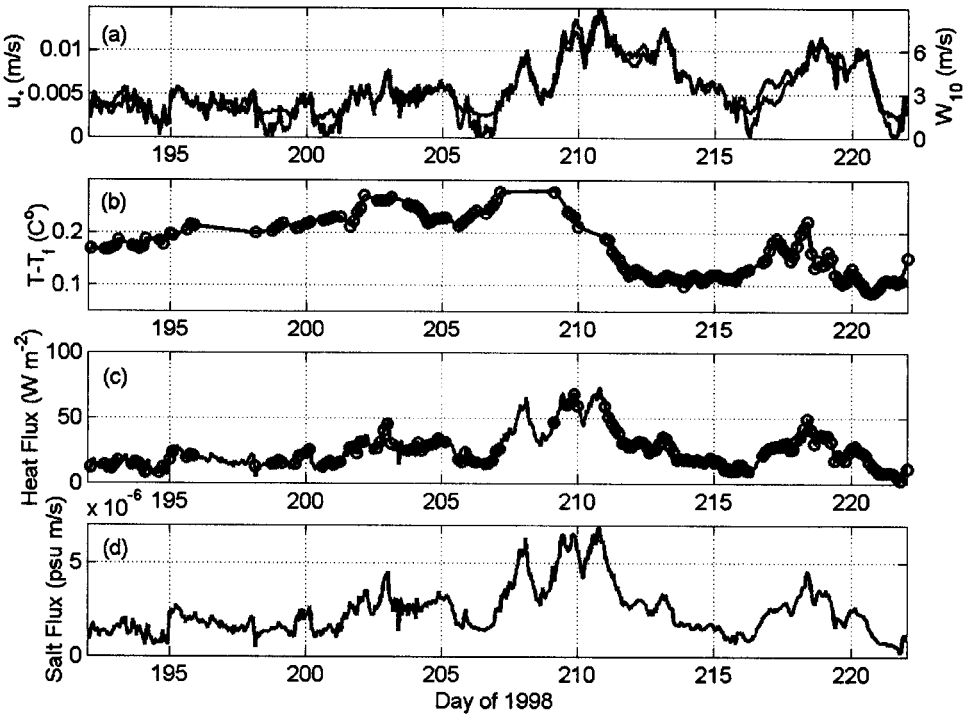

Figure 2.4. (a) Friction speed (blue) at the ice-ocean interface from the SHEBA Project Office wind speed at 10 m (red) and ice velocity, assuming a steady state balance. (b) Elevation above freezing temperature at 4 m depth. (c) Ice-ocean heat flux from bulk exchange relation, proportional to the product of (a) and (b). (d) Salt flux at ice-ocean interface assuming the bulk heat flux goes to melting ice of salinity 2 psu.

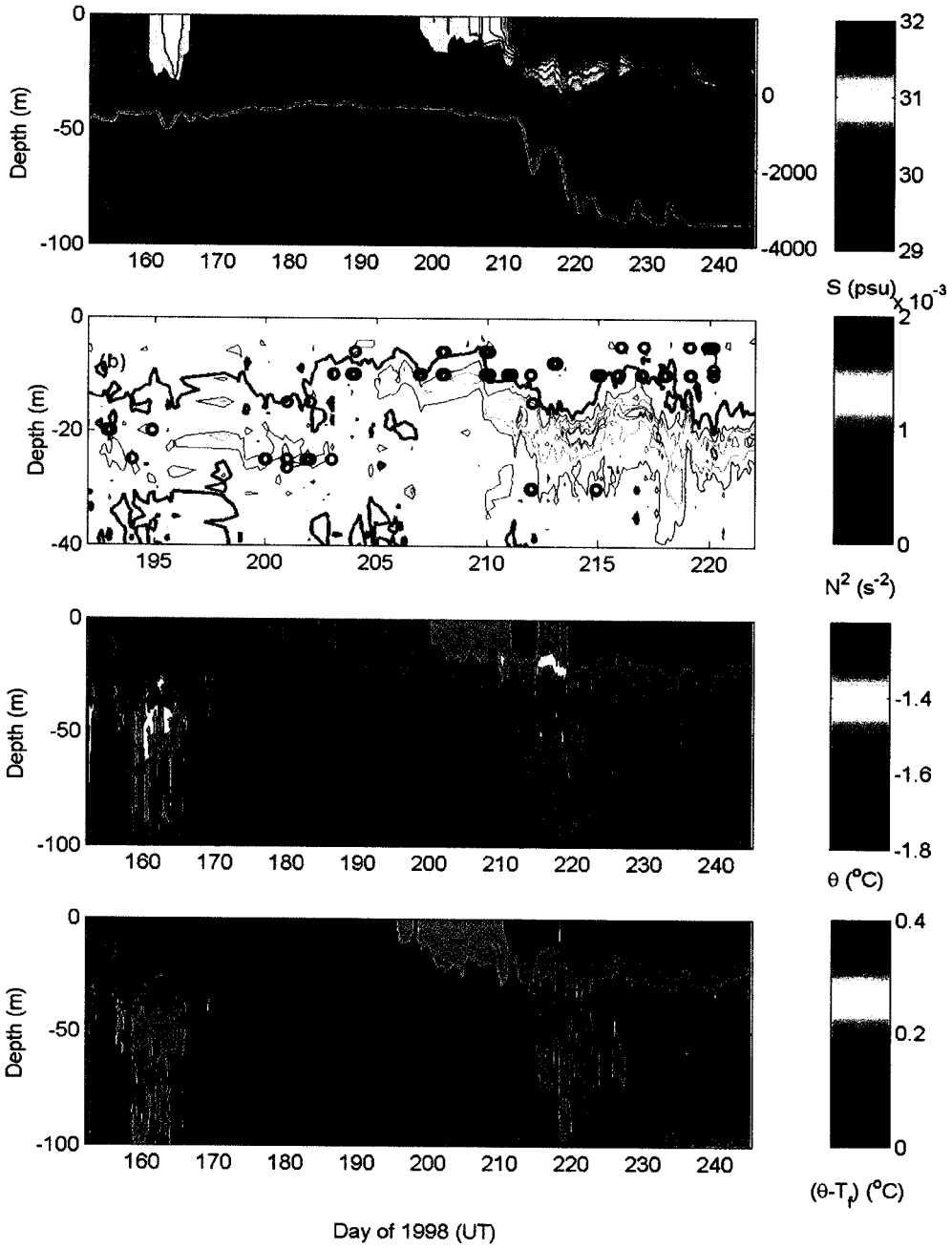

Figure 2.5. Ocean city CTD profiler salinity and ocean depth (a), buoyancy frequency in top 40 m (b), potential temperature (c), and potential temperature departure from surface freezing temperature (d). In (b), the $1x10^{-4}$ s^{-1} contour is the thick magenta line, and the black circles are AMTV run depths and times.

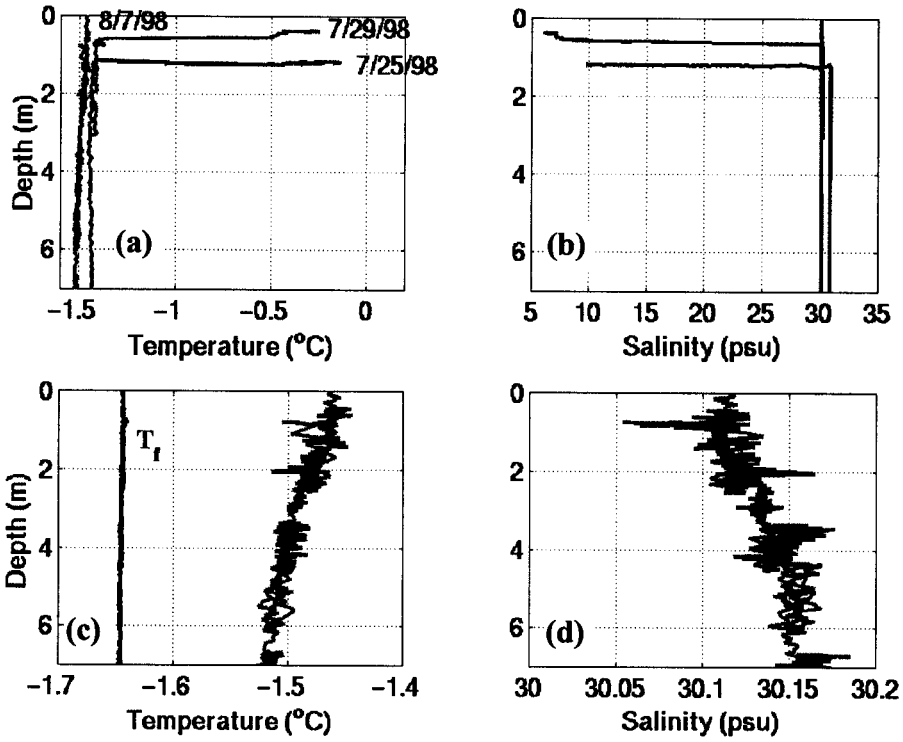

Figure 2.6. Remotely-Operated Vehicle profiles of temperature (a) and salinity (b) in the main SHEBA lead. On 7/25/98 (day 206) and 7/29/98 (day 210) the ROV could not float passively to the surface due to the strong stratification in the lead, so the profiles do not extend to the surface. The profiles on 8/7/98 (day 219) are shown in detail in (c) and (d), along with surface freezing temperature.

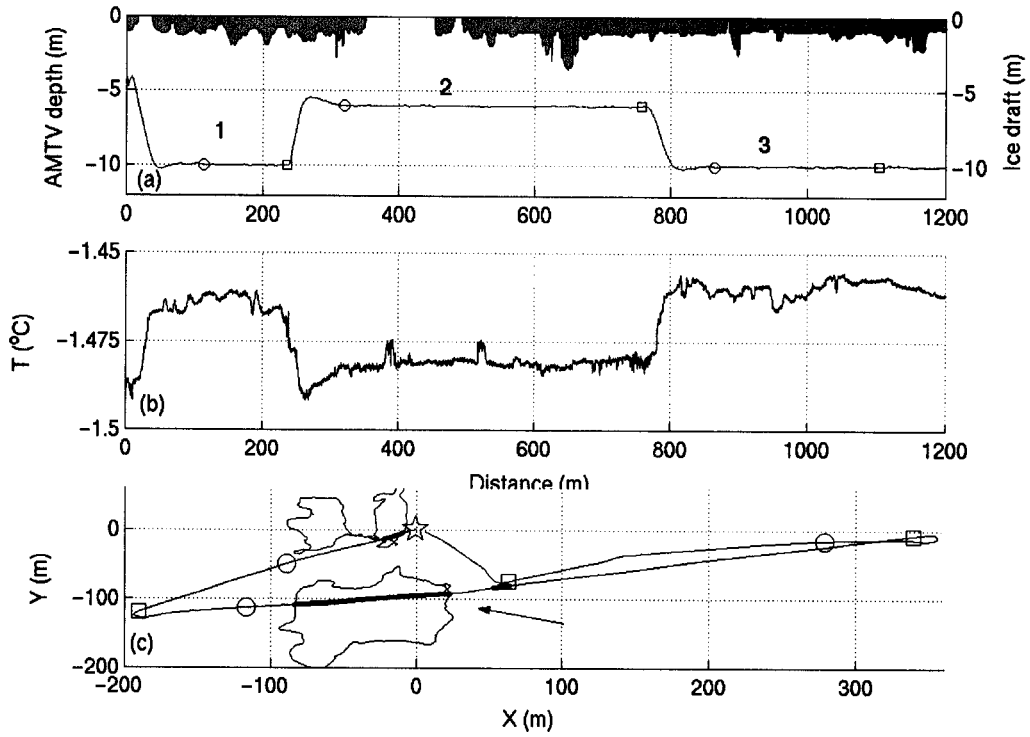

Figure 2.7. AMTV run on day 204.0 (UT). (a) Vehicle depth marked with symbols representing the start and finish of each leg. Also shown is the ice draft observed by the AMTV's upward-looking acoustic altimeter. (b) Temperature observed by the AMTV. (c) Horizontal position of the AMTV as recorded by an acoustic tracking range. The x and y axes are defined in the tracking range software and remained constant throughout the experiment. The same symbols as in (a) are used to indicate the segments of the run to be analyzed. The outline of the lead is shown, as well as the ice velocity of 6.4 cm s^{-1}. The open water returns from the altimeter are plotted with thicker line segments.

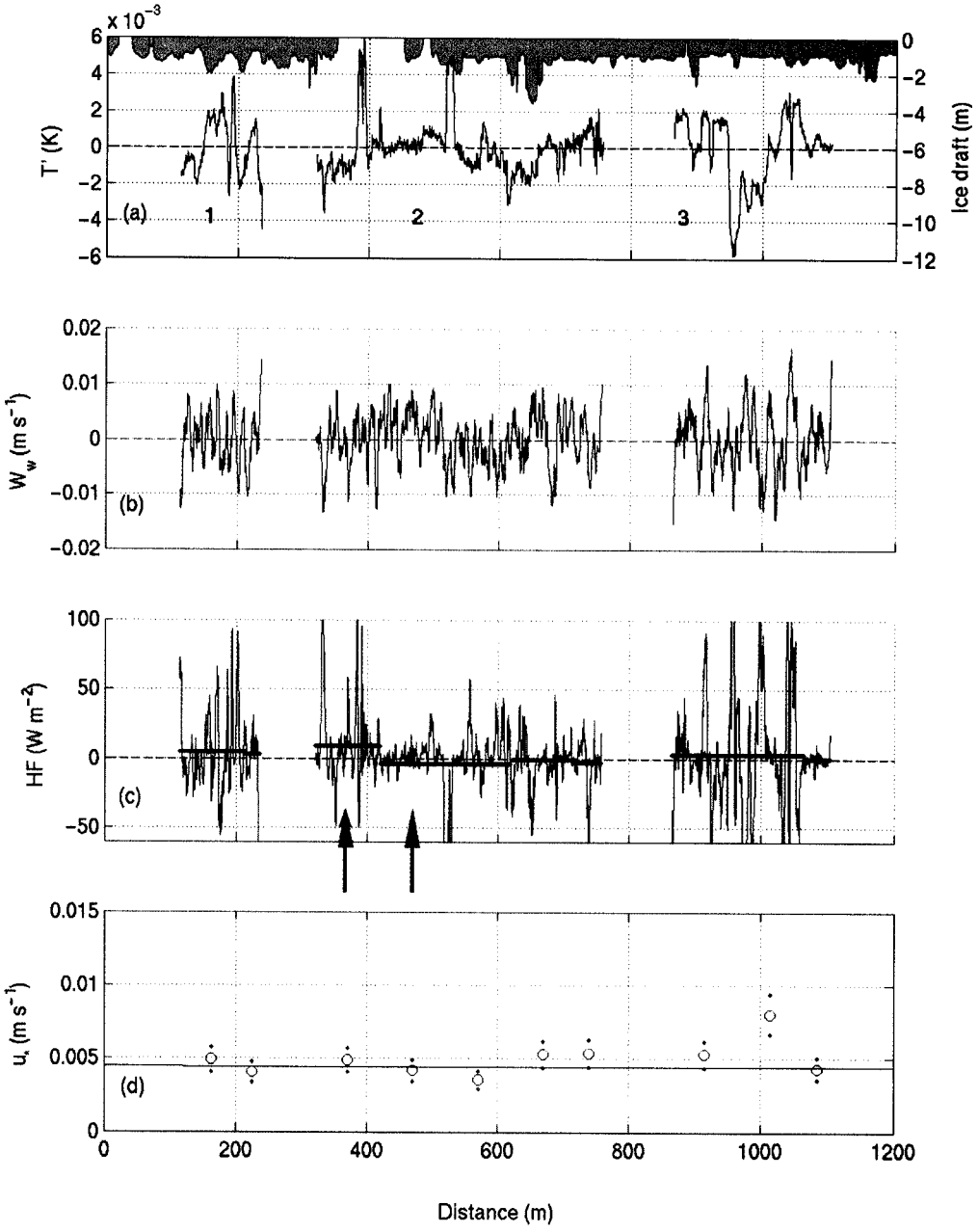

Figure 2.8. AMTV run on day 204.0, turbulent quantities. (a) Detrended temperature for each leg and ice draft. (b) Vertical water velocity calculated from vehicle motion. (c) Heat flux with 100 m bin averages shown as horizontal bars. Only the two indicated are significant (10 and -3 W m^{-2}). (d) Friction speeds from the spectra of vertical water velocity and the 95% confidence interval.

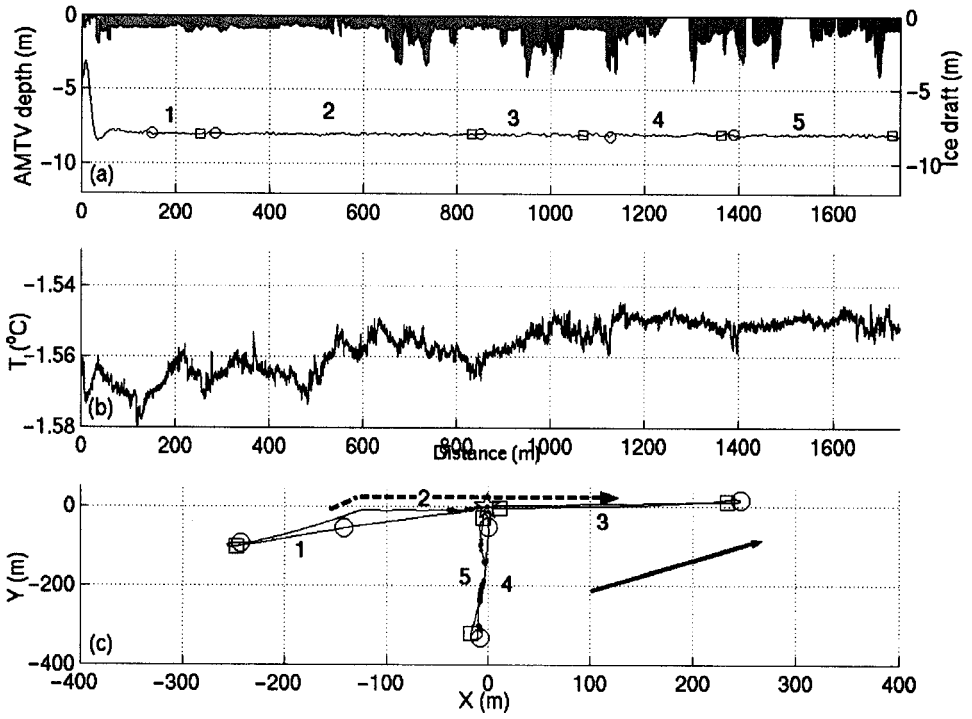

Figure 2.9. AMTV run on day 213.0 (UT), as in Fig. 2.7. At this time the lead was nearly closed. As before, the solid arrow indicates the ice velocity. The AMTV crossed a ridge at around +200 m on the x-axis.

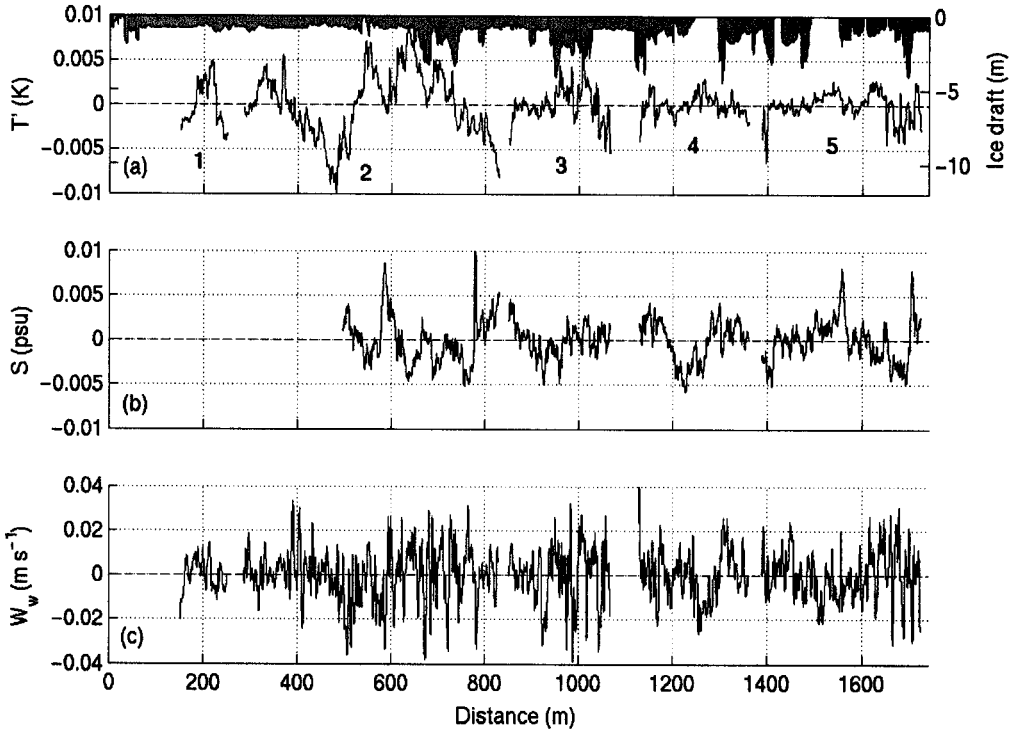

Figure 2.10. AMTV run on day 213.0, as in Fig. 2.8, except salinity deviations are plotted for legs where available.

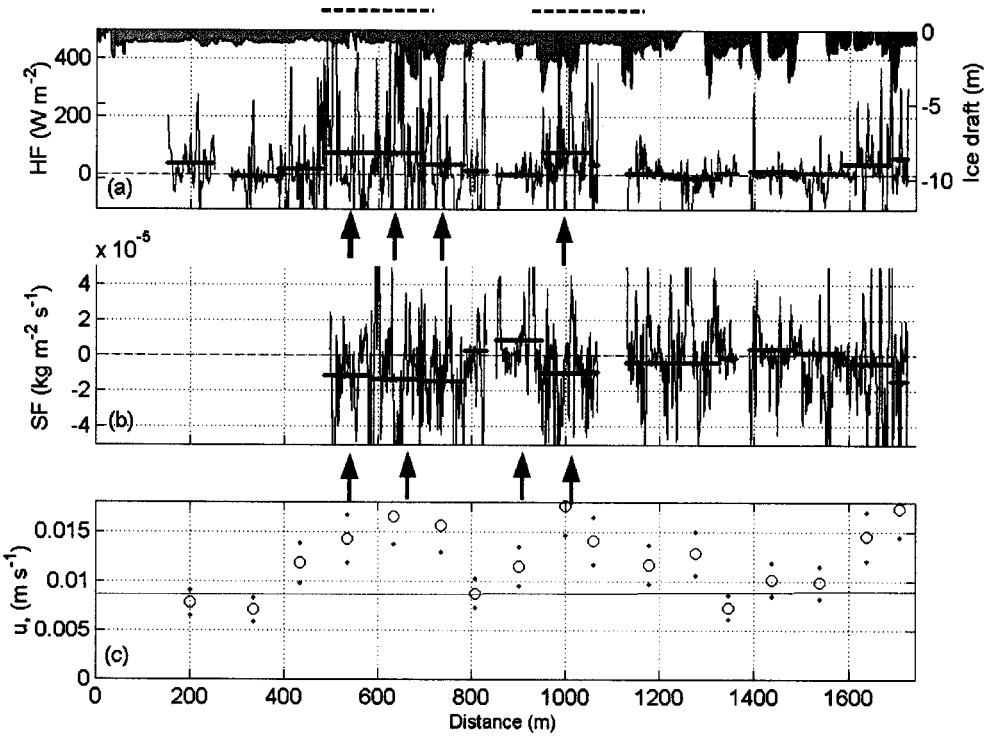

Figure 2.11. AMTV run on day 213.0, as in Fig. 2.8, except salt flux is also plotted. Significant heat flux is observed at the 500 m, 600 m, 700 m, and 900 m bins (73, 72, 31, 74 W m^{-2}). Significant salt flux is observed at the 500 m, 600 m, 900 m, and 1000 m bins (-1.1, -1.3, +0.82, -1.0x10^{-5} kg m^{-2} s^{-1}). These segments are under and downstream of the ridge as indicated by the dashed line.

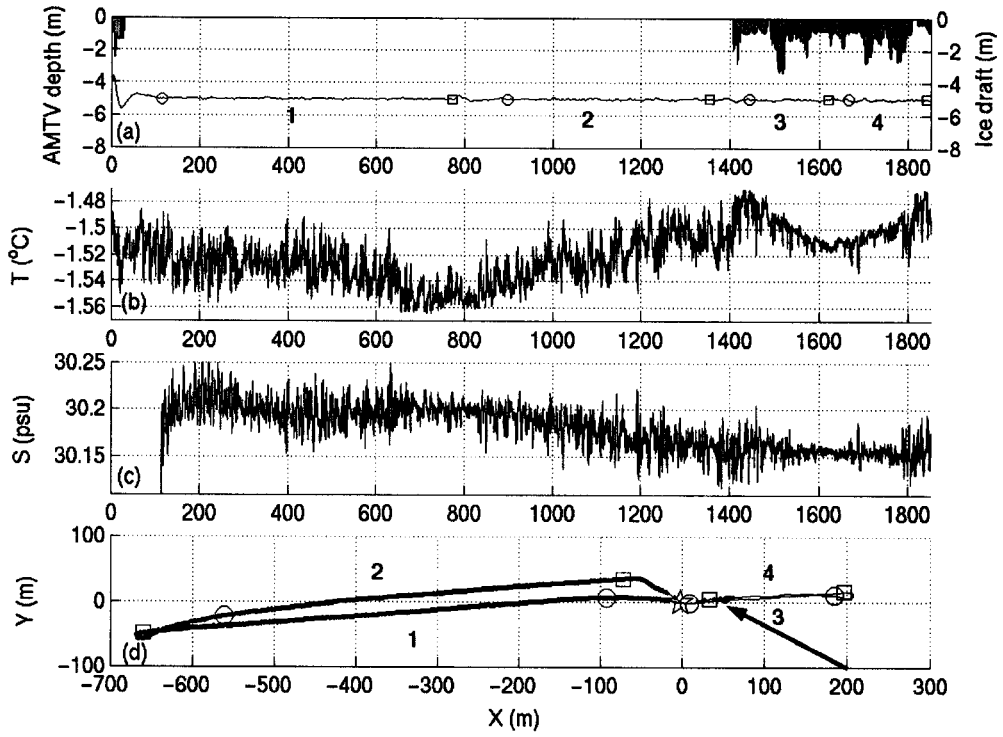

Figure 2.12. AMTV run on day 219.9 (UT). As in Fig. 2.7, except salinity is available. The lead was more than 700 m wide.

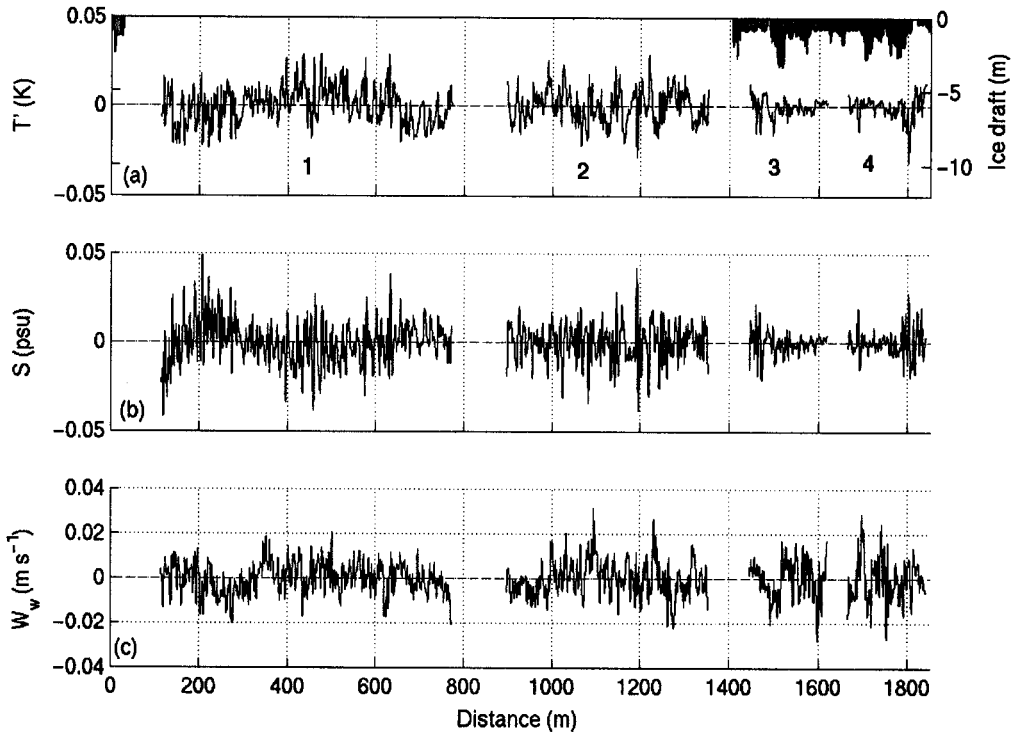

Figure 2.13. AMTV run on day 219.9. As in Fig. 2.10.

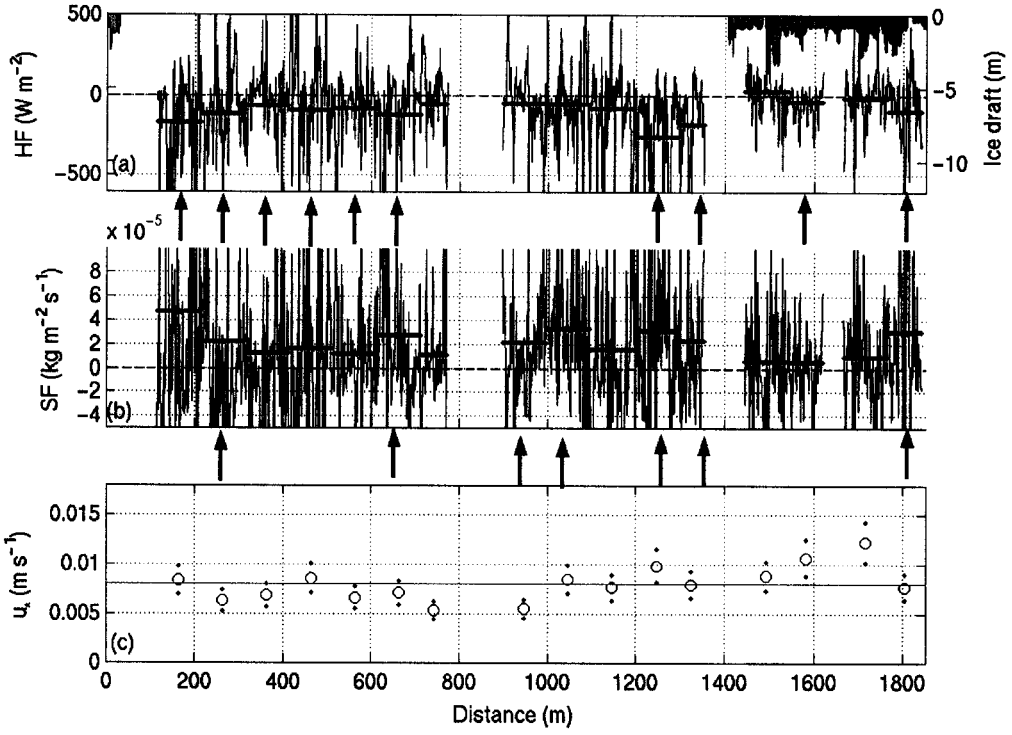

Figure 2.14. Fluxes for AMTV run on day 219.9. As in Fig. 2.11. Most of the bins show statistically significant fluxes as indicated. The lead fluxes of heat and salt averaged 98 and 144 W m^{-2} and 1.7 and 2.4x10^{-5} kg m^{-2} s^{-1} (segments one and two). Segment three did not pass the significance test for heat or salt flux, and segment four only had significant salt flux: 1.9x10^{-5} kg m^{-2} s^{-1}. The segment averages reported here are calculated from the covariances over each entire segment, not the average of the 100 m segments. The first 200 m of segment one were not included as it appears to have been contaminated by salinity drift (see Fig. 2.13).

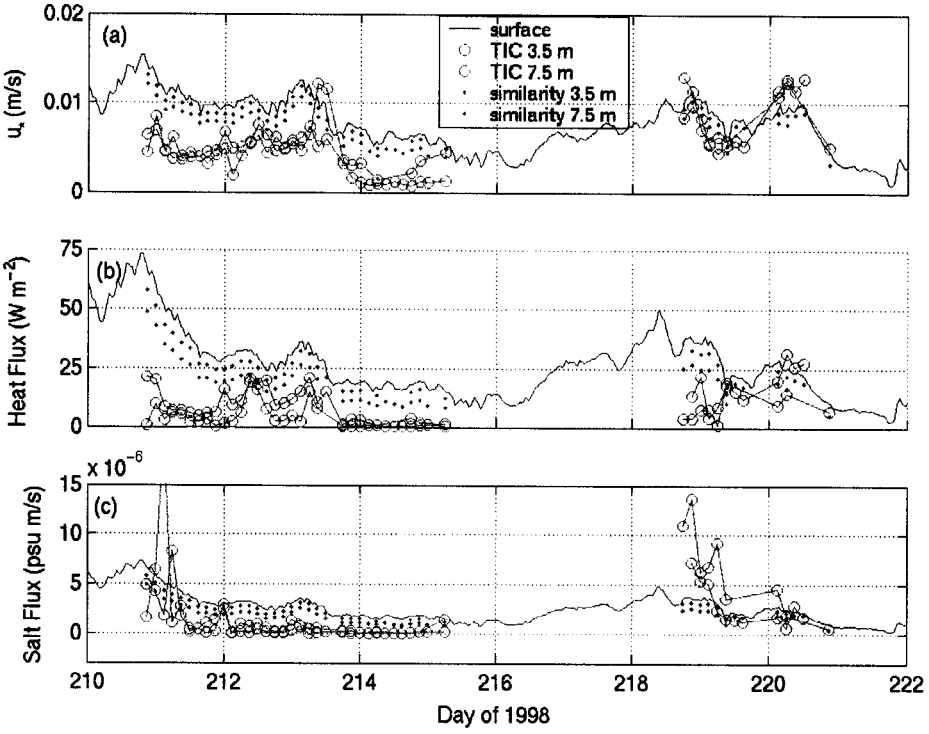

Figure 2.15. (a) Turbulence Instrument Cluster (TIC) observed friction speed at 3.5 m (red) and 7.5 m (green) compared to surface friction speed from force balance relation. The small dots are friction speed at the cluster depths extrapolated from the surface value using similarity theory. (b) TIC observed heat flux, compared to bulk estimate of surface heat flux and similarity predictions. (c) TIC observed salt flux comparison. Surface value based purely on thermal balance (no runoff).

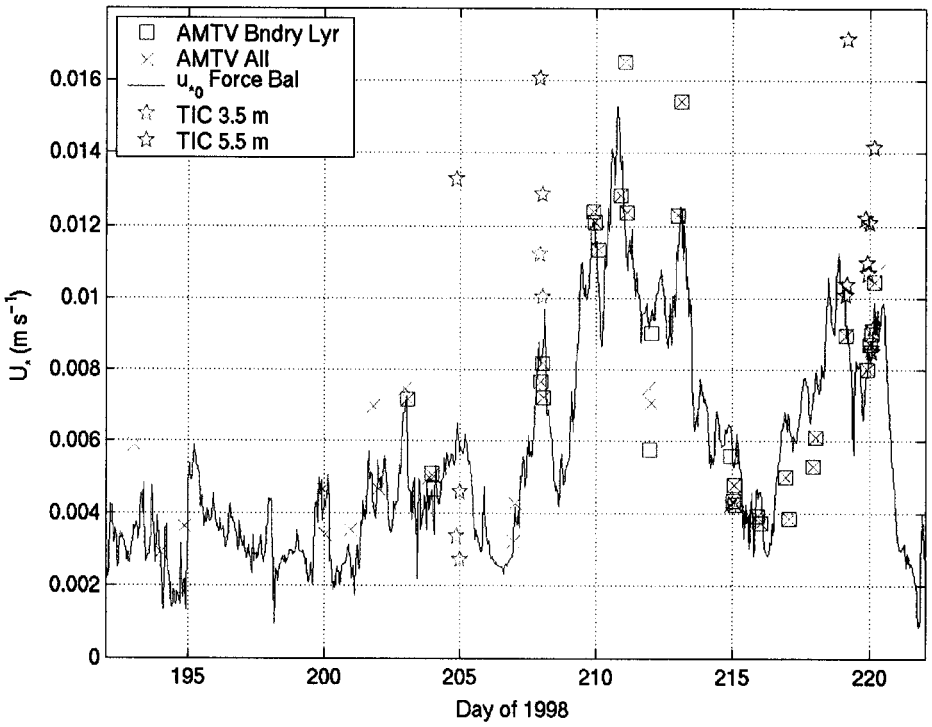

Figure 2.16. Ice-ocean interface friction speed from steady-state balance of wind stress and Coriolis force compared to all AMTV run averages (pink crosses), AMTV run averages using only boundary layer points (red squares), and lead-edge TIC observations (3.5 m blue stars and 5.5 m green stars).

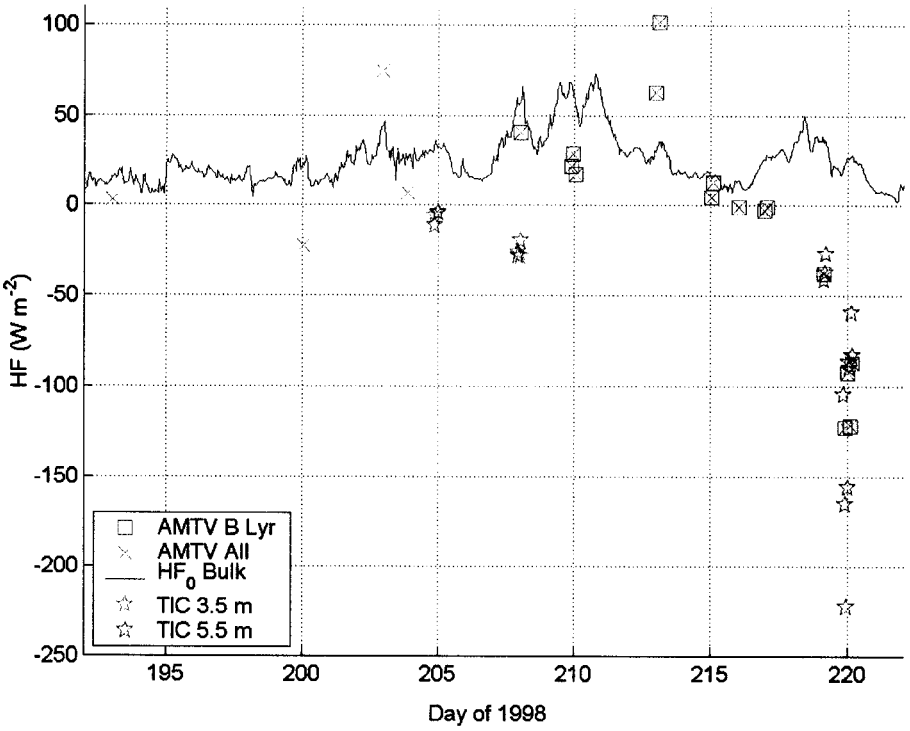

Figure 2.17. Ice-ocean heat flux from bulk estimate, and heat flux in the mixed layer from AMTV, and lead-edge TIC. Bulk heat flux is based on elevation of mixed layer above freezing and surface friction velocity from Fig. 2.16. Only values of AMTV heat flux that passed the significance test are shown. After day 215, the AMTV was predominantly in open water where downward heat fluxes were observed.

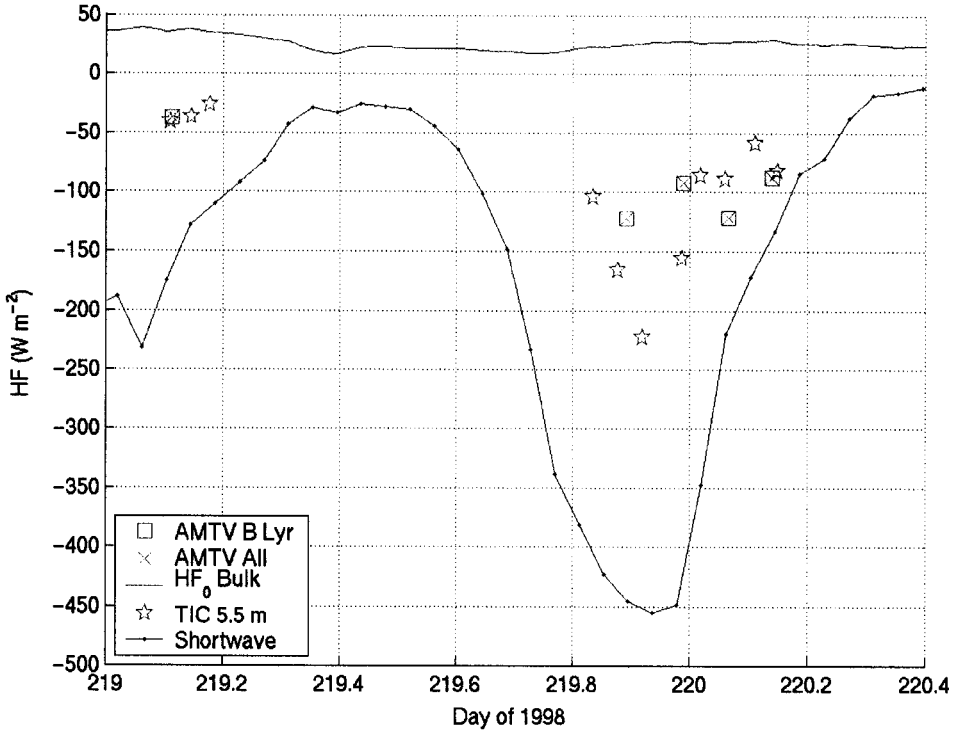

Figure 2.18. Detailed view of heat flux on days 219-220. Blue line with dots is the downward shortwave radiation measured just above the ice surface by the SHEBA Project Office. AMTV and lead-edge TIC heat fluxes correspond well to the radiative flux.

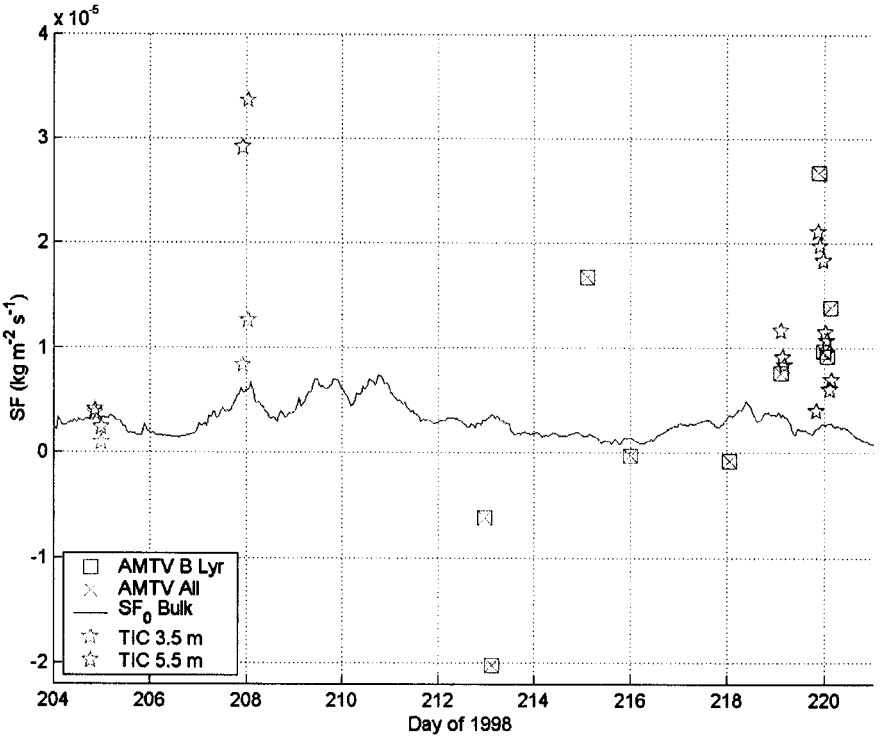

Figure 2.19. Salt flux in the upper ocean at SHEBA. Bulk estimate (blue line) is the melting due to the bulk heat flux in Fig. 2.17. The conductivity cell was not operating correctly before day 213. Only AMTV values that passed the significance test are included in the averages shown. The AMTV sampled mostly open water after day 215 where upward salt flux was typically observed by both instruments.

3. MODELING STUDIES

3.1 ANALYTICAL FORMULATION

Both models in this study use conservation equations written for the mean quantities with the vertical coordinate positive upward. An incompressible, Boussinesq fluid is assumed. Reynold's decomposition is carried out, which means that there must be a separation in scale between a "mean" signal and a "turbulent" signal (the latter indicated by a single prime). The momentum, temperature, and salt fluxes are expressed as covariances among the turbulent variables. The method used here to determine these covariances from mean properties (turbulent closure) is first order closure, meaning the fluxes are related to the gradients in the mean properties through turbulent diffusion coefficients. The primes on pressure and density indicate deviations from the mean, stationary state. The mean vertical density profile and associated pressure profile are subtracted from their actual profiles.

$$\frac{\partial \mathbf{u}}{\partial t} + \mathbf{u}\cdot\nabla\mathbf{u} + f\hat{\mathbf{k}}\times\mathbf{u} = -\frac{\nabla p'}{\rho_0} + \nabla\cdot\boldsymbol{\tau} - \frac{g\rho'\hat{\mathbf{k}}}{\rho_0} \tag{3.1}$$

where $\tau_i = -\langle u_i' u_j' \rangle n_j$ is the i-component of stress and $\mathbf{n}$ is the unit vector (summation over j is understood)

$$\nabla\cdot\mathbf{u} = 0 \tag{3.2}$$

$$\frac{\partial T}{\partial t} + \mathbf{u}\cdot\nabla T = -\nabla\cdot\mathbf{F}_T + Q_T \tag{3.3}$$

where $\mathbf{F}_T$ is the kinematic heat flux: $\mathbf{F}_T = \langle u'T' \rangle\hat{\mathbf{i}} + \langle v'T' \rangle\hat{\mathbf{j}} + \langle w'T' \rangle\hat{\mathbf{k}}$

and Q_T is a radiative heating term: $Q_T = \frac{I_z}{L}\exp(\frac{z}{L})$, where L is an extinction depth equal to 4 m and I_z is the shortwave flux at the ocean surface.

$$\frac{\partial S}{\partial t} + \mathbf{u} \cdot \nabla S = -\nabla \cdot \mathbf{F}_S \tag{3.4}$$

where $\mathbf{F}_S$ is the salt flux: $\mathbf{F}_S = \langle u'S' \rangle \hat{\mathbf{i}} + \langle v'S' \rangle \hat{\mathbf{j}} + \langle w'S' \rangle \hat{\mathbf{k}}$

Boundary conditions depend upon the particular problem of interest, but in general, we will specify fluxes of momentum (u_{*0}), heat ($\langle w'T' \rangle_0$), and salt ($\langle w'S' \rangle_0$) at the ice-ocean interface or the atmosphere-ocean interface (for open water).

In general, density depends on temperature, salinity, and pressure through the nonlinear equation of state, but for our purposes density is a simple linear function of salinity:

$$\rho = 0.808S + 1000 \tag{3.5}$$

It is acceptable here to neglect effects of temperature on density because near the freezing point, the thermal expansion coefficient of seawater is much smaller than the saline contraction coefficient. Pressure effects are small because we are concerned with surface mixed layer processes.

3.2 ONE-DIMENSIONAL MODEL

3.2.1 MODEL DESCRIPTION

Results from previous studies show that in many cases, a one-dimensional, first-order closure model for the stratified oceanic boundary layer simulates observations well. In particular, *McPhee* [1987] and *Mcphee et al.* [1987] successfully used similarity scaling arguments and a time-dependent 1-D model to describe the under-ice boundary layer during the 1984 Marginal Ice Zone Experiment (MIZEX). His model [*McPhee*, 1999] agreed well with a subset of the observations and with the results of the level 2.5 model of *Mellor and Yamada* [1974; 1982]. *McPhee and Kantha* [1989] extended the model to include internal

wave generation by sea ice, which helped explain the high ice-ocean drag during a later period of MIZEX. *Morison et al.* [1992] used the model to examine unstable "forced" convection from leads, with reasonable results. *McPhee* [1994, 1999] demonstrated some interesting features of Weddell Sea mixed layer development with the one-dimensional model. The model of this section is similar to that of *McPhee* [1987] and is recapitulated here with some modifications.

The model assumes purely horizontal and horizontally homogeneous flow. Velocity is expressed in a reference frame moving at a far-field velocity (beyond influence of the boundary). The vertical velocity vanishes because of Eq. 3.2 and a w=0 top boundary condition. The mean momentum equation then reduces to the following.

$$\frac{\partial \mathbf{u}}{\partial t} + f\hat{\mathbf{k}} \times \mathbf{u} = \frac{\partial \boldsymbol{\tau}}{\partial z} = \frac{\partial}{\partial z}\left(K \frac{\partial \mathbf{u}}{\partial z}\right) \text{ where } \mathbf{u} \text{ is the horizontal velocity } (u,v,0) \qquad (3.6)$$

The conservation equations for temperature and salinity are:

$$\frac{\partial T}{\partial t} = -\frac{\partial}{\partial z}\langle w'T' \rangle + Q_T = \frac{\partial}{\partial z}\left(\alpha_T K \frac{\partial T}{\partial z}\right) + Q_T \qquad (3.7)$$

$$\frac{\partial S}{\partial t} = -\frac{\partial}{\partial z}\langle w'S' \rangle = \frac{\partial}{\partial z}\left(\alpha_S K \frac{\partial S}{\partial z}\right) \qquad (3.8)$$

Vertical fluxes are modeled as vertical property gradients multiplied by an eddy exchange coefficient, K. For temperature and salinity, this is multiplied by the ratio of turbulent heat or salt diffusivity to eddy viscosity (the turbulent Prandtl and Schmidt numbers, respectively). A first-order turbulent closure model [*McPhee,* 1981; 1994] specifies the eddy viscosity as the product of characteristic turbulent velocity and local turbulent mixing length:

$$K = u_* \lambda \qquad (3.9)$$

The local friction velocity, u_*, is the square root of the local stress, calculated from a previous estimate of eddy viscosity and the velocity shear profile.

$$u_* = \sqrt{|\boldsymbol{\tau}|} = \sqrt{K\left|\frac{\partial \mathbf{u}}{\partial z}\right|} \tag{3.10}$$

The friction velocity is set to a constant value in the surface layer.

McPhee [1994] develops the mixing length calculation for the stable or neutral mixed layer. In the inner layer, observations support the assumption of linear growth of the mixing length, λ, with distance to a maximum value [*McPhee*, 1981]. The maximum value in the mixed layer is calculated based on interfacial surface stress and planetary rotation and is bounded by stabilizing buoyancy flux through the stability parameter, η_*, which is less than or equal to one.

$$\lambda = \min(\kappa|z|, \Lambda_* u_{*0} \eta_*^2 f^{-1}) \tag{3.11}$$

$$\eta_*^2 = (1 + \frac{\Lambda_* u_{*0}}{\kappa f R_c L_0})^{-1} \tag{3.12}$$

The mixing length retains the constant value throughout the mixed layer, below which it is reduced in the strong stratification of the pycnocline. There the mixing length is calculated from Eqs. 3.11 and 3.12 using the local buoyancy flux and local stress. The closure expressions are arrived at through scaling the steady momentum equation appropriately for the boundary layer, making use of an assumption that the nondimensional eddy viscosity is a universal constant away from the interface (in the outer layer) [*McPhee*, 1981].

Turbulent Schmidt and Prandtl numbers are calculated using a gradient Richardson number approach, outlined in *McPhee* [1994]. They are assumed to be equal in this model, and when vertical shear is strong, they are equal to one:

$$\alpha_S = \alpha_T = \begin{cases} 1, & Ri \le 0.079 \\ \exp(-1.5\sqrt{Ri - 0.079}), & 0.079 < Ri < 5 \\ 0.039, & Ri > 5 \end{cases} \tag{3.13}$$

$$Ri = \frac{-\frac{g}{\rho_0}\frac{\partial \rho}{\partial z}}{\left|\frac{\partial \mathbf{u}}{\partial z}\right|^2} \tag{3.14}$$

The boundary layer is viewed as a single column, with surface boundary conditions varying as the ice-lead system passes over. Boundary conditions at the surface are heat flux, salt flux, momentum flux (stress), and roughness, which can all vary in time. Stress is specified in the model in the form of surface friction speed, u_{*0}, and roughness length, z_0, is also specified. Heat flux at the interface is made up of two terms: the downwelling shortwave radiation and ice-ocean heat flux when water temperatures above freezing in the mixed layer contact the ice boundary. The former is distributed in an absorbing layer via the heating term with an extinction depth of 4 m. The latter is calculated from the bulk heat flux transfer model (Eq. 2.8) [*McPhee,* 1992]. Salt flux is also made up of two terms: a percolation velocity and salt flux due to interfacial melting. The former is a specified velocity of the interface (upward) due to fresh meltwater entering the top via runoff or percolation through the pack ice. The latter component of salt flux is calculated using the salinity boundary relation of Eq. 3.15 (a more complete version of Eq. 2.9) *McPhee* [1990]. Conduction through the ice is assumed negligible here.

$$\langle w'S' \rangle_0 = \langle w'T' \rangle_0 \Delta S q_l^{-1} + \Delta S (w_{perc} + F_{cond} q_l^{-1}) \tag{3.15}$$

where $\Delta S = S_{ml} - S_{ice}$ and $q_l = 83.8(1 - 0.03 S_{ice})$. Bottom boundary conditions are zero flux conditions for momentum, temperature, and salinity.

Initial conditions on temperature and salinity profiles are set, usually according to an observed set of profiles. Initial conditions for velocity and eddy viscosity are not as straightforward. The steady version of the one-dimensional momentum equation is solved with an initial estimate of eddy viscosity. This solution is then used to recalculate mixing length and friction velocity profiles, together giving a new eddy viscosity profile. The steady solution is calculated again, and this process is iterated to convergence for initialization of velocity and eddy viscosity.

It is possible to view the 1-D, horizontally homogeneous unsteady boundary layer as a 2-D steady boundary layer. *Mellor et al.* [1986] and *Morison et al.* [1992] apply the transformation discussed here. The boundary conditions and boundary layer equations are transformed to a coordinate system moving with the ice in the negative x direction at constant speed U_i. Let x^* represent the horizontal distance in the x direction downstream of an arbitrary point in the ice pack:

$$x^* = U_i t + x \tag{3.16}$$

Equation 3.6 becomes

$$U_i \frac{\partial \mathbf{u}}{\partial x^*} + f\hat{\mathbf{k}} \times \mathbf{u} = \frac{\partial}{\partial z}\left(K \frac{\partial \mathbf{u}}{\partial z}\right) \quad \text{where } \mathbf{u} = (u,v,0) \tag{3.17}$$

It is important to realize that Eq. 3.17 does not violate the horizontal homogeneity assumption because it is only a transformation of Eq. 3.6. A vertical profile at

some value of x^* is still assumed to be the solution to the horizontally homogeneous equations. It depends on the boundary conditions at that location and the solution at a neighboring value of x^* that acts like the solution at the previous time step. It represents the spatial variation associated only with the temporal variation of the 1-D boundary layer profile. Gradients in the new horizontal variable are not used in the advective terms of the momentum equation, so for an accurate solution these gradients must be small. Unlike time-dependent solutions, those expressed in terms of x^* can be compared directly to AMTV data, since they are both expressed in horizontal distance related to the ice pack.

3.2.2 RESULTS AND DISCUSSION—DAY 220

A two-dimensional steady simulation of the lead around solar noon of day 219, 1998 is shown in Fig. 3.1. The model domain is 4.25 km in the horizontal by 30 m in the vertical with 0.15 m spacing in the vertical and 5 min time steps (corresponding to 51 m in the horizontal for the average ice velocity of 0.17 m s^{-1} to the left). The model lead is a 1.25 km segment in the upper left with incoming shortwave radiation of 448 W m^{-2}, extinction depth of 4 m, and albedo of 0.08. The lead is further specified by a surface friction velocity of $8x10^{-3}$ m s^{-1} towards the left, a roughness length of $2.7x10^{-5}$ m, and a fresh water input equivalent to 0.5 cm day^{-1} surface melt over an 80% ice-covered ocean draining into the remaining 20% lead fraction (a salt flux in the lead of $6x10^{-6}$ kg m^{-2} s^{-1}). The surface stress and roughness length were calculated using the observed 10-m wind speed and techniques from *Steele et al.* [1989]. The fresh water input due to surface melt is determined from measurements of the ablation rate [*Perovich et al.*, 2003]. The salinity of the ice is taken to be 0.5 psu [*Eicken et al.*, 2002]. The top boundary conditions under ice downstream of the lead do not include any source of meltwater other than bottom melt, and the radiative flux is zero. The surface friction velocity and roughness length increase to 0.01 m s^{-1} (still towards the left) and 0.01 m, calculated from observed ice velocity using a Rossby

similarity law and a representative value for sea ice, respectively. The initial temperature and salinity profiles represent those measured at the lead edge during the AMTV run with the Sea-Bird SBE-19 CTD: a 15-meter mixed layer with temperature of more than 0.1 C^o above the freezing temperature.

Results show that, like the AMTV observations, the temperature at 5 m increases steadily as the downstream lead edge is approached from upstream, then falls and levels off under the ice. As discussed above, this is consistent with continuous solar heating and mixing down of the surface water. Figure 2.12 shows the temperature observed (also around solar noon) by the AMTV at 5 m increased at a rate of about 0.01 deg per 100 m in the lead, while the model results indicate a rate of about half that value. Also, the 5-m observed temperature decreases downstream of the ice edge more quickly: $0.02C^o$ over 100 m compared $0.02C^o$ over 1000 m in model. Despite the difference in horizontal temperature gradient, the model reproduces a qualitatively correct temperature structure.

The model heat flux in the lead at 5 m is about 100 W m^{-2} downward over the 500 m just before the lead edge, compared to an average of 98 W m^{-2} and 144 W m^{-2} for the AMTV over the two large lead segments on day 219.9. Downstream, under the ice, the model heat flux at 5 m strengthens as the rough ice surface rapidly mixes down the warmer surface water. The heat flux at 5 m then relaxes slowly as the vertical temperature gradient weakens, eventually becoming upwards about 2 km downstream of the lead edge. The heat flux at 10 m remains downward throughout the run and is more downward than the 5 m heat flux between 1 km and 2 km. The AMTV heat flux observations indicate a much faster decay of heat flux under the ice. While the 100 m of AMTV data just downstream of the edge show a strong downward flux of 97 W m^{-2} at the very end of the run, the segment 100-400 m downstream of the lead edge averaged 40 W m^{-2} and there were two segments with insignificant fluxes. The model downward

flux remains greater than this level until about 1.2 km downstream of the lead edge.

The salinity at 5 m shows a freshening also consistent with vertical mixing of fresh water input at the surface of the lead. The freshening trend weakens under the ice, since the source of fresh water (basal melting) is weaker than the surface melt drainage flux in the lead. The absolute salinity observations from the AMTV in Fig. 2.12 have been contaminated by a low frequency drift, which makes comparison with the model difficult. However, the trend in salinity from the turn-around point at 800 m is in the same sense as the model: freshening as the lead edge is approached from upstream. Any trend before the turn-around point was lost in the attempt to correct for the sensor drift. The salinity deviations are unaffected by the low-frequency sensor drift, allowing the calculation of salt flux. The salt flux in the last 500 m of the model lead averages to 0.4×10^{-5} kg s^{-1} m^{-2} upward. The AMTV salt flux was 1.7×10^{-5} kg s^{-1} m^{-2} and 2.4×10^{-5} kg s^{-1} m^{-2} upward for the two 500 m lead segments. The model seems biased low; perhaps the freshwater flux in the lead was greater than the value used in the lead boundary condition. In the 100 m downstream of the lead edge, the model salt flux under the ice at 5 m increases to about 0.8×10^{-5} kg s^{-1} m^{-2} and decreases gradually. The observed under-ice flux on day 219.9 (taking the covariance over all of segment 4) gives 1.9×10^{-5} kg s^{-1} m^{-2} , while the segment 3 covariance does not pass significance test. Besides the difference in flux magnitude between the model and observations, the model shows an increase in salt flux relative to the lead, while the observations indicate a moderate decrease relative to the lead.

The modeled mixing length and stress can also be compared to the observed. The modeled mixing length at 5 m is about 0.5 m in the lead, increasing to 0.8 m under the ice and decreasing gradually with downstream distance. The increase in modeled length scale from lead to ice boundary conditions is due to the reduction in stabilizing buoyancy flux and increase in stress at the surface. The observations do not show a clear pattern, but they are in

rough agreement with the model. By Eq. 2.4, the mixing length in the lead at 5 m is 0.7 m with a maximum under the ice edge of 1.8 m.

The model shows an increase in friction speed at 5 m from 0.6 cm s^{-1} to 0.8 cm s^{-1}, corresponding to the specified jump in surface friction from open water to ice of 0.8 to 1.0 cm s^{-1}. This is in good agreement with AMTV results. The AMTV friction speeds on day 219.9 calculated from the vertical water velocity spectra and shown in Fig. 2.14 were around 0.8 cm s^{-1} in the lead and 1.0 cm s^{-1} under the ice.

Contours of model density are shown in Fig. 3.2. The lead is in the upper left and the surface stress is to the left. The contour of zero horizontal density gradient is overlaid, roughly separating the domain into one region influenced by the lead surface and another by the ice surface. The horizontal density gradient is positive in the region under the ice, a situation conducive to the over-running overturns discussed previously. However, the 2-D steady model does not allow these overturns, since the advective terms have been neglected. Even in the quasi-steady period around day 219, it appears that there exists a potential for instability that cannot be simulated with the current model.

The model represents the boundary observed on day 220 reasonably well. Both the model and AMTV observations indicate fresh, warm water mixing vertically in the lead. However, the observations suggest the temperature, salinity, and heat and salt fluxes diminish significantly within a few hundred meters of the downstream lead edge, while the model values decay over much larger distances. One possible reason for the differences in horizontal dependence of both scalars and fluxes is that the advective terms are in reality significant, particularly near the lead edge, causing over-running overturns and enhanced mixing. However, unstable conditions were not directly indicated by the day 220 AMTV observations. That may be because the horizontal density gradients were too weak to play a significant role. The enhanced vertical mixing observed under the ice may also be because the model boundary condition (stress and roughness

length at 50 m intervals) could not adequately capture the effect of the lead edge on mechanical mixing. Lead edge mechanical forcing was suggested to be an important factor in the pattern of unstable lead convection by *Smith and Morison* [1998]. The 2-D unsteady model is required to investigate these two possibilities.

3.2.3 RESULTS AND DISCUSSION—DAY 209 TO DAY 215

While the one-dimensional model produced reasonable simulations for the boundary layer transition from lead to ice on day 220, we now investigate its ability to simulate the horizontally averaged boundary layer during the strong fresh water flushing period from day 207 to day 215. There is no lead in this simulation. The model domain is 30 m deep with a vertical grid spacing of 0.3 m. The time step is 15 minutes. Initial temperature and salinity profiles for the model are from the cast at ocean city on day 209.2. Initial velocity and eddy viscosity profiles are calculated using the steady solution for the initial boundary condition. The model is forced by surface stress from Fig.2.4a. Radiative flux through the ice is set to zero, and the ice-ocean heat flux is determined from the bulk formulation. Interfacial salt flux can arise from bottom melting that balances heat flux and from a specified percolation velocity while conductive heat flux through the ice is set to zero (Eq. 3.15). From day 210 to day 215, the percolation velocity is set to $1.6\text{x}10^{-6}$ m s^{-1}, corresponding to a salt flux of $4.6\text{x}10^{-5}$ kg s^{-1} m^{-2} upward. This is the flux calculated from the change in salt content of the upper 30 m. Before day 210, the percolation velocity is set to zero. The roughness length is set to 0.01 m. The bottom boundary conditions are the same as above.

Figure 3.3 shows both modeled and observed salinity and temperature contours and elevation above freezing temperature at 5 m. The results are dominated by the enormous freshwater flux beginning on day 210. The fresh water is not distributed as deeply in the model as in the observations: on day 215 the 30 psu contour is found at 11 m in the model and 17 m in the observations. The model output is adjusted to include the advective change in mixed layer

salinity from day 210 to day 215 so that the total salt content in both the model and the observed water column on day 215 are the same. The advective change is presumed uniform with depth and linear in time. The 30.5 psu contour is close to the observed, but the way in which fresh water is distributed above is quite different. The temperature contours show that relative to observations, the model ocean is colder at the surface and warmer at depth. Advective effects have not been used to correct the model temperature field, yet they probably are the reason for the variability in the extent of a warm core (–1.45 °C contour) during the period. The elevation of the mixed layer temperature above the freezing temperature drops steadily in the model. The model mixed layer became so fresh that the freezing temperature rose above the ambient temperature, implying the possibility of frazil ice formation. The supercooled mixed layer is visible from day 213 onwards in Fig. 3.3. The observed elevation above freezing temperature dropped from day 209 to day 212, then remained around 0.1 C° until day 215.

There are four possible reasons that the observed mixed layer was warmer (relative to the freezing temperature) than was the simulated mixed layer. First of all, the model neglects all oceanic heating due to solar radiation. Of course, solar heating through leads and melt ponds was occurring, and even with no leads, 2-5% of incoming shortwave radiation enters the ocean through bare ice [*Light et al.*, 2003]. Secondly, the SHEBA camp may have drifted into warmer water. It appears that the mixed layer and upper pycnocline were warming from day 212 to day 215 (Fig. 2.5), probably due to a combination of solar heating and advection. Third, the model did not mix the fresh water as deeply as the observations suggest, which means that warm water below the model pycnocline was not brought into the mixed layer and less thermal energy was available to maintain the elevation above freezing temperature. Underestimated vertical mixing plus the absence of the possibly advective warm core in the pycnocline hinder the model's performance. Fourth, the model does not take into account frazil ice production such as that observed with the ROV in the upper 2 m during the initial

flushing of the lead. Such a release of latent heat and salt would to result greater temperatures and salinities deeper in the boundary layer. Unfortunately we do not have a quantitative observation of this phenomenon.

Turbulence mast data from ocean city agree qualitatively but not in detail with one-dimensional model calculations. Figure 3.4 shows simulated friction speed and heat flux with ocean city TIC and AMTV observations. Salt fluxes from the TIC are not plotted since they are not reliable from 211-215. In Fig. 22, the TIC at 2.7 m very closely follows the one at 6.7 m (distance from interface) for both quantities, which is not generally true for the model. The model friction velocity at 6.7 m matches the observed for the most part. The model value of friction velocity at 2.7 m is nearly double the observed value on day 211, converging to it by day 213.5. The model compares more favorably to the AMTV values of friction velocity. The AMTV did not suffer from the same problems of biofouling as the TIC, nor is it vulnerable to possible biasing due to topographic features, as is the TIC. Biofouling and mechanical wear may have led to poor rotor performance, especially at 2.7 m.

The observed heat fluxes are much different than the model calculation for days 212-214, where the observed heat fluxes were upward while the model heat fluxes are close to zero. The large upward TIC fluxes occur at about the same time that the surface stress momentarily increased and the AMTV observed even larger upward heat fluxes. It is possible that the inexplicably large upward heat fluxes at 5 m (AMTV) in localized areas halted the decline in the elevation above freezing temperature in the mixed layer on the whole, thus allowing the ice-ocean heat flux from day 212 to day 214 to remain strong. The other factors discussed above related to the low model heat content of Fig. 3.3 could also apply here. Ultimately, the large AMTV fluxes probably originated from the water heated in leads. Of course, the simulation does not include solar heating or the horizontal variability required for this mechanism.

The TIC data before day 219 certainly do not seem to be what is expected of a one-dimensional process driven by surface buoyancy flux. To investigate the effect of the massive influx of fresh water on the boundary layer structure and interaction with the ice, a 1-D, time-varying numerical model was used. The model was unable to correctly simulate the observations prior to day 219. A two-dimensional unsteady version of a three-dimensional model is now used to investigate the problem of the stable, stratified, non-homogeneous, unsteady boundary layer. First, performance in simulating days 219-220 is investigated, then the more extreme case of days 209-215. Perhaps it can explain the observed deeper, saltier mixed layer and abnormally strong upward fluxes on days 212-214.

3.3 THREE-DIMENSIONAL MODEL

A three-dimensional model has been developed with an eye towards quantifying the stability of the horizontally inhomogeneous boundary layer under melting sea ice. It is a non-hydrostatic, time-dependent, with the assumption of an incompressible, Boussinesq fluid. As discussed above, CTD observations at SHEBA from July and August show warm, fresh surface water mixing more deeply than predicted by a one-dimensional mixed layer model forced by observed winds and meltwater input. Autonomous vehicle observations around a lead during the same period show fluxes suggestive of a warm fresh lead plume underneath cooler, saltier seawater. It has been postulated that boundary layer shear in the presence of a horizontal density gradient would give rise to such unstable conditions [*Crawford et al.*, 1999], increasing the vertical mixing beyond the one-dimensional prediction. It is the purpose of this section to explore this possibility. We also wish to explore the inherently two-dimensional, unsteady summer lead flushing process in its own right.

3.3.1 MODEL DESCRIPTION

The model, a discretization of Eqs. 20-24, is based on the model of *Smith et al.* [2002] with modifications for summertime ice-ocean boundary layer study. Previous two-dimensional incarnations of the model are found in *Smith and Morison* [1993, 1998]. In *Smith and Morison* [1993], the upper ocean response to brine rejection in leads and movement of the ice was investigated. The two-dimensional hydrostatic model successfully simulated leads with a range of buoyancy flux and ice velocity, confirming the lead number scaling of *Morison et al.* [1992]. *Smith and Morison* [1998] showed that freely convecting wintertime leads show only minor departures from the hydrostatic simulations. It was also shown that two- and three-dimensional simulations allow for salty plumes to sink to the halocline relatively intact when ice velocity is low, actually shoaling the mixed layer when a one-dimensional model would deepen it. Higher-dimensional simulations can also allow for mechanical forcing at lead edges, which triggers convective events in their model. The most recent version of the model [*Smith et al.*, 2002] is three-dimensional, non-hydrostatic with two options for parameterization of turbulent mixing. The generation of geostrophic eddies through dynamic instability around winter Arctic leads was examined. The model of *Smith et al.* [2002] forms the basis for the model described here.

The conservation equations are those of Eqs. 3.1-3.5. The model is solved in a reference frame fixed to the ice surface, and a free-stream velocity term in the y-momentum equation $(-fU_i)$ forces horizontal flow. Stress is written in terms of local gradients.

$$\boldsymbol{\tau} = K\nabla\mathbf{u} \tag{3.18}$$

As in the one-dimensional model the eddy viscosity is obtained as the product of friction speed and mixing length [*McPhee*, 1994]. Horizontally averaged surface values and vertical profiles of stress and buoyancy flux are used to specify the

eddy viscosity as a function of depth and time only. In the surface layer, friction speed is set to a constant (equal to the observed surface value) and mixing length increases linearly. Below the surface layer, friction velocity is determined locally from the shear (Eq. 3.10). The friction velocity is then horizontally averaged (being careful not to include the values in ice) and multiplied with mixing length to form eddy viscosity. Both horizontal and vertical momentum flux terms use the same viscosity, although they have differing background values. The diffusivity of temperature and salinity are equal to the eddy viscosity following an assumption of low gradient Richardson number.

The pressure equation is derived as described in *Smith and Morison* [1998]. By taking the divergence of the momentum equation and applying the continuity equation an elliptic equation for pressure is obtained.

$$\nabla^2 p' = \frac{\partial RHS_x}{\partial x} + \frac{\partial RHS_y}{\partial y} + \frac{\partial RHS_z}{\partial z} = \nabla \cdot \mathbf{RHS} \tag{3.19}$$

Here **RHS** is the right hand side of the vector momentum equation when only $\partial \mathbf{u} / \partial t$ and the pressure gradient terms are on the left hand side.

Centered differences in space and leapfrog in time conventions are used on a staggered grid. The rate of change of velocity is calculated without the pressure term, then new salinities (densities) and temperatures are calculated. Now pressure can be solved and used to revise the velocity calculation. Boundary conditions are applied, and the solution is averaged with the previous solution before advancing to the next time step.

Doubly periodic flow is specified at the vertical boundaries, and no flow is allowed through the top and bottom boundaries. The bottom boundary is a free slip boundary for horizontal velocity, and no flux for either temperature or salinity. The top boundary is a flat surface lead surrounded by sinusoidal ice topography. There is a no slip condition for horizontal velocity. To impose

realistic ice topography, temperature and velocity are held constant in the ice. Multiyear sea ice at SHEBA was isothermal at the freezing point during the summer [*Perovich et al.*, 2003]. The salinity flux is zero at the ice-ocean interface—no ice melting or forming. In the lead a radiative heat flux is distributed with an extinction depth of 4 m. The lead salt flux is also specified, and it enters in the top grid cell only.

The 40-m wavelength of the ice topography is chosen from an estimate of the peak in the spectrum of ice draft gathered from the AMTV. The 2-m maximum thickness corresponds to a mean ice draft of about 1 meter, and typical ridges with 2 or 3 m of draft, as indicated by the AMTV data. The ice topography is greatly simplified by using only one sinusoidal component.

Initial conditions are either a steady state boundary layer solution for the given free stream velocity (assuming neutral stratification and a flat upper surface) or uniform velocity relative to the motionless upper surface. Temperature and salinity are initially uniform at 0 ^{o}C and 31 psu.

3.3.2 RESULTS AND DISCUSSION—DAY 220

The two most significant three-dimensional model experiments are discussed: strong fresh water flushing during boundary layer spin up (around day 207) and freshening of a quasi-steady boundary layer (day 219.9). Model parameters are summarized in Table 1. Note that the y-dimension is much smaller than the other dimensions, essentially eliminating the y-derivatives. Therefore, from this point forward, we refer to this as the 2-D unsteady model.

Figure 3.5 presents the quasi-steady result 4 hours into the simulation of day 219.9 (in which time the deep water traveled about 1500 m). Ice topography is outlined. Salinity (color shading) shows that the fresh water entering in the top grid cell is mixed downward, while at the same time it is carried downstream. As expected, the salinity is lowest at the surface at the downstream edge of the lead.

Table 1. Parameters for two three-dimensional numerical simulations. Spin up refers to a period such as before day 210 of the SHEBA experiment, 1998, when the fresh layer in the lead was shrinking. Quasi-steady refers to a period such as around day 219, 1998, when there was no fresh water layer in the SHEBA lead.

Model Parameters	**Spin Up**	**Quasi-steady**
Lead Width (m)	80	480
Domain Size (x, y, z m)	(240, 4.5, 10)	(1440, 9, 22.5)
U_i (m s^{-1})	0.07	0.15
Lead Salt Flux (10^{-5} kg m^{-2} s^{-1})	4.8	2.0
Lead Heat Flux (W m^{-2})	200	448
dx, dy (m)	0.5	1.0
dz (m)	0.1	0.25
dt (s)	0.5	0.5
Background A_z (m^2 s^{-1})	$1x10^{-5}$	$1x10^{-6}$
Background $A_{x,y}$ (m^2 s^{-1})	$1x10^{-3}$	$1x10^{-5}$

Temperature (white contours) follows a similar pattern, with the warmest water at the surface at the downstream edge of the lead. Isotherms are sloped differently than isohalines since the temperature source is distributed exponentially with depth, while only the water at the surface is freshened. Velocity (u and w vectors) shows a vertical shear on average, although the topography modifies the flow to satisfy the continuity equation. The simulation is not strictly steady because as long as the lead fluxes are present, the boundary layer will become fresher and warmer, eventually building a strong, shallow pycnocline. However, it is approximately steady in the sense that the wind and fresh water input did not change significantly over several hours (also assumed in the one-dimensional model).

Horizontal transects of model temperature, salinity, friction speed, heat and salt flux (Fig. 3.6) compare very well to AMTV observations from day 219.9 (Figs. 2.12-2.14). Temperature at 5 m in the lead shows a nearly identical

horizontal gradient to the AMTV data from day 220: a rise of 0.01 K per 100 m. Temperature decreases on a slightly steeper slope downstream of the lead edge in both the model and observations. Model salinity in the lead shows the freshening rate with downstream distance is weaker than observed, although absolute salinity from the AMTV is biased by a decreasing trend, as discussed previously. Friction speed at 5 m increases from lead to ice: 0.007 m s^{-1} to 0.009 m s^{-1} in the model, consistent with the AMTV observations. Heat flux at 5 m reaches about 130 W m^{-2} downward in the last 200 m of the lead, comparable to the AMTV lead averages for that run (98 W m^{-2} and 144 W m^{-2}). Model heat flux at 5 m becomes upwards (nearly 100 W m^{-2}) immediately downstream of the lead edge and decays to about half that value over the next 400 m. The covariance estimates of heat flux for all of segments 3 and 4 do not pass the significance test, although when using 100 m segments, two of the four pass (40 W $m^{-2}$and 97 W m^{-2}). The AMTV under-ice heat flux average is similar to a model transect between 5 m and 10 m. It should be noted that the AMTV did not travel beyond about 300 m downstream of the lead, making this downstream comparison with the model difficult. Model salt flux at 5 m approaches 1.2×10^{-5} kg m^{-2} s^{-1}, which is close to the AMTV lead values of 1.7×10^{-5} kg m^{-2} s^{-1} and 2.4×10^{-5} kg m^{-2} s^{-1}. The model salt flux decays by more than 50% in 100 m downstream. AMTV observations also suggested weaker salt fluxes under the ice.

The two-dimensional unsteady model transects share many features with the two-dimensional steady model results, with some important differences. In better agreement with the AMTV observations, the water properties return to background values much more quickly downstream of the lead in the 2-D unsteady model than in the 2-D steady model. The 2-D unsteady model heat flux at 5 m becomes upward immediately downstream, rather than after 2 km as in the 2-D steady model, giving rise to much larger heat flux divergence between 5 m and 10 m. The constant temperature boundary condition under the ice results in more oceanic heat loss (by eddy diffusion) than the bulk heat flux condition used

in the 2-D steady model. The 2-D unsteady model lost thermal energy at an average rate of 80 W m^{-2} to the ice during the run shown, while the 2-D steady model was around 50 W m^{-2}. The melt rate implied by the unsteady model heat flux is 2.6 cm day^{-1} (a salt flux about 20% of that in the lead). Observations of ablation rate at the SHEBA lead edge support the 2-D unsteady model heat flux results. On day 218 five ice thickness gauges from 6 m to 51 m from the lead edge (adjacent to our hut and downstream of the lead) measured an average melt rate of 3.8 cm day^{-1}, while the SHEBA camp average was about 1.3 cm day^{-1} [*Perovich et al.*, 1999].

AMTV heat flux observations show mixed comparisons with the two models, but seem to support the 2-D unsteady model. Under the ice the AMTV did not observe strong upward (2-D unsteady) or downward (2-D steady) flux, rather a weak downward heat flux. However, as noted, the unsteady model result between 5 m and 10 m is similar to the 5 m AMTV observations. The role of the molecular sublayer in the observed boundary layer may be important in affecting depth distribution of fluxes [*McPhee*, 1992] and should be examined with further study. Finally, salt flux at 5 m decreases downstream of the lead in the 2-D unsteady model, but increases in the 2-D steady model. AMTV observations tend to support the unsteady model, since it did not measure large salt fluxes for much of the under-ice transect.

In general, the two-dimensional unsteady model agrees closely with observations from day 220, despite less realistic ice boundary conditions than the two-dimensional steady model. Topography and advective terms that are not possible in the steady model result in more rapid vertical mixing. Near the start of the run, for example, when the fresh water is first introduced, weak, unstable density gradients are found under the ice. This spin-up effect will be examined in the next section. The mechanical forcing associated with an explicit lead edge also causes enhanced mixing. Disagreements between the AMTV results and the 2-D unsteady model might be resolved by allowing ice melt in the model.

3.3.3 RESULTS AND DISCUSSION—DAY 209

Compared to the quasi-steady experiment, the spin-up problem is characterized by larger fresh water flux, smaller ice velocity, and no initial velocity shear. See Table 1 for a complete specification of the run discussed here. The salt flux in the model lead is set approximately to the flux estimated from the rate of decay of the fresh layer in the lead as observed by the ROV early in the storm (day 206.5 to day 210.5).

Figure 3.7 shows the simulation after one hour. (Beyond one hour the model solution became numerically unstable.) The ice topography is outlined and is of the same dimension as the quasi-steady run. At this time, the lead was 100 m wide. Salinity (shaded) shows the presence of a layer just over 1 m thick in the lead. As the layer is flushed past the ice ridges, an unstable density gradient develops. The fresh plume mixes downward as it is swept downstream, but dense, salty water remains in the ice depressions above. Temperature (white contours) shows the warmest water is at the lead surface near the downstream edge as expected. Under the ice the fresh water plume has a maximum temperature in its core a few meters below the ridges. Velocity (blue arrows) indicates strong shear in the top 5 m, particularly below the ridge keels.

Buoyancy frequency (Eq. 2.10) indicates regions of low stability under the ice (Fig. 3.8). The model criterion for mixed layer depth (used in the determination of mixing length) is a buoyancy frequency of 1.5×10^{-5} s^{-2} and is contoured in black. The -1×10^{-7} s^{-2} contour is in white. The regions of unstable density gradient are visible in the ice cavities just downstream of the lead inside the white contour. Indeed, "overrunning" of dense water over light water is simulated. However, overturning is not observed in the simulated velocity field. A turbulent Rayleigh number can be used to investigate the likelihood of buoyant instability in the model given an unstable salinity gradient, after *Smith and Morison* [1998].

$$Ra = \frac{g\alpha \frac{\partial S}{\partial z} h^4}{A_S A_z} \tag{3.20}$$

Although the criterion for instability is intended for quantifying the relative influences of molecular diffusion and turbulent heat transfer between two horizontal plates maintained at steady temperatures, it can provide insight into the current problem. In the turbulent heat transfer problem, when *Ra* is larger than about 10^3, buoyant overturning convection is expected to take place rather than "diffusive" transfer. In this numerical model, the analog to molecular diffusion is turbulent diffusion used to parameterize unresolved eddies, and convective instabilities correspond to resolved overturns. The eddy diffusivity and viscosity are used rather than the traditional molecular values, and they are assumed equal. Here h is the distance over which the salinity gradient is found. Substituting values from the simulation in Fig. 3.7 ($\partial S/\partial z$ = 6x10^{-3} psu m^{-1}, h=1 m $A_S = A_z$ = 5x10^{-4} m^2 s^{-1}) results in a value of 200, which is nearly large enough for instability. If the gradient were larger and/or the depth over which it occurred were larger, a resolved instability could occur. For example, if h=2 m, *Ra*= 3000. If the model could be run for a longer time, it is possible the salinity gradient could increase to a critical value at which point we could expect the model to show overturning. The model domain would have to be extended sufficiently for the plume to descend to the critical value before the next lead was reached. From Fig. 3.7, the plume appears to descend at a rate of about 1 m per 80 m. In addition, if the eddy viscosities were lower by a factor of two, overturns would be expected in the model.

Although the model simulation in Fig. 3.7 only lasted one hour, it is worthwhile to compare the snapshot in time with observations and 1-D (no lead) simulations from days 207-215 at SHEBA. Thermal energy is found at greater depths in the 2-D unsteady model. The salt and heat content in each horizontal layer of the 2-D unsteady model are compared with an equivalent 1-D simulation

in Fig. 3.9. The 1-D model is run with the 2-D model's horizontally averaged salt flux (1.6×10^{-5} kg m^{-2} s^{-1}), heat flux (67 W m^{-2}), and surface friction speed (0.005 m s^{-1}). An extinction depth of 4 m is used to distribute the heat flux. The run is repeated with a freezing point surface boundary condition replacing the zero-heat flux condition. The temperature and salinity profiles from these two runs are averaged so that the integrated heat content agrees with the 2-D model. Specifically, the profiles from the constant surface temperature run are weighted twice as heavily as the zero heat flux run since the 2-D model has twice as much ice boundary as lead boundary. The difference in heat content between the 2-D model and the net input due to radiation can be used to calculate the average heat flux to the ice in the 2-D model: 7 W m^{-2}. The 2-D model does not allow this heat flux to melt ice and cause a salt flux. This would affect the solution only slightly since the implied melt rate is small compared to the specified salt flux in the lead. To make a fair comparison, melting was not allowed in the 1-D simulations here—the salt inventory is in agreement as well.

The vertical distributions of thermal energy and salt differ. Maximum heat content is found at 4 m in the 2-D model, but at 1.5 m in the 1-D average. Reduced salinity water is found as deep as 5 m in the 2-D model, compared to 4 m in the 1-D model. The heat and salt distributions in the 2-D case reflect deeper mixing of the surface water. The depths influenced by the lead are still quite shallow compared to observations, although a longer run could possibly allow the warm, fresh water to mix more deeply. For example, the 1-D result from Fig. 3.3 shows the fresh water introduced on day 210 (traced by the 31 psu contour) finds its way to 11 m by day 211, and in the 1-D model in this section it only reaches 4 m. Perhaps the 2-D model would show a similar or deeper fresh water signal if it could be run over several days. The 2-D spin up simulation also suggests a longer run would result in a more vertically uniform water column (compared to 1-D simulation in Fig. 3.3), particularly if the regions of unstable density gradient began to overturn. Although neither the 1-D nor the 2-D unsteady model seems

to predict the relatively deep observed mixed layer, the 2-D unsteady model suggests that horizontal variability in heat and salt flux, combined with ice topography may contribute to enhanced vertical mixing.

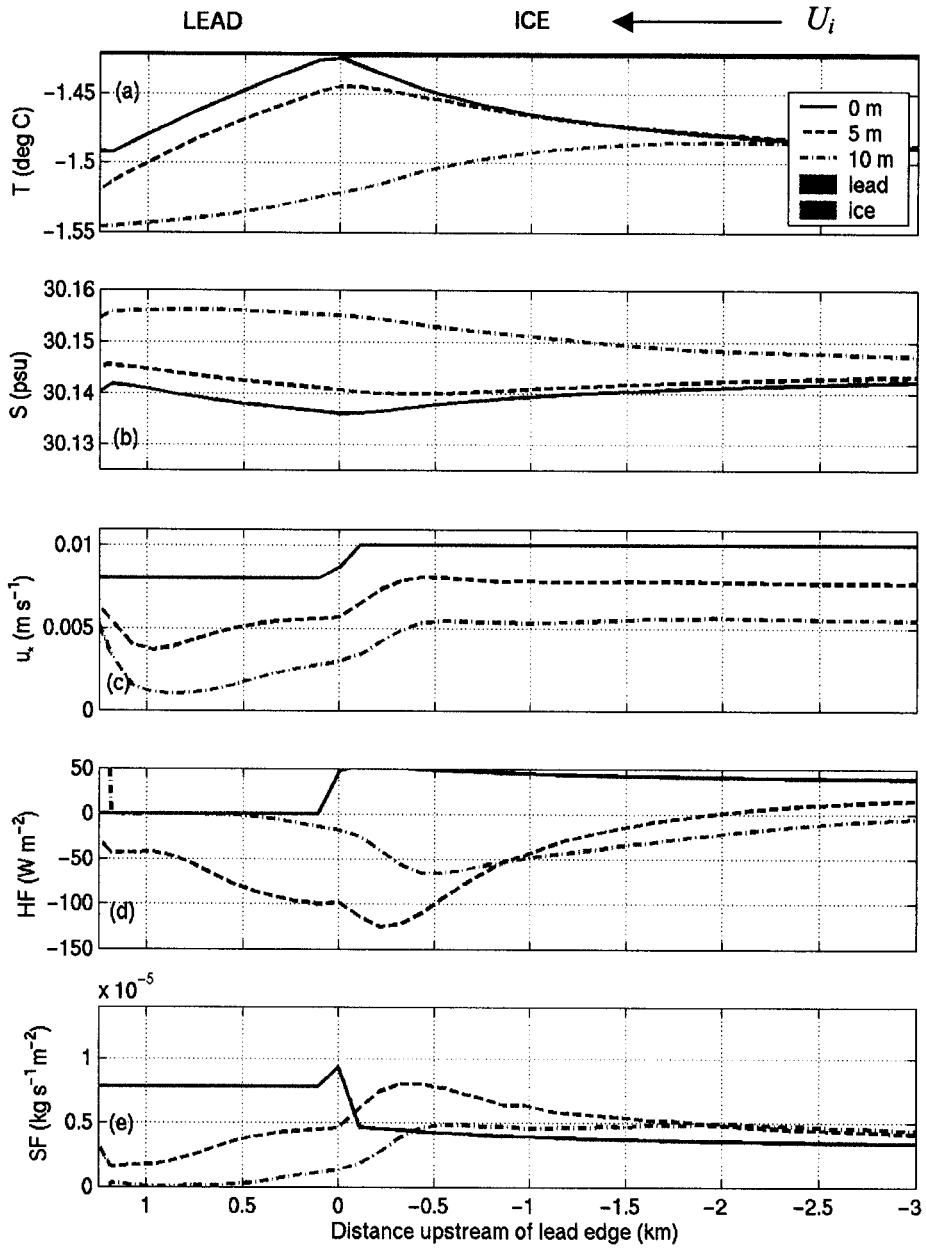

Figure 3.1. Two-dimensional steady simulation of SHEBA lead on day 220, 1998. Horizontal transects at surface, 5 m, and 10 m. The lead is in the upper left and the ice is moving from right to left.

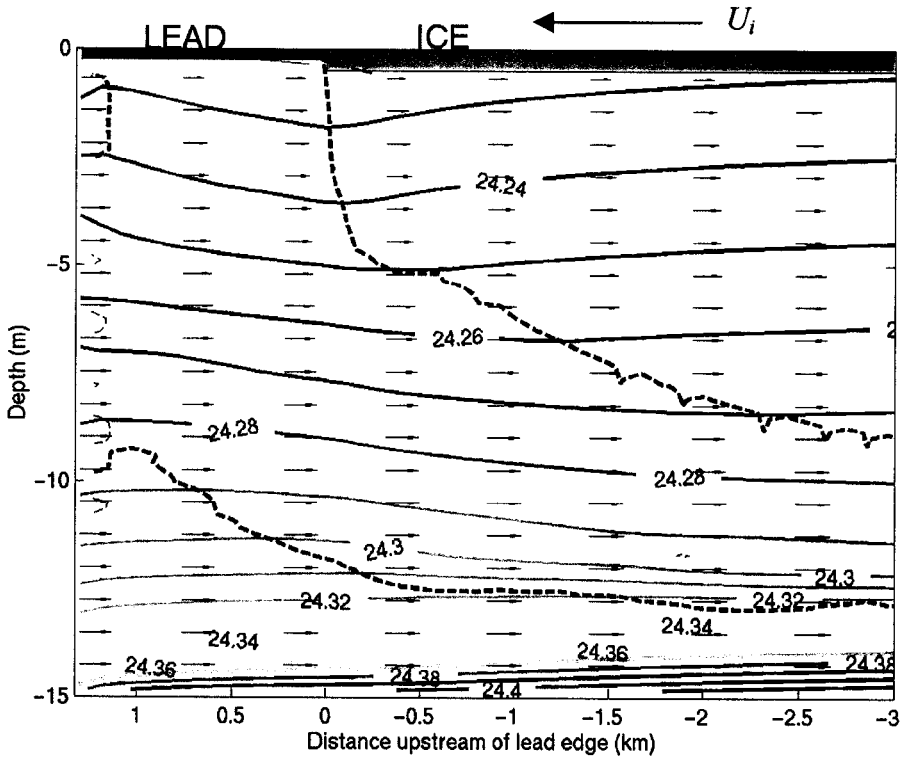

Figure 3.2. Density contour for same run as Fig. 3.1. Units are density minus 1000 kg m^{-3}. Black line indicates where horizontal density gradient changes sign. Velocity field is also shown (sub-sampled).

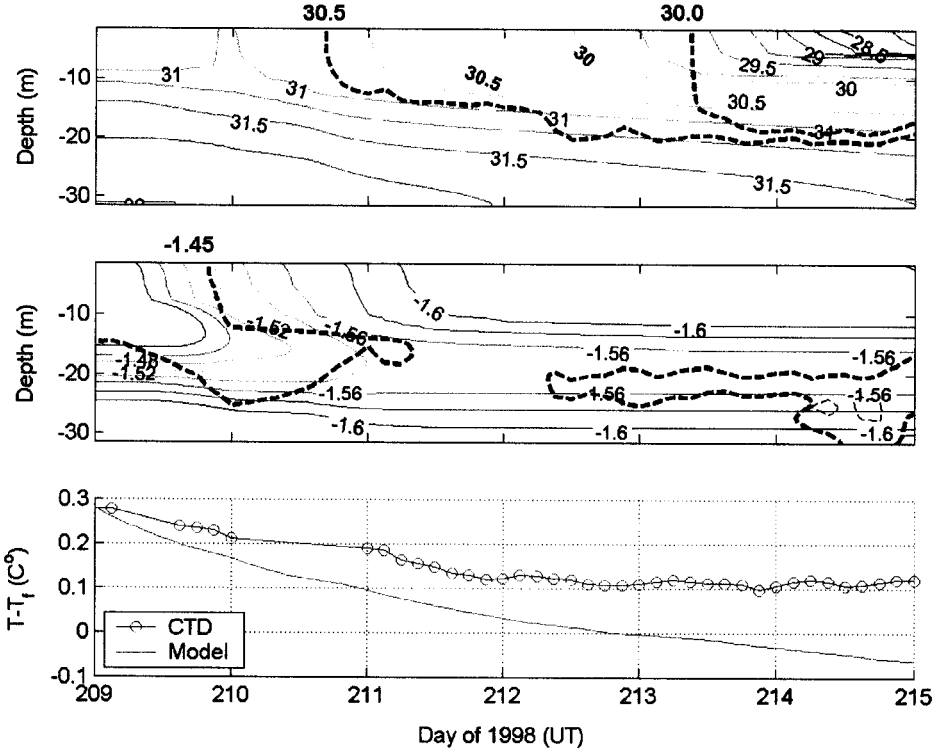

Figure 3.3. One-dimensional run for days 209-215, 1998. No leads or solar radiation are present. Fresh water surface flux of 4.6×10^{-5} kg m^{-2} s^{-1} begins on day 210. Salinity and temperature fields, and elevation above freezing at 5 m depth are shown. A uniform freshening rate of 0.4 psu over days 210-215 has been applied to the model salinity to account for observed advective changes. Observed contours are shown with dashed lines and bold numbers (from Fig. 2.5).

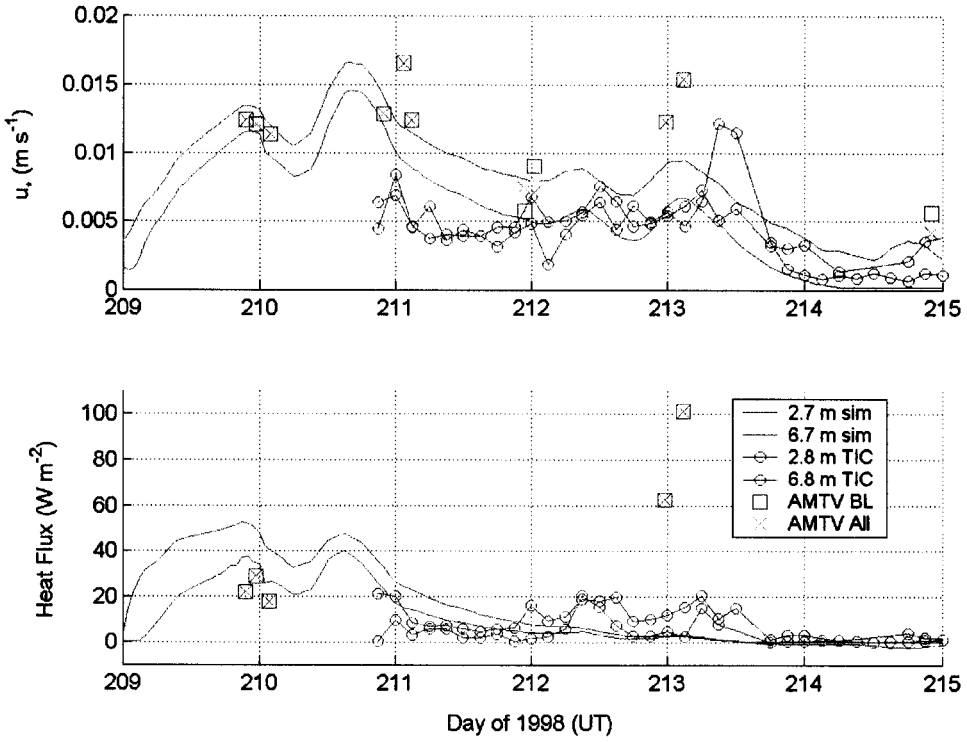

Figure 3.4. Friction speed and heat flux at two depths for the same run as Fig 3.3 compared with TIC observations at 2.7 m and 6.7 m below the ice-ocean interface and AMTV observations.

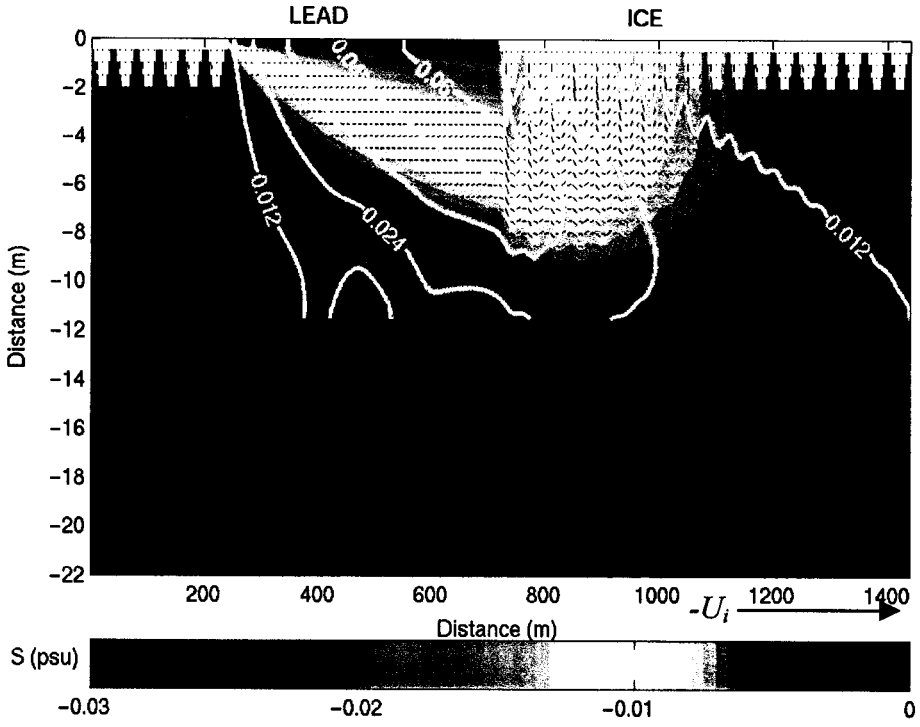

Figure 3.5. Simulation after 4 hours of day 219.9 with a nonhydrostatic, three-dimensional model in 2-D unsteady mode. Salinity deviation is shaded, and temperature deviation is contoured. Velocity field is also shown; the velocity at the bottom is 0.15 m s^{-1}. Only every 10^{th} velocity vector in the horizontal is shown. Ice topography (in white) is at a fixed temperature and position, and there is zero salt flux at the interface. Heat and salt fluxes at the lead surface are 448 Wm^{-2} and $2x10^{-5}$ kg m^{-2} s^{-1}.

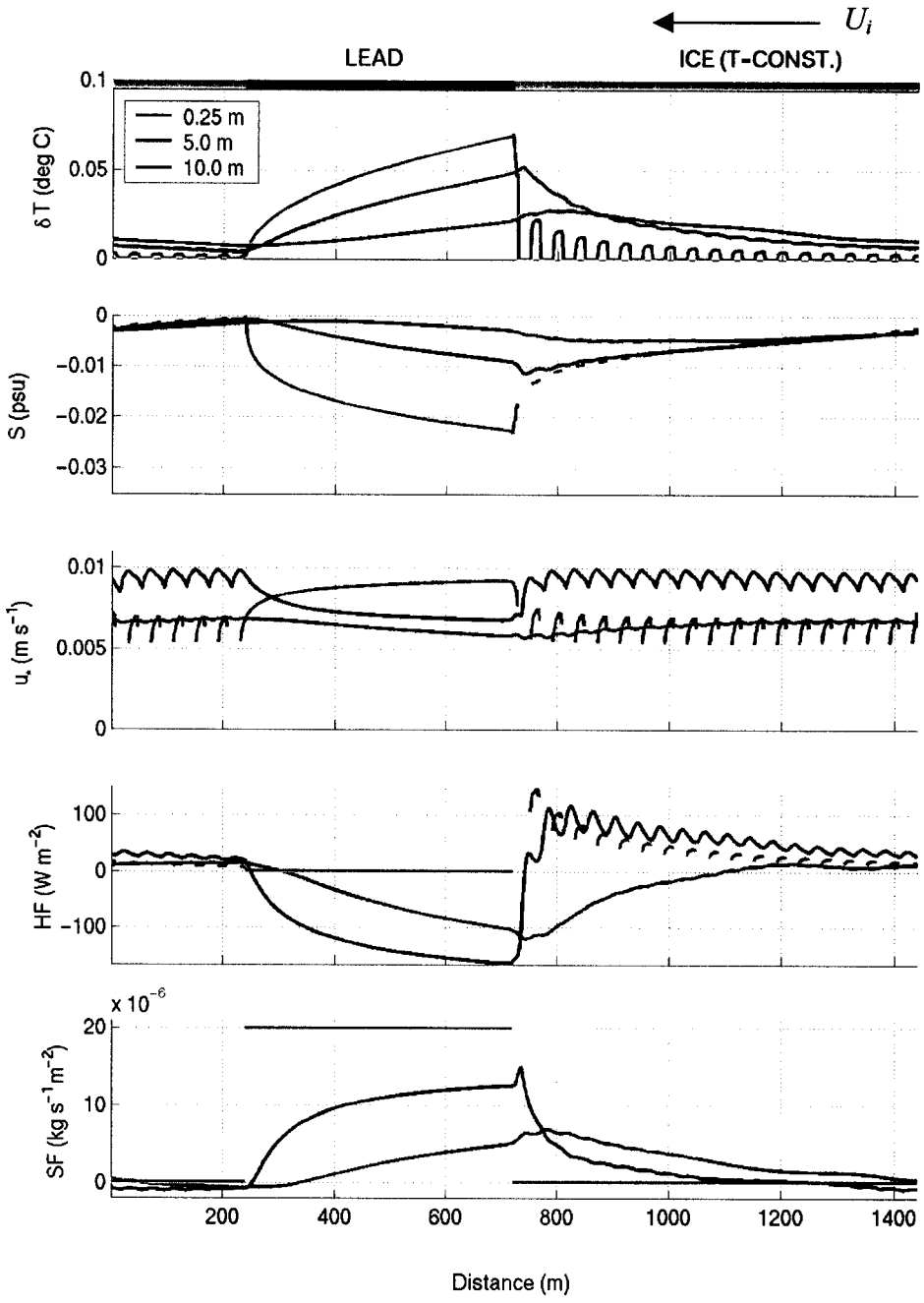

Figure 3.6. Horizontal transects at surface, 5 m, and 10 m for same model run as Fig. 3.5. Lead is the 480 m segment beginning at 240 m.

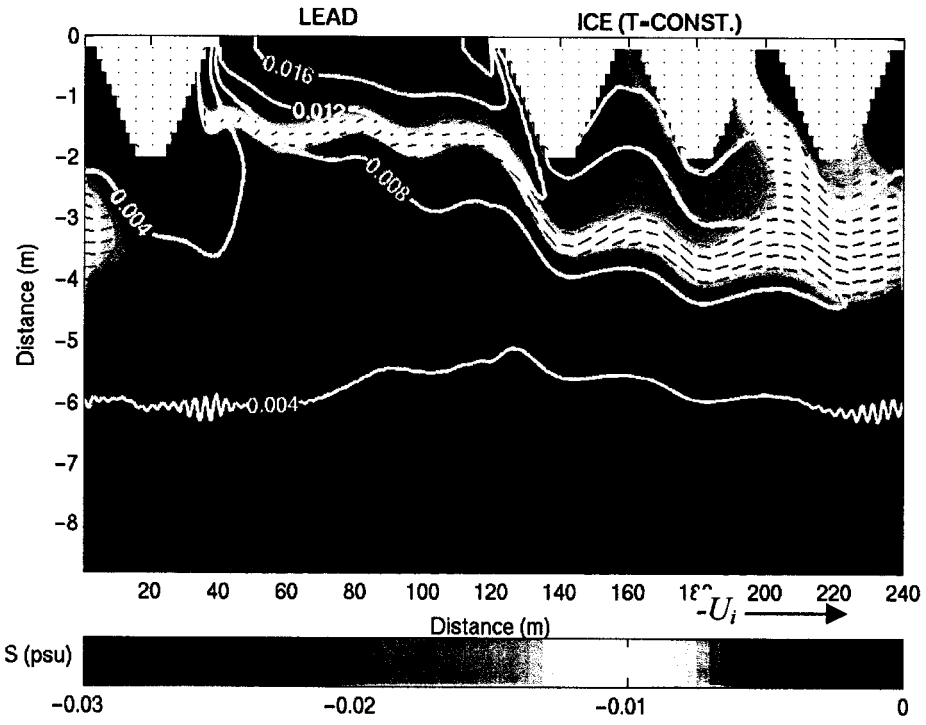

Figure 3.7. Simulation of day 209 after one hour with nonhydrostatic, three-dimensional model in two-dimensional mode. Salinity deviation is shaded, temperature deviation is contoured. Velocity field is also shown, only one of every 10 vectors in the horizontal is shown. Flow is from left to right.

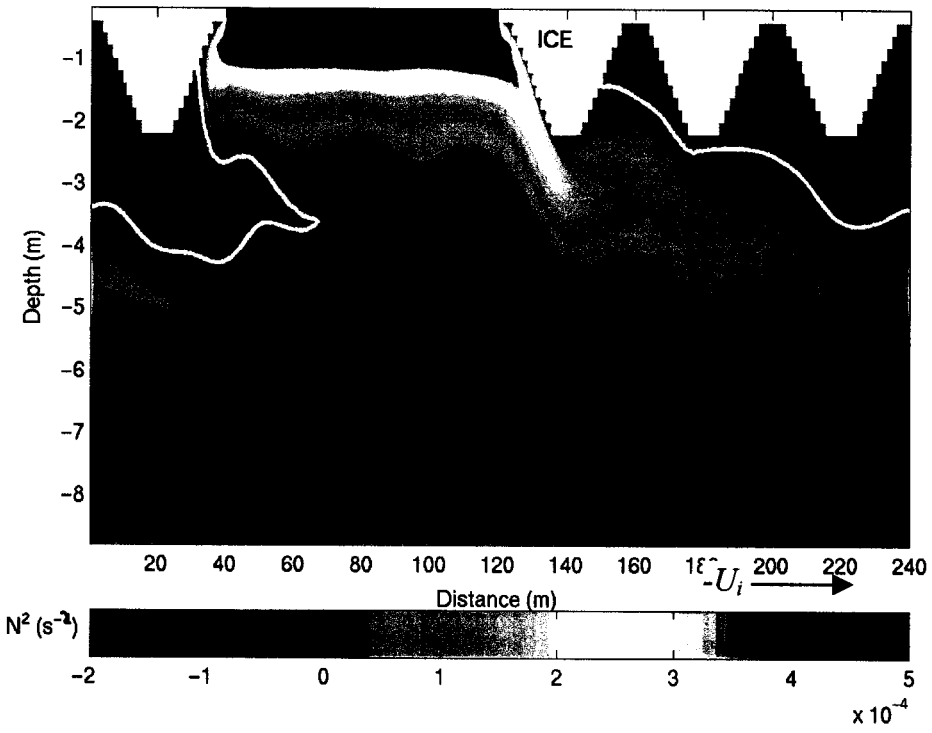

Figure 3.8. As in Fig. 3.7, but the square of buoyancy frequency is shaded. The black line is the 1.5×10^{-5} s^{-2} contour (the model mixed layer is defined by the average depth of this contour). The -1×10^{-7} s^{-2} contour is in white and separates positive and negative stability regions.

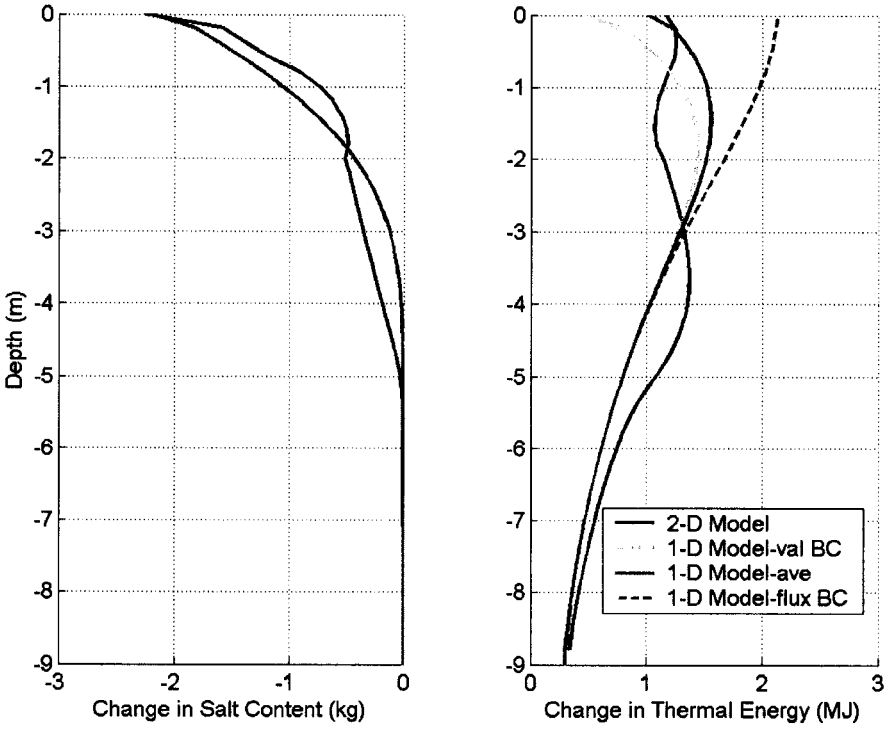

Figure 3.9. The salt content and thermal energy in each horizontal layer after 1 hour from the 2-D model (blue) and the 1-D model (red). Each layer is 0.2 m thick. Two-dimensional results are from day 209 run in Fig. 3.7. The one-dimensional model is run with the horizontal average interfacial salt flux (1.6×10^{-5} kg m^{-2} s^{-1}), heat flux (67 W m^{-2}), and surface friction speed (0.005 m s^{-1}). The run is repeated with a freezing-temperature surface boundary condition replacing the zero-heat flux condition. The solid line is the weighted average of the two (see text), equal in heat content to the blue line.

4. CONCLUSIONS

This section discusses the possible ways in which this work might scale up to large-scale ice-ocean processes and numerical models. Our observations provide valuable insight on the seasonal evolution of the ice-ocean system. We find the snow and ice melt does not enter the ocean immediately as it forms nor does it uniformly cover the surface. Rather, meltwater is retained near the surface (which lowers the albedo). The water drains into leads where it can build up in a strongly stratified layer if ice speeds are low. The release of fresh water from leads can occur in a sudden, massive "flush" challenging notions of horizontal homogeneity in the boundary layer. A simple heat balance calculation below also suggests that horizontal homogeneity of ice-ocean heat flux is tenuous during periods of large lead fraction and floe perimeter. Large-scale models could use a lead number approach and keep track of lead fraction and floe perimeter to delay the input of fresh water appropriately. These parameters may also help in correcting the ice-ocean heat flux for horizontal variability scenarios.

4.1 THE FATE OF THERMAL ENERGY IN THE UPPER OCEAN

To put our observations in perspective it is useful to compute an energy budget for the upper ocean at SHEBA. *Maykut and McPhee* [1995] showed that solar heating of the ocean in the Beaufort Sea area accounted for a large portion of ice melt during AIDJEX in 1975. The calculation described in this section for SHEBA also shows that solar energy input to the upper ocean is nearly balanced by loss to the ice and ocean warming. However, it appears that the standard estimate of loss to the ice (Eq. 2.8) is not as effective in countering the solar heat input as suggested by the relatively small observed ocean warming through the summer. A cartoon (Fig. 4.1) shows the energy exchange in and out of the upper ocean reservoir that could result in a change in temperature: solar energy into the reservoir via three different pathways, sensible heat transfer to the ice (causing melting, conduction and/or change in ice temperature), lateral oceanic advection

of thermal energy, and sensible heat transfer at the reservoir base in the pycnocline. Here we assume the ice is isothermal at 0 °C and that the heat flux through the pycnocline is negligible. Our results are consistent with these assumptions.

The fractions of area covered by ice, melt ponds, and leads changed significantly three times during June, July, and August, so the time series from *Perovich* [2002b] is approximated by the values in Table 2. Also shown is the mean downwelling shortwave and longwave radiation for each period from the SHEBA Project Office.

Table 2. Area fraction of bare ice, melt ponds, and leads and mean downwelling shortwave and longwave radiation during the summer at SHEBA.

Time		Ice	Pond	Lead	I_0	$LW_\downarrow$
(1998 Day)	(Date)	f_{bi}	f_{mp}	f_{ld}	(W m^{-2})	(W m^{-2})
152-166	1 June – 15 June	0.97	0.00	0.03	276	277
167-206	16 June – 25 July	0.75	0.20	0.05	234	295
207-227	26 July – 15 Aug	0.60	0.20	0.20	137	299
228-242	16 Aug – 30 Aug	0.78	0.02	0.20	88	294

The albedo of leads, α_{ld}, is 0.066±0.007 on cloudy days [*Pegau and Paulson*, 2001]. The effect of wind waves on the lead albedo is pronounced at large zenith angles (during spring) in sunny conditions, but during June, July, and August the sky is typically overcast.

The transmittances of bare ice and melt ponds as a function of wavelength were measured and reported by *Light et al.* [2003]. Before June 30 the bare ice was not strictly speaking bare. It had at least some measure of snow cover. No transmittance data is available for this transitional, snow-covered ice condition, and here we assume it is equal to the transmittance of bare ice. This is likely an over estimate, but the net effect is small.

Since the incident radiation was measured with a broadband detector, a spectrally-averaged transmittance for each type is formed:

$$\overline{T} = \frac{\int T_\lambda I_{0\lambda} d\lambda}{\int I_{0\lambda} d\lambda} \tag{4.1}$$

The integrals are over the wavelength range of strong solar radiation, roughly 350 nm to 2500 nm. Since the spectral intensity was not measured, the $I_{0\lambda}$ function was taken from *Grenfell and Perovich* [1984]. An average of clear and cloudy spectral intensities was used. Transmittance, T_λ, was measured on several days and at a few sites during July and August, and an average over the sites was used for each surface type. Cases where a layer of snow (on ice) or skim ice (on melt ponds) was on the surface were not used. While this dramatically affects the transmittances, both were relatively rare from late June to mid-August. Minimum and maximum transmittances over all sites were used to calculate lower and upper bounds on the solar radiation input to the ocean and will be discussed later. Spectrally averaged transmittances were 0.15 and 0.03 for melt ponds and bare ice, respectively, with minimum values of 0.11 and 0.02 and maximum values of 0.32 and 0.05.

The net longwave flux is estimated from Eq. 4.2 [*Ruffieux et al.*, 1995].

$$LW_{net} = \varepsilon(LW_{\downarrow} - \sigma T_0^{\,4}) \tag{4.2}$$

Longwave radiation can only leave or enter the ocean through open water, as the ice is an excellent absorber of infrared radiation. The emissivity, ε, is near one because of the very low lead albedo. We use a value of 0.95. The Stefan-Boltzmann constant, σ, is 5.67×10^{-8} W K^{-4} m^{-2}. The surface temperature of the lead is T_0, expressed in degrees Kelvin. We use the temperature in the lead layer

observed by *Paulson and Pegau* [2001] on day 203 (1.6 °C, a near maximum). The longwave emission from leads is then estimated to be 307 W m^{-2}.

The area fraction of the surface types and the fraction of incident radiation that passes through each allow an estimate of the solar energy flux that reached the ocean.

$$I_z = \{f_{bi}\overline{T}_{bi} + f_{mp}\overline{T}_{mp} + f_{ld}(1-\alpha_{ld})\}I_0 + f_{ld}LW_{net} \tag{4.3}$$

$$Q_{net}(t) = \int_{t_0}^{t} I_z dt' \tag{4.4}$$

The amount of energy absorbed at the end of each time interval (Q_{net}) is shown in Fig. 4.2. By the end of August, the ocean absorbed 160 MJ m^{-2}, roughly 60% from leads, 20% from melt ponds, and 20% from bare ice. Therefore, it is not appropriate to neglect the radiation transmitted through melt ponds and ice, at least during the SHEBA summer. The rate of solar heating of the ocean began to level off as the intensity of light diminished and as melt ponds froze over (mid-August). Neglecting the net longwave flux would result in a 5 MJ m^{-2} increase by day 227 and 9 MJ m^{-2} by day 242.

The net radiative flux calculation is necessarily crude because of a number of factors. First, the transmittance is a difficult measurement to make, especially under melt ponds where edge effects are difficult to quantify [*Light*, personal communication]. Secondly, there are relatively few transmittance measurements. Certainly transmittance depends on a number of parameters that must be neglected for lack of data, among the most important are ice thickness and the type of surface. Thin snow layers or skim ice are very important, and even with more data, the detailed distribution in time and space of such surface coverage is very difficult to observe. Other sources of error include the slight mismatch in the wavelength range of the shortwave detector and transmittance data (285-2800 nm

vs. 350-2500 nm). However, since the intensity of radiation is weak below 350 nm and above 2500 nm, the error in multiplying I_0 by mean transmittance should be small. Also, other shortwave radiation measurements at SHEBA were collected and showed slight differences with the Project Office instrument. Biases of up to 5 W m^{-2} were observed [*Persson et al.*, 2002], which would correspond to almost 40 MJ m^{-2} over June, July, and August. *Persson et al.* [2002] report that the Project Office instrument was biased low relative to other instruments, so we can regard our data as a lower bound on observed shortwave radiation.

Net solar input is nearly balanced by basal ice melt (neglecting conduction and ice warming—both zero for isothermal ice held at the freezing temperature). The heat flux through the ice-ocean interface is estimated by Eq. 2.8, shown for part of the summer in Fig. 2.4. The net loss of energy through the interface during June, July, and August is calculated by integrating Eq. 2.8.

$$Q_{ice}(t) = \int_{t_0}^{t} \rho C_p c_H u_{*0} \delta T \, dt' \tag{4.5}$$

The temperature elevation above freezing is taken from the 5-m temperature and salinity observed with the ocean city CTD, which was far from the nearest lead (nearly 1 km). The friction velocity is calculated from wind and ice velocities using Eqs. 2.5-2.6. In Fig. 4.3, the energy lost to the ice is plotted along with solar input to the ocean (and its upper and lower bounds due to maximum and minimum transmittances). By the end of August, the ocean lost 130 MJ m^{-2} to the ice. The thermal energy lost to the ice estimated from average bottom ablation around SHEBA (green circles) is taken from *Perovich et al.* [2003] (their Fig. 15b). They indicate less energy to melting early in the summer, and more energy to melting later in the summer compared to the bulk heat flux estimate. Overall, however, both results suggest ice melting was almost exclusively carried out by

locally heated surface waters, similar to the AIDJEX result of *Maykut and McPhee* [1995].

In the simplest balance, energy gained by the ocean but not lost to the ice would raise the ocean temperature. The ocean would have to increase in thermal energy by 30 MJ m^{-2} by the end of August (cyan curve in Fig. 4.3), or about 10 MJ m^{-2} using the lower bound of solar input (dashed cyan curve). The temperature of the ocean at four levels is plotted in Fig. 4.4 and does show a general warming near the surface for much of the summer. The thermal energy depends on the elevation above freezing (the upper set of curves in Fig. 4.4), which is nearly identical in shape to absolute temperature. The peaks in temperature early in the summer around 30–50 m seem to be unrelated to surface processes and are ignored here (perhaps a boundary current around Chukchi Cap). The temperature signal is very large and not evident at 5 m or 10 m. Conditions seem to return to normal on day 170. Then the temperatures above 30 m gradually climb away from the freezing temperature until day 210. The strong winds after day 210 rapidly lowered temperatures before an interesting spike at all depths around day 217, when the camp drifted off Chukchi Cap. Later, the temperatures at 5 m and 10 m returned to near-freezing, while the 30 m temperature remained significantly above freezing.

The change in thermal energy in the water column above each depth is calculated and plotted in Fig. 4.5. If one considers the ocean to only exchange energy at the upper surface, the curves in panel (a) are valid. The change in energy since June 1 ($t = 0$) in the water column above a depth, z, is given by

$$Q_{oc}(t,z) = \int_{-z}^{0} \rho C_p [\delta T(t,z') - \delta T(0,z')] dz' \tag{4.6}$$

If one assumes an advective heat flux into the upper ocean from adjacent regions can be represented by the change in heat content of the base of the mixed layer,

then this can be subtracted to obtain the change in internal energy due to surface processes alone.

$$Q_{oc-adv}(t,z) = Q_{oc}(t,z) - \rho C_p |z|[\delta T(t,-H) - \delta T(0,-H)] \quad (4.7)$$

The depth, H, must be below the level of influence of the surface, but small enough so that changes there are correlated to changes near the surface. We assume in Fig. 4.5b that the change in temperature at 30 m would have happened throughout the water column in the absence of surface processes. The advection correction does not make any difference between day 170 and day 210, as expected from the flat line temperature at 50 m in Fig. 4.4. After day 210, the energy in the upper layers fall in both formulations. Without correcting for advection, the thermal energy then increases above all depths (especially in the upper 30 and 50 m) from day 211 to day 220. Subtracting out the estimate of the advective change implies the water column is lower in thermal energy, i.e., the near-surface layers stayed the same temperature while the temperature rose at 50 m. Presumably, the warmer water advected in was cooled by the ice, especially in the top 10 m.

It is clear from Fig. 4.4 that some features observed at 50 m, and even 30 m are not reflected at 5 or 10 m. The most obvious is from day 152-170, but there are other smaller events that make the advection correction unreliable and noisy (day 215, day 221, and 227). The assumption of homogeneous vertical change in the absence of surface processes does not always hold. The event around day 219 seems to have been felt throughout the water column, as well as the general trend of warming from day 211 to day 220. It is unlikely that solar heating drove either signal since they were strongest at the deeper depths, while small but significant near the surface, which suggests these were advective phenomena. During this time, the SHEBA camp drifted from Chukchi Sea (500 m depth) over the shelf break to about 2000 m depth. It is likely that the complexity after day 210 in Fig.

4.5 is due to a combination of increased ice motion and vertical mixing as well as advection over a water column, which may contain a shelf slope boundary current whose properties are varying nonuniformly in the horizontal and even the vertical in the top 50 m.

The cumulative change in thermal energy measured in the top 30 m of the ocean is plotted in Fig. 4.3 (red curve). The version "corrected" for advection is shown with the dashed line. In both cases, the energy in the water column from day 170 to day 210 increases at a rate slightly less than predicted from a balance of solar input and the estimated heat flux to the ice (cyan). An average oceanic heating rate of 2 W m^{-2} over the period would make up the difference. Using the minimum estimate of transmittance for melt ponds and ice would lead to agreement (cyan dotted) from day 170 to day 205. There are two possible reasons the ocean did not warm as much as predicted from the energy balance. First, as described, from day 170 to day 210, a fresh surface layer trapped solar energy in the lead. The surface layer was very warm (up to 2 °C), but this heating could not be measured by the ocean city CTD. Eight leads within 30 km of SHEBA had a warm, fresh layer on day 203 [*Richter-Menge et al.*, 2001].

A second way to account for the lack of ocean warming is lateral melting of floe edges, which is not accounted for in the bulk heat flux formulation (Eq. 2.8). Significant lateral melting was observed at two leads instrumented by *Perovich et al.* [2003]. In fact, *Perovich et al.* [2003] partitioned the total energy expended on melting into lateral melting (5%), basal melting (18%), and surface melting (77%) on July 20 (day 201). They also show an equivalent vertical heat flux for observed bottom and top melt rates to be 19 and 80 W m^{-2}, respectively, implying an equivalent vertical heat flux for lateral melting of about 5 W m^{-2}—about twice the value required to account for the difference between the red and cyan curves in Fig. 4.3. Using the balance based on minimum transmittance data implies agreement between the predicted and observed ocean warming, and

would mean no lateral melting or heating of upper leads took place from day 170 to day 205, in disagreement with observations.

The warm surface layers in leads were eroded beginning on day 207 (also see *Richter-Menge et al.*, [2001]), but the mixed layer did not lose substantial thermal energy until the larger wind event on day 210. Then the observed ocean cooling is stronger than predicted, and the ocean remains cool rather than warming as the simple 3-way balance would suggest (cyan curve). A heat flux of 15 W m^{-2} over the period would make up the difference. Either the solar input is overestimated (unlikely, see above), or the ice-ocean heat flux is underestimated. The latter is true when compared to the results of *Perovich et al.* [2003]. They show the energy used in bottom melting from June 1 to August 31 (day 152 to day 242) was roughly 155 MJ m^{-2}, compared to 130 MJ m^{-2} estimated from Eq. 2.8 (Fig. 4.3). However on July 20 (day 201), the two estimates were much closer, 60 and 50 MJ m^{-2}, indicating the problem with using Eq. 2.8 occurs during a time of high ice speed. However, given the wide applicability of Eq. 2.8, a more likely factor is a contemporaneous increase in floe perimeter and other boundary characteristics.

The bulk heat flux formulation for bottom melt has been used successfully in the past [*McPhee*, 1992; *Maykut and McPhee*, 1995]. It assumes a horizontally representative mixed layer temperature and friction speed. However, *Perovich and Elder* [2002] observed large melt rates after day 213 near lead edges, and floe perimeter was observed to increase four-fold at the same time [*Perovich et al.*, 2002b]. While not previously considered to be important [*Maykut and McPhee*, 1995], horizontal variation in mixed layer temperature over the scale of a single floe may be significant (see Fig. 2.12). The estimate of ice-ocean heat flux in this study could be low because after day 213 there was more floe edge, which experienced warmer temperatures due to adjacent leads. The AMTV observations (Fig. 2.12) show the temperature can vary by as much as 0.5 C^{o} in 500 m. For this water to remain at the freezing point, it would have to freshen by about 1 psu,

which it does not. Therefore we can assume the freezing temperature behaves similarly to the *in situ* temperature. The horizontal variation in δT is important, as is the horizontal variation in stress.

The ice-ocean flux at ridge keels is likely to exceed the bulk estimate as well. A significant increase in roughness (say near ridge keels) may enhance the ice-ocean flux [*Wettlaufer*, 1991], and in fact the largest summer melt observed at SHEBA was an old ridge (average of 25 W m^{-2}) [*Perovich and Elder*, 2002]. The relative importance of lead edges after day 210 seems to win out over keels however. While the effect of ridge keels is greater at the greater ice speeds after day 210, the observed increase of melt near lead edges was much larger then under keels [*Perovich and Elder*, 2002].

Generally, the results discussed here and in *Perovich et al.* [2003] are in good agreement. They both indicate the SHEBA melt season was characterized by extra solar insolation over previous years (at least 160 MJ m^{-2} versus 150 MJ m^{-2} at AIDJEX), important contributions from bare ice and melt pond transmittances (0.03 and 0.15 required for their heat budget to balance equal our estimate exactly), and the rapid increase in ice-ocean heat flux at the late-July storm (confirmed by ice melt and oceanic temperature drop). The melt rate was found to be high around lead edges, and the AMTV somewhat suggests the same.

4.2 LARGE-SCALE IMPLICATIONS

Eicken et al. [2002] point out that fresh meltwater is prevented from percolating through the ice into the ocean in the early summer by layers of superimposed ice, where fresh meltwater meets below-freezing ice or brine. Our observations of mixed layer salinity are consistent with this meltwater retention. Water that enters through flaws and cracks often forms false bottoms, which also prevents the release of fresh water into the ocean. Meltwater flowing into larger leads does not form false bottoms, and if the buoyancy flux is strong enough compared to the surface stress, the meltwater remains in a fresh surface layer.

The birth of this layer can be predicted from the Obukhov length, which can be calculated from large-scale parameters: ice-ocean stress and an estimate of buoyancy flux in leads. The latter flux is difficult to estimate because it is not simply the basal melt rate or the surface melt rate. It is strongly dependent on the permeability of the ice and the surface melt rate [*Eicken et al.*, 2002]. As a first step in modeling such a process, one could assume that all of the surface melt runs into leads, i.e. impermeable ice. Then the surface melt would be multiplied by f_{bi} f_{ld}^{-1} to estimate the meltwater flux into leads. The surface melt could be held in a parameterized model surface reservoir until a critical Froude number was reached, at which point the lead flushing would begin.

The effect of surface trapping of meltwater in a large-scale model would be to change the seasonal cycle of mixed layer depth. Currently, Arctic Ocean models such as the model of *Zhang et al.* [1998] use a bulk mixed layer with an entrainment velocity predicting the mixed layer deepening throughout the fall, winter, and spring. When the surface buoyancy flux is strongly stabilizing, the mixed layer depth jumps to the top grid point (say 10 m). Later in the summer or early fall, when the ice melt tapers off, the mixed layer depth begins to gradually increase again. Keeping the mixed layer deeper by withholding ice melt until later into the summer might modify this "saw tooth" pattern. The jump to minimum depth would be delayed until the flushing event. In this case, the model mixed layer would be fresher and shallower longer into the fall. Once the stratification from the flushing event was broken in early fall, heat stored before the flushing event would be available to melt ice or limit ice production. In other words, the sudden release of fresh water would put a tight lid on heat absorbed below the new, shallow mixed layer until a fall or winter storm could deepen the mixed layer. If the fresh water gradually came into the mixed layer, the ocean would not be capped off and the mixed layer could provide thermal energy from early in the summer onwards.

Currently it appears from AIDJEX (1975) and SHEBA (1997-1998) that the heat deeper in the mixed layer did not reach the surface until later in the fall or winter. We calculate roughly 5-10 MJ m^{-2} remain in the top 30 m from SHEBA observations, and *Maykut and McPhee* [1995] calculate 15-20 MJ m^{-2} for AIDJEX, mostly between 30 and 50 m. In effect, storage in the upper pycnocline weakens the ice-albedo feedback, since incoming solar radiation cannot reach the ice surface until later in the year when solar radiation is weaker. It would slow ice production somewhat. Large-scale models need to accurately simulate the fresh water flux in order to accurately simulate the ice-albedo feedback. Surface meltwater retention does two things: lowers the albedo early in the summer through melt pond formation, and it results in a strong fresh water flux that "seals off" thermal energy in the pycnocline for future seasons.

4.3 FUTURE WORK

Small-scale, summertime, ice-ocean processes were observed in more detail than ever before in this study. A run-by-run analysis of the AMTV results may reveal even more information than was described here. The day-to-day conditions varied, and each run is a unique data set. The AMTV data set also contains very high-resolution ice draft data that has not been analyzed here.

The small-scale processes have been simulated with one-dimensional and two-dimensional models. Both of the models used here were successful at reproducing many features of the horizontally inhomogeneous boundary layer. However, both models had difficulty with the lead flushing event on day 210 to day 215. In the 1-D model, an initial subsurface temperature maximum decayed away, and the mixed layer was colder, fresher and thinner than observed. The 2-D unsteady was more realistic, although it was only run for an hour due to numerical instability. It was unable to simulate the observed deep temperature maximum in the upper pycnocline, but it successfully simulated a shallower subsurface temperature maximum. It also suggested a new mixing mechanism

due to horizontal density gradient in the presence of vertical shear. This model could be improved by enhancing the numerical stability to allow longer run times. The role of the mixing mechanism could then be further investigated.

A more sophisticated treatment of stratification and solar radiation may also improve the model. The model is initially neutrally stratified, so it is not possible to investigate the progression of the pre-existing mixed layer, and it is not possible to compare the modeled and observed heat content of the upper pycnocline. One way the ocean can warm in the pycnocline is by penetrative solar heating. The model uses a 4 m extinction depth for incoming shortwave radiation in the lead. However, the penetration of radiation in the visible is strongly dependent on chlorophyll [*Kantha and Clayson*, 2000]. In fact, incoming shortwave radiation can be attenuated to 10% of the surface value at a range of depths of 2-50 m, when chlorophyll ranges from 0.02 to 20 mg m^{-3} and the euphotic depth can vary from 10 to 100 m [*Morel and Antoine*, 1994]. At the SHEBA lead, chlorophyll was observed in the top 25-30 m, mostly due to two major phytoplankton blooms [*Pegau*, 2002]. Concentrations were as high as 1.5 mg m^{-3}, which would correspond to a 90% reduction by 20 m and a 99% reduction by 40 m. This could allow on the order of 10% of the visible radiation to heat the pycnocline directly. A model pycnocline and a more sophisticated treatment of shortwave penetration may reveal under what circumstances a warm core is maintained, as throughout the storm of day 210.

The quasi-steady period (day 220) was simulated very well, particularly by the 2-D unsteady model. It differed from AMTV observations in its prediction of heat flux under the ice downstream of the lead. However this may be due to a slight difference in the depth penetration of the boundary layer disturbance; the model results between 5 and 10 m agreed more closely with the AMTV 5 m results. The model agreed fairly well with ablation measurements at the lead edge. Overall the 2-D unsteady model results illustrate the importance of spatial

variability and the advective terms in exploring the boundary layer observations even under relatively steady forcing.

Large-scale heat budget calculations need to accurately represent the ice-ocean heat flux, which we assert is dependent on lead fraction and floe perimeter. While reasonably effective, the bulk exchange formulation does not agree exactly with the observed average melt rates in late summer. This is likely because actual rates vary greatly depending on ice type and location. Ridges and lead edges thinned the most, especially after the lead fraction and ice-ocean stress increased [*Perovich et al.*, 2003]. The horizontal variability in ice-ocean heat flux needs to be incorporated somehow into any large-scale estimate. Horizontal variation in heat content and in ice-ocean stress are important factors to consider.

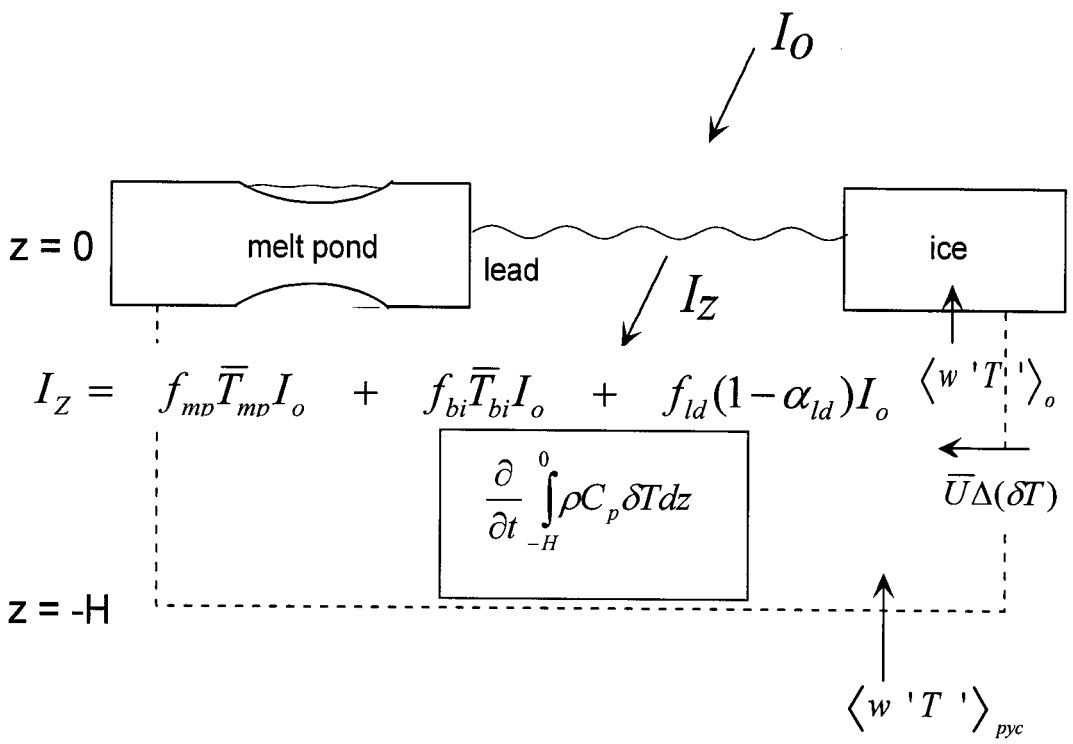

Figure 4.1. Illustration of the heat balance of the upper ocean under sea ice. The central box is the rate of change of thermal energy inside the dotted lines. This could be nonzero due to solar insolation through leads with a given albedo, or through melt ponds or ice with a given transmittance. The area fraction of each type is indicated by *f*. Sensible heat flux at the ice-ocean interface and the pycnocline as well as advection of warm water also contribute. Net longwave radiation through leads is not shown; it is generally small unless lead fraction is high.

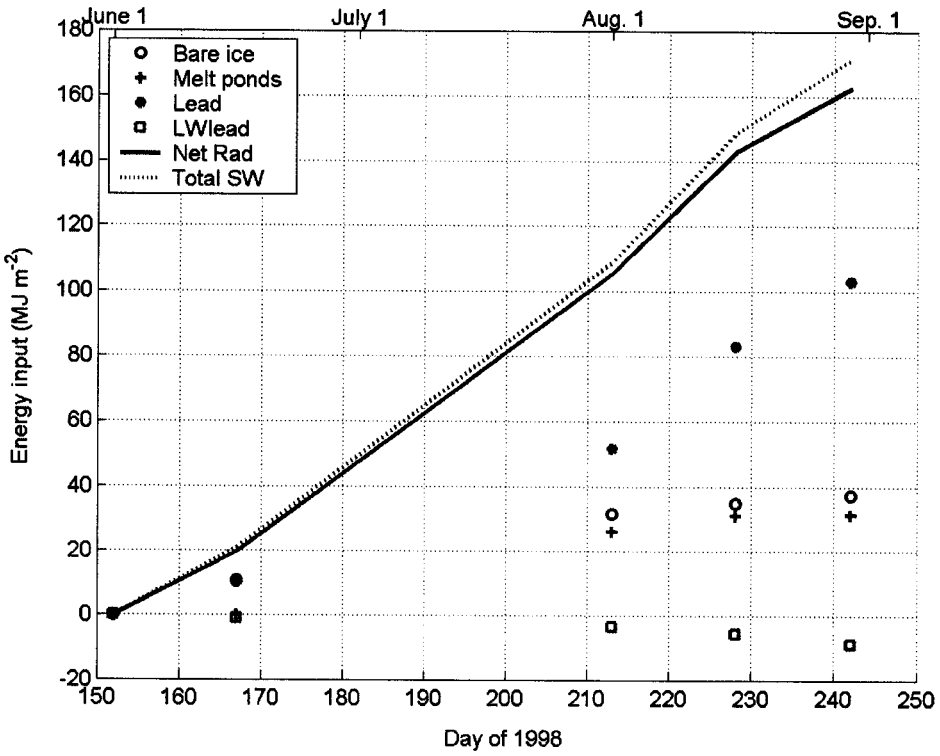

Figure 4.2. The accumulation of shortwave irradiance to the ocean through leads (red stars), melt ponds (green crosses), bare ice (blue circles), and the total (dashed line). Energy is contributed from melt ponds mainly during July, and from leads mostly from late July to early August (when lead fraction was highest). Including net longwave losses through leads results in the black line. See Table 2 for area fractions and solar insolation values used to make this plot.

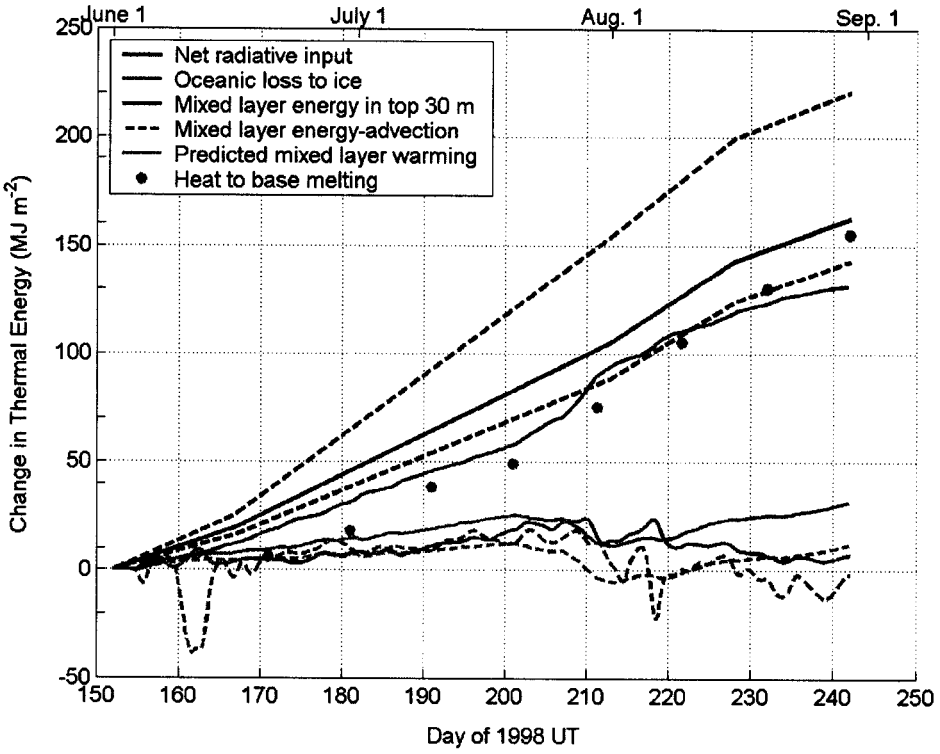

Figure 4.3. The major terms of the heat budget for the upper 30 m of the ocean at SHEBA. Net radiation input (black) is the same as Fig. 4.2, but now with dashed lines representing the maximum and minimum inputs based on the highest and lowest observed transmittances. Oceanic loss (green line) is calculated from the surface friction velocity and elevation above freezing at 5 m from the ocean city CTD. The difference in these two is the predicted ocean warming (cyan) and minimum warming (dashed cyan). The actual change in heat content is shown by the red (solid) with the dashed accounting for advective change in heat content. Heat used for bottom melting from balance measurements shown in green dots [*Perovich et al.*, 2003].

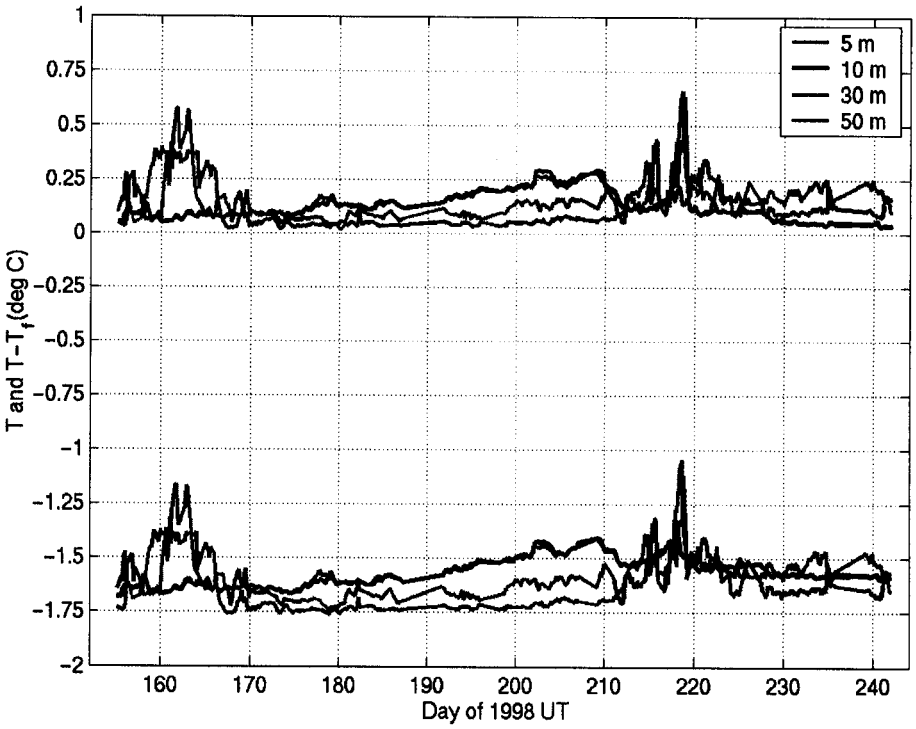

Figure 4.4. Temperature (bottom) and elevation above salinity-determined freezing temperature (top) at four different depths measured by the main ocean city CTD during June, July, and August. Data have been smoothed with a 1-day running mean.

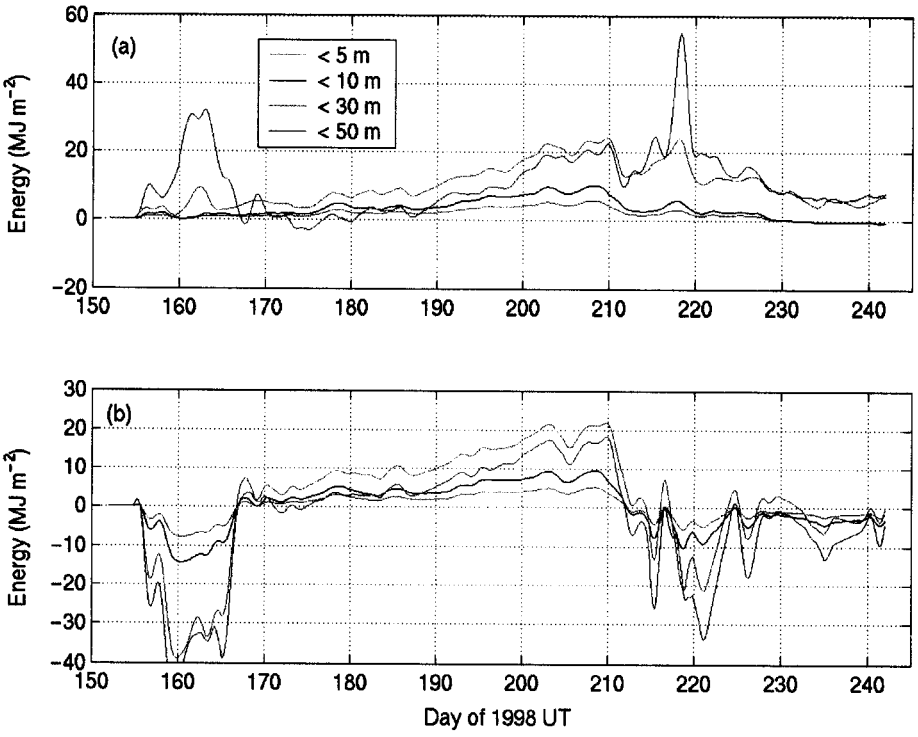

Figure 4.5. Change in thermal energy of the ocean above four depths based on SHEBA ocean city CTD casts. In (a), the change is calculated by simply adding the integral from depth to the surface to the previous cast. In (b), the vertical integral of an imaginary 30 m column that changes uniformly at the rate observed at 30 m is subtracted from (a). Data have been smoothed with a 1-day running mean.

LIST OF REFERENCES

Aagaard, K., and E. C. Carmack, 1989. The role of sea ice and other fresh water in the Arctic circulation. *J. Geophys. Res.*, *94*(C10), 14,485-14,498.

Andreas, E. L., C. W. Fairall, P. S. Guest, and P. O. G. Persson, 2001. The air-ice drag coefficient measured for a year over Arctic sea ice in *Proceedings of the Sixth Conference on Polar Meteorology and Oceanography, 14-18 May 2001, San Diego*, pp. 300-303, Am. Meteorol. Soc., Boston, Mass.

Badgley, F. J., 1966. Heat budget at the surface of the Arctic Ocean. In J. O. Fletcher (Ed.): *Proceedings on the Symposium on the Arctic Heat Budget and Atmospheric Circulation*, Rand Corporation, Santa Monica, 267-277.

Carmack, E. C., 2000. The Arctic Ocean's freshwater budget: Sources, storage and export. In E. L. Lewis et al. (Eds): *The Freshwater Budget of the Arctic Ocean*, NATO/WCRP/AOSB, Kluwer Academic Publications, Boston, 91-126.

Crawford, G., L. Padman, and M. McPhee, 1999. Turbulent mixing in Barrow Strait. *Continental Shelf Research*, *19*, 205-245.

Curry, J. A., J. L. Schramm, and E. E. Ebert, 1995. Sea ice-albedo climate feedback mechanism. *J. Climate*, *8*(2), 240-247.

Ebert, E. E., and J. A. Curry, 1993. An intermediate one-dimensional thermodynamic sea ice model for investigating ice-atmosphere interactions. *J. Geophys. Res.*, *98*(C6), 10,085-10,109.

Edson, J. B., C. W. Fairall, P. G. Mestayer, and S. E. Larsen, 1991. A study of the inertial-dissipation method for computing air-sea fluxes. *J. Geophys. Res.*, *96*(C6), 10,689-10,711.

Eicken, H., H. R. Krouse, D. Kadko, and D. K. Perovich, 2002. Tracer studies of pathways and rates of meltwater transport through Arctic summer sea ice. *J. Geophys. Res.*, *107*(C10), 8046, doi:10.1029/2000JC000583.

Fleury, M., and R. G. Lueck, 1994. Direct heat flux estimates using a towed vehicle. *J. Phys. Oceanogr.*, *24*, 801-818.

Garratt, J. R., 1990. The internal boundary layer—a review. *Boundary-Layer Meteorol.*, *50*(1-4), 171-203.

Gelb, A., ed., 1974. *Applied Optimal Estimation.* The M. I. T. Press, Cambridge, 374 pp.

Grenfell, T. C., and D. K. Perovich, 1984. Spectral albedos of sea ice and incident solar irradiance in the southern Beaufort Sea. *J. Geophys. Res.*, *89*(C3), 3573-3580.

Hayes, D. R., and J. H. Morison, 2002. Determining turbulent vertical velocity and fluxes of heat and salt with an autonomous underwater vehicle. *J. Atmos. Oceanic Technol.*, *19*(C2), 759-779.

Holland, M. M., J. A. Curry, and J. L. Schramm, 1997. Modeling the thermodynamics of a sea ice thickness distribution, 2, Sea ice/ocean interactions. *J. Geophys. Res.*, *102*(C10), 23,093-23,107.

Kantha, L. H., and C. A. Clayson, 2000. *Small Scale Processes in Geophysical Fluid Flows*. Academic Press, San Francisco, 888 pp.

LeadEx Group, 1993. The LeadEx Experiment. *Eos Trans. AGU, 74*(35), 393, 396-397.

Light, B., T. C. Grenfell, and D. K. Perovich, 2003. Transmission of solar radiation by a summer sea ice cover. Poster presented at Seventh Conference on Polar Meteorology and Oceanography and Joint Symposium on High-Latitude Climate Variations, AMS, Hyannis, MA, 12-16 May.

Lueck, R. G., and F. Wolk, 1999. An efficient method for determining the significance of covariance estimates. *J. Atmos. Oceanic Technol.*, *16*(6), 773-775.

Manabe, S., R. J. Stouffer, M. J. Spelman, and K. Bryan, 1991. Transient response of a coupled ocean-atmosphere model to gradual changes of atmospheric CO_2, Part I: Annual mean response. *J. Climate*, *4*(8), 785-818.

Martin, S., and P. Kauffman, 1974. The evolution of under-ice melt ponds, or double diffusion at the freezing point. *J. Fluid Mech.*, *64*, 507-527.

Maykut, G. A., 1978. Energy exchange over young sea ice in the central Arctic. *J. Geophys. Res.*, *83*(C7), 3646-3658.

Maykut, G. A., and D. K. Perovich, 1987. The role of shortwave radiation in the summer decay of a sea ice cover. *J. Geophys. Res.*, *92*(C7), 7032-7044.

Maykut, G. A., and M. G. McPhee, 1995. Solar heating of the Arctic mixed layer. *J. Geophys. Res.*, *100*(C12), 24,691-24,703.

McPhee, M. G., 1981. An analytic similarity theory for the planetary boundary layer stabilized by surface buoyancy. *Boundary-Layer Meteorol.*, *21*, 325-339.

McPhee, M. G., 1983. Turbulent heat and momentum transfer in the oceanic boundary layer under melting pack ice. *J. Geophys. Res.*, *88*(C5), 2827-2835.

McPhee, M. G., 1986a. Analysis and prediction of short-term ice drift, paper presented at the Fifth International Offshore Mechanics and Arctic Engineering Symposium. Am. Soc. Of Mech. Eng., Tokyo, April 13-18.

McPhee, M. G., 1986b. The Upper Ocean. In N. Untersteiner, (Ed.): *The Geophysics of Sea Ice. Proceedings of the NATO Advanced Study Institute on Air-Sea-Ice Interaction.* Plenum, New York, pp. 339-394.

McPhee, M. G., 1987. A time-dependent model for turbulent transfer in a stratified oceanic boundary layer. *J. Geophys. Res.*, *92*(C7), 6977-7986.

McPhee, M. G., 1989. A rigid, cable-lowered instrument frame for measuring turbulence and internal waves in the Arctic. *IEEE J. Oceanic Eng.*, *14*(2), 203-207.

McPhee, M. G., 1990. Small-scale processes. In: Smith, W. O. (Ed.), *Polar Oceanography. Part A: Physical Science*. Academic Press, San Diego, pp. 287-334.

McPhee, M. G., 1992. Turbulent heat flux in the upper ocean under sea ice. *J. Geophys. Res.*, *97*(C4), 5365-5379.

McPhee, M. G., 1994. On the turbulent mixing length in the oceanic boundary layer. *J. Phys. Oceanogr.*, *24*, 2014-2031.

McPhee, M. G., 1999. Parameterization of mixing in the ocean boundary layer. *J. Mar. Syst.*, *21*(1-4), 55-65.

McPhee, M. G., 2002. Turbulent stress at the ice/ocean interface and bottom surface hydraulic roughness during the SHEBA drift. *J. Geophys. Res.*, *107*(C10), 8037, doi:10.1029/2000JC000633.

McPhee, M. G., 2003. A spectral technique for estimating momentum and scalar flux magnitude in the ocean boundary layer under pack ice during SHEBA, *J. Phys. Oceanogr.*, submitted.

McPhee, M. G., and J. D. Smith, 1976. Measurements of the turbulent boundary layer under pack ice. *J. Geophys. Res.*, 6(5), 696-711.

McPhee, M. G., and L. H. Kantha, 1989. Generation of internal waves by sea ice. *J. Geophys. Res.*, *94*(C3), 3287-3302.

McPhee, M. G., and T. P. Stanton, 1996. Turbulence in the statically unstable oceanic boundary layer under Arctic leads. *J. Geophys. Res.*, *101*(C3), 6409-28.

McPhee, M. G., G. A. Maykut, and J. H. Morison, 1987. Dynamics and thermodynamics of the ice/upper ocean system in the marginal ice zone of the Greenland Sea. *J. Geophys. Res.*, *92*(C7), 7017-7031.

McPhee, M. G., T. P. Stanton, J. H. Morison, and D. G. Martinson, 1998. Freshening of the upper ocean in the Arctic: Is perennial sea ice disappearing? *Geophys. Res. Lett.*, *25*(10), 1729-1732.

Mellor, G. L., and T. Yamada, 1974. A hierarchy of turbulence closure models for planetary boundary layers. *J. Atmos. Sci.*, *31*, 1791-1806. [Corrigendum, 1977. *J. Atmos. Sci.*, *43*, 1482.]

Mellor, G. L., and T. Yamada, 1982. Development of a turbulence closure for geophysical fluid problems. *Rev. Geophys. Space Phys.*, *20*, 851-875.

Mellor, G. L., M. G. McPhee, and M. Steele, 1986. Ice-seawater turbulent boundary layer interaction with melting or freezing. *J. Phys. Oceanogr.*, *16*, 1829-1846.

Morel, A., and D. Antoine, 1994. Heating rate within the upper ocean in relation to its bio-optical state. *J. Phys. Oceanogr. 24*, 1652-1665.

Morison, J. H., and M. G. McPhee, 1998. Lead convection measured with an autonomous underwater vehicle. *J. Geophys. Res.*, *103*(C2), 3257-3281.

Morison, J. H., M. G. McPhee, and G. A. Maykut, 1987. Boundary layer, upper ocean, and ice observations in the Greenland Sea marginal ice zone. *J. Geophys. Res.*, *92*(C7), 6987-7011.

Morison, J. H., M. G. McPhee, T. B. Curtin, and C. A. Paulson, 1992. The oceanography of winter leads. *J. Geophys. Res.*, *97*(C7), 11,199-11,218.

Nihashi, S., and K. I. Ohshima, 2001. Relationship between ice decay and solar heating through open water in the Antarctic sea ice zone. *J. Geophys. Res.*, *106*(C8), 16,767-16,782.

Paulson, C. A., and W. S. Pegau, 2001. The summertime thermohaline evolution of an Arctic lead: Heat budget of the surface layer in *Proceedings of the Sixth Conference on Polar Meteorology and Oceanography, 14-18 May 2001, San Diego*, pp. 271-274, Am. Meteorol. Soc., Boston, Mass.

Pegau, W. S., 2002. Inherent optical properties of the central Arctic surface waters, *J. Geophys. Res.*, *107*(C10), 8035, doi:10.1029/2000JC000382.

Pegau, W. S., and C. A. Paulson, 2001. The albedo of Arctic leads in summer. *Ann. Glaciol.*, *33*, 221-224.

Percival, D. B., and A. T. Walden, 1993. *Spectral Analysis for Physical Applications: Multitaper and Conventional Univariate Techniques*. Cambridge University Press, Cambridge, 583 pp.

Perovich, D. K., and B. Elder, 2002. Estimates of ocean heat flux at SHEBA, *Geophys. Res. Lett.*, *29*(10), 1344, doi:10.1029/2001GL014171.

Perovich, D. K., T. C. Grenfell, B. Light, and P. V. Hobbs, 2002a. Seasonal evolution of the albedo of multiyear Arctic sea ice. *J. Geophys. Res.*, *107*(C10), 8044, doi:10.1029/2000JC000438.

Perovich, D. K., W. B. Tucker III, and K. A. Ligett, 2002b. Aerial observations of the evolution of ice surface conditions during summer. *J. Geophys. Res.*, *107*(C10), 8048, doi:10.1029/2000JC000449.

Perovich, D. K., T. C. Grenfell, J. A. Richter-Menge, B. Light, W. B. Tucker III, and H. Eicken, 2003. Thin and thinner: Sea ice mass balance measurements during SHEBA. *J. Geophys. Res.*, *108*(C3), 8050, doi:10.1029/2001JC001079.

Perovich, D. K., T. C. Grenfell, B. Light, J. A. Richter-Menge, M. Sturm, W. B. Tucker III, H. Eicken, G. A. Maykut, and B. Elder, 1999. *SHEBA: Snow and Ice Studies*. Cold. Reg. Res. And Eng. Lab., Hanover, NH, [CD-ROM].

Persson, P. O. G., C. W. Fairall, E. L. Andreas, P. S. Guest, and D. K. Perovich, 2002. Measurements near the atmospheric surface flux group tower at SHEBA: Near-surface conditions and surface energy budget. *J. Geophys. Res.*, *107*(C10), 8045, doi:10.1029/2000JC000705.

Polyakov, I. V., A. Y. Proshutinsky, and M. A. Johnson, 1999. Seasonal cycles in two regimes of Arctic climate. *J. Geophys. Res.*, *104*(C11), 25,761-25,788.

Proshutinsky, A. Y., and M. A. Johnson, 1997. Two circulation regimes of the wind-driven Arctic Ocean. *J. Geophys. Res.*, *102*(C6), 12,493-12,514.

Randall, D., J. Curry, D. Battisti, G. Flato, R. Grumbine, S. Hakkinen, D. Martinson, R. Preller, J. Walsh, and J. Weatherly, 1998. Status of and outlook for large-scale modeling of atmosphere-ice-ocean interactions in the Arctic. *Bull. Amer. Meteor. Soc.*, *79*(2), 197-219.

Richter-Menge, J. A., D. K. Perovich, and W. S. Pegau, 2001. Summer ice dynamics during SHEBA and its effect on the ocean heat content. *Ann. Glaciol.*, *33*, 201-206.

Rind, D. R., Healy, C. Parkinson, and D. Martinson, 1995. The role of sea ice in $2xCO_2$ climate model sensitivity. Part I: the total influence of sea-ice thickness and extent. *J. Climate*, *8*(3), 449-463.

Rothrock, D. A., Y. Yu, and G. A. Maykut, 1999. Thinning of the Arctic sea ice cover. *Geophys. Res. Lett.*, *26*(23), 3469-3472.

Ruffieux, D., P. O. G. Persson, C. W. Fairall, and D. E. Wolf, 1995. Ice pack and lead surface energy budgets during LEADEX 1992. *J. Geophys. Res.*, *100*(C3), 4593-4612.

SEARCH SSC, 2001. *SEARCH: Study of Environmental Arctic Change, Science Plan*, Polar Science Center, Applied Physics Laboratory, University of Washington, Seattle, 89pp.

Serreze, M. C., J. E. Walsh, F. S. Chapin III, T. Osterkamp, M. Dyurgerov, and V. Romanovsky, 2000. Observational evidence of recent change in the northern high latitude environment. *Clim. Change*, *46*(1-2), 159-207.

Smith, D. C. IV, and J. H. Morison, 1993. A numerical study of haline convection beneath leads in sea ice. *J. Geophys. Res.*, *98*(C6), 10,069-10,083.

Smith, D. C. IV, and J. H. Morison, 1998. Nonhydrostatic haline convection under leads in sea ice. *J. Geophys. Res.*, *103*(C2), 3233-3247.

Smith, D. C. IV, J. W. Lavelle, and H. J. S. Fernando, 2002. Arctic Ocean mixed-layer eddy generation under leads in sea ice. *J. Geophys. Res.*, *107*(C8), 3103, doi:10.1029/2001JC000822.

Smith, D. M., 1998. Recent increase in the length of the melt season of perennial Arctic sea ice. *Geophys. Res. Lett.*, *25*(5), 655-658.

Steele, M., J. H. Morison, and N. Untersteiner, 1989. The partition of air-ice-ocean momentum exchange as a function of ice concentration, floe size, and draft. *J. Geophys. Res.*, *94*(C9), 12,739-12,750.

Stern, H. L., and R. E. Moritz, 2002. Sea ice kinematics and surface properties from RADARSAT synthetic aperture radar during the SHEBA drift. *J. Geophys. Res.*, *107*(C10), 8028, doi:10.1029/2000JC000472.

Untersteiner, N., 1961. On the mass and heat budget of Arctic sea ice. *Arch. Meteorol. Geophys. Bioklimatol., Ser: A*, *12*, 151-182.

Uttal, T., J. A. Curry, M. G. McPhee, D. K. Perovich, R. E. Moritz, J. A. Maslanik, P. S. Guest, H. L. Stern, J. A. Moore, R. Turenne, A. Heiberg, M. C. Serreze, D. P. Wylie, O. G. Persson, C. A. Paulson, C. Halle, J. H. Morison, P. A. Wheeler, A. Makshtas, H. Welch, M. D. Shupe, J. M. Intrieri, K. Stamnes, R. W. Lindsey, R. Pinkel, W. S. Pegau, T. P. Stanton, and T. C. Grenfell, 2002. Surface heat budget of the Arctic Ocean. *Bull. Amer. Meteor. Soc.*, *83*(2), 255-275.

Walsh, J. E., W. L. Chapman, and T. L. Shy, 1996. Recent decrease of sea level pressure in the central Arctic. *J. Climate*, *9*(2), 480-486.

Wettlaufer, J. S., 1991. Heat flux at the ice-ocean interface. *J. Geophys. Res.*, *96*(C4), 7215-7236.

Zhang, J., W. D. Hibler III, M. Steele, and D. A. Rothrock, 1998. Arctic ice-ocean modeling with and without climate restoring. J. Phys. Oceanogr., 28, 191-217.

APPENDIX A

Spectral Determination of Friction Speed

Let the weighted spectral density of vertical velocity (ϕ) be a function of turbulent kinetic energy production (P) and wavenumber (k).

$$\phi(k) \equiv kS_{ww}(k) = f(P,k) \tag{A.1}$$

$$P = \left| u_*^2 \frac{dU}{dz} \right| = \frac{u_*^3}{\lambda} = u_*^3 k_{\max} c_\lambda^{-1} \tag{A.2}$$

In Eq. A.2, we assume shear times eddy viscosity equals the kinematic stress. The eddy viscosity equals friction speed times mixing length (λ), so the shear turns out to be friction speed divided by mixing length. An empirical constant of proportionality approximately equal to 0.85 is c_λ. Using dimensional analysis to obtain the correct dimensions of ϕ, *McPhee* [2003] obtains the following relationship.

$$\Phi \equiv \frac{\phi}{u_*^2} = c_\gamma \left(\frac{k}{k_{\max}} \right)^{-\frac{2}{3}} \equiv c_\gamma \gamma^{-\frac{2}{3}} \tag{A.3}$$

Therefore, the non-dimensional spectrum of vertical water velocity (weighted spectral density divided by the square of friction speed) has a universal shape and level in the inertial subrange. If the proportionality constant, c_γ, is known, observed weighted spectra can be appropriately nondimensionalized to achieve the universal spectrum; i.e., friction speed is calculated to do just that.

McPhee [2003] uses turbulent instrument clusters to calculate friction speed directly using Eq. 2.4 in 3-hour averages of 15-minute blocks of data from

November through March at ice station SHEBA. He then calculates the weighted spectrum of vertical water velocity for each 15-minute segment and smooths into logarithmic wavenumber bins, averaging over 3 hours, and finally nondimensionalizing by friction speed squared. After nondimensionalizing the wavenumber by k_{max}, all 387 3-hour nondimensional spectra collapse well to a single curve in the center of the expected scatter. Taking the logarithm of Eq. A.3 and finding the value of Φ at a given γ in the inertial subrange provides an estimate of c_γ (0.48). *McPhee* [2003] states that Eq. A.3 neglects the turbulent kinetic energy sink of stabilizing buoyancy and assumes horizontally homogeneous conditions. Our study takes place in July and August, when stabilizing buoyancy and horizontal variability were often strong, but we will proceed anyway with this in mind. The effect of stabilizing buoyancy will be discussed briefly at the end of this appendix.

Using turbulent instrument cluster data from the summer to form nondimensional spectra of vertical water velocity gives results similar to *McPhee* [2003]. However, the inertial subrange is found to be less well-defined; the spectra seem to fall off at a much lower logarithm of nondimensional wavenumber (0.2 vs. 0.7). In Fig. A.1 are plotted nondimensional spectra of vertical water velocity from three different turbulence clusters: two levels at the interior of a floe (about 3.5 m and 7.5 m depths from days 210-215 and 219-220 of 1998) and one from a lead edge (about 5 m in depth from days 219-220 of 1998). Each spectrum represents a 3-hour (floe interior) or 1-hour average (lead edge). It appears that the deeper cluster and lead edge cluster give slightly different results than the upper cluster in the interior, perhaps due to a very shallow boundary layer and/or significant buoyancy flux at the cluster levels. It is also found that the clusters give slightly different constants of proportionality (0.33, 0.49, and 0.25 for interior shallow, interior deep, and lead edge, respectively), found by averaging the values from the spectra. At the shallow cluster in the interior we see excellent agreement for friction speed calculated

with the two methods: directly and only using the vertical water velocity spectra (Fig. A.2). Other clusters show less correspondence between the indirect and direct methods. The value of 0.48 was used for c_γ for all clusters. It seems the method is quite sensitive to the choice of c_γ, since using the derived value for each respective cluster generally leads to a proportion between the two methods closer to one. The correlation coefficients between the two methods are unchanged however.

Now Eq. A.3 can be used to calculate friction speed from the water velocity spectrum calculated for each 100 m segment of AMTV data. First, we calculate the weighted spectra as described (Fig. A.3). The inertial subrange, although small, seems to be centered on $\gamma_* = 0.1$. Note the double-humped structure in many of the spectra. All valid 100-m segments have been used, regardless of run depth. Runs resulting in a friction speed of less than 0.008 m s^{-1} are in red. A three-dimensional view of the spectra illustrates the time dependence and shows higher spectral levels during the storm from days 210-215 clearly (Fig. A.4). Once γ_* is chosen, we calculate the value of the nondimensional universal spectrum $\Phi(\gamma_*)$ from Eq. A.3; we use c_γ=0.48, as in *McPhee* [2003], and we note that there is evidence to suggest smaller values. However, these values may be due to significant buoyancy flux or a violation of horizontal homogeneity. Using values of 0.25 or 0.33 introduces a uniform positive bias of 39% or 21%, respectively. We choose the value that matches the surface estimate of friction speed most closely, which also happens to be the value found by *McPhee* [2003]. Next we look up the value of the actual weighted spectrum log ϕ_* at log k_* = log k_{max} +log γ_*. Finally, we use the definition of Φ to calculate the friction speed:

$$\log u_* = 0.5(\log \phi_* - \log \Phi(\gamma_*)) \qquad \text{(A.4)}$$

A confidence interval is calculated from the confidence interval in the spectral estimate of ϕ and amounts to a ±17% band.

The procedure gives good agreement with surface friction velocity, despite the likely presence of stabilizing buoyancy flux and horizontal inhomogeneity, even for runs outside the boundary layer (Fig. 2.16). As long as the mixing length depends on the location of the maximum in the vertical water velocity spectrum, and there exists an inertial subrange, this method is valid in the boundary layer. As the buoyancy flux increases and mixing length decreases, the maximum in the vertical velocity spectrum moves to higher wavenumbers, and the inertial subrange becomes shorter. Eventually buoyancy flux could be so great as to play a part in the balance of the production of turbulence, and this method would fail.

If we scale a new sink term in the turbulent kinetic energy equation, buoyancy flux, we see it has a similar form to the production term.

$$P_B = -\frac{g}{\rho}\langle w'\rho'\rangle = -\frac{g}{\rho}\frac{u_{*0}^3}{\kappa L_0}, \tag{A.5}$$

where we have simply applied the definition of the Obukhov length (Eq. 2.16). The Obukhov length plays a similar role in the buoyancy term to mixing length in the production term. As buoyancy flux becomes very large, both mixing length and Obukhov length approach zero, but their ratio approaches a constant. Therefore production and buoyancy flux destruction increase in tandem as Obukhov length decreases, which will continue until molecular scales are reached or horizontal homogeneity is broken by proximity to roughness elements. This method should work until that point because there still should be a region near the boundary, albeit small, where energy cascade depends on production and wavenumber (inertial sublayer or log layer). The key is making observations in that region that resolve the inertial subrange.

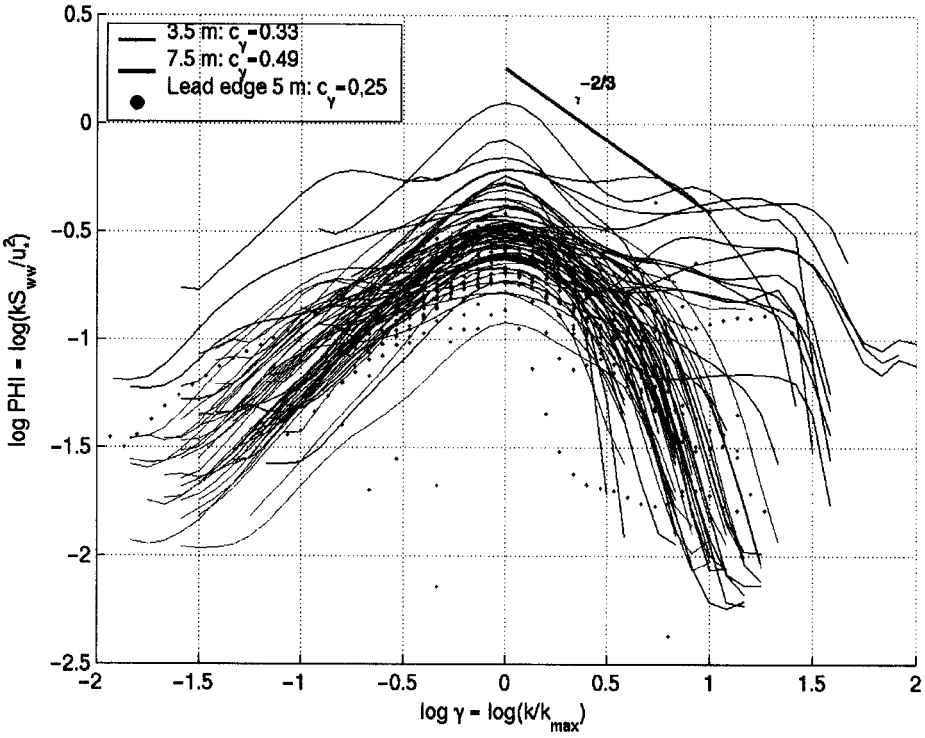

Figure A.1. Vertical water velocity spectra from three turbulence instrument clusters deployed at SHEBA normalized by the covariance estimate of friction speed. The clusters are from depths of 3.5 m, 7.5 m, and 5.0 m. The former two were deployed at ocean city (mean ice draft of 1.4 m) from 210-215 and 219-220 and the latter at the lead edge ("Sarah's Lake") on 205, 208, and 219-220. The slope of the inertial subrange is shown in green. By definition, all spectra have their maxima at log $\gamma = 0$.

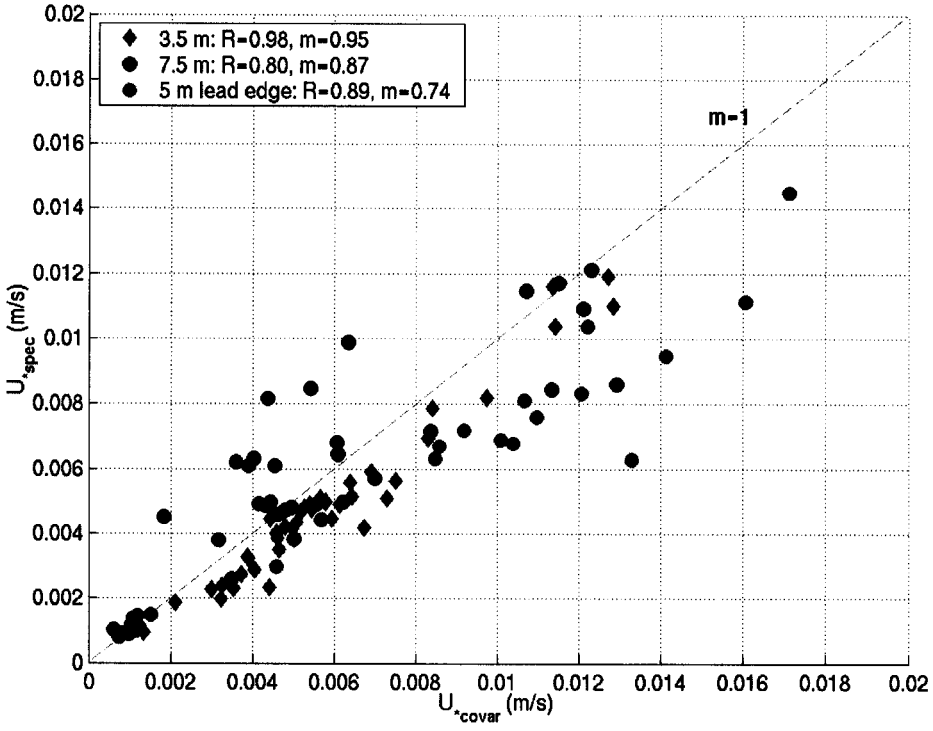

Figure A.2. Friction speed from spectral methods (ordinate) against friction speed directly from velocity component covariances (abscissa). The same three data sets from Fig. A.1 are used. A proportionality constant (c_γ) of 0.48 has been assumed. Using the respective constant for each cluster leads to slopes closer to one, but the correlation coefficients remain the same.

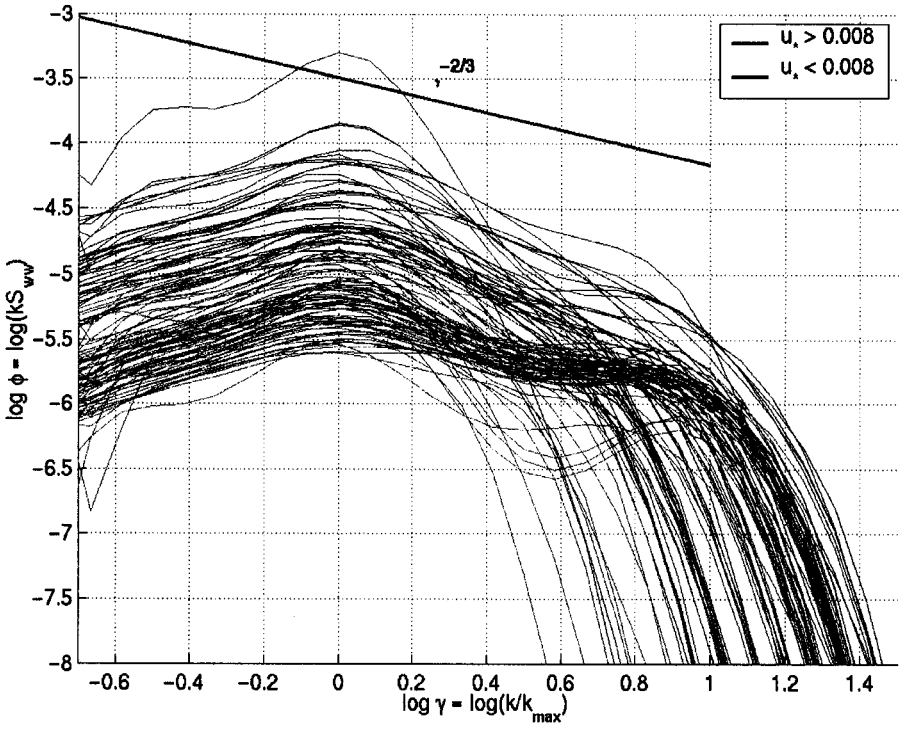

Figure A.3. Weighted spectra of AMTV-derived vertical water velocity. Each 100 m of data were used to calculate a spectrum, which has been fit with a polynomial to find the maximum. Only one of every five spectra is shown here. The friction velocity was calculated by the spectral levels at γ=0.1, and the spectra have been color-coded according to the magnitude of the result (blue is above 0.008 m s^{-1}).

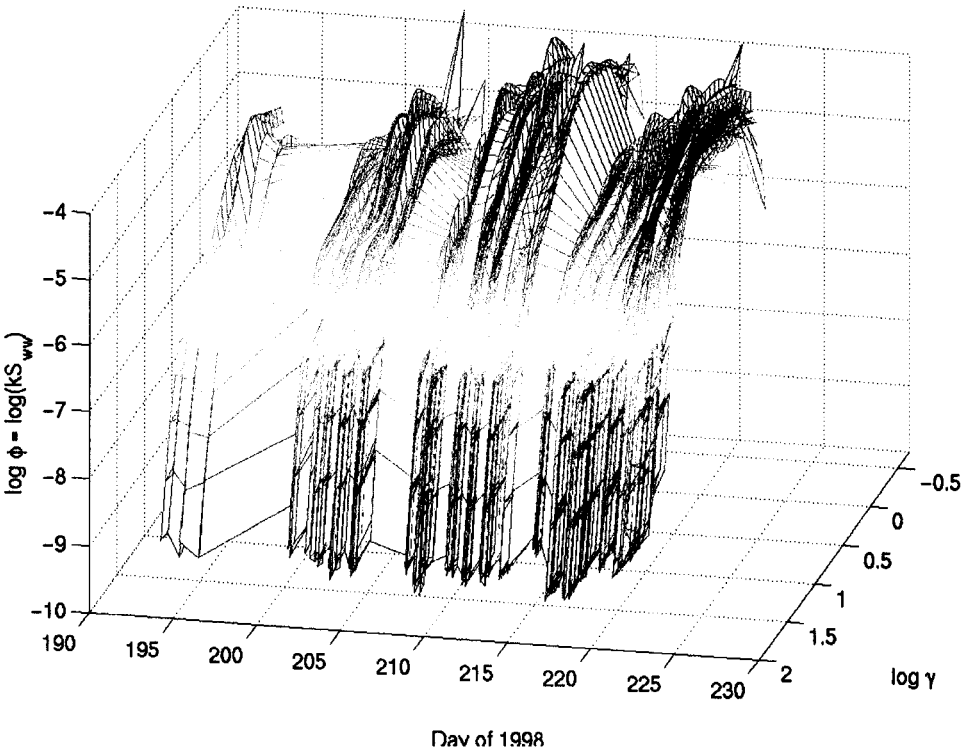

Figure A.4. As in Fig. A.3, but all AMTV vertical water velocity spectra are shown in three dimensions. The color of the surface corresponds to its height (spectral density). Note the increase in spectral density in tandem with the interfacial friction speed (Fig. 2.16), which ultimately results in reasonable estimates of friction speed at the AMTV operating depths.

APPENDIX B

Determining Turbulent Vertical Velocity, and Fluxes of Heat and Salt with an Autonomous Underwater Vehicle

DANIEL R. HAYES AND JAMES H. MORISON

Polar Science Center, Applied Physics Laboratory, University of Washington, Seattle, Washington

(Manuscript received 10 October 2000, in final form 6 September 2001)

ABSTRACT

The authors show that vertical turbulent fluxes in the upper ocean can be measured directly with an autonomous underwater vehicle (AUV). A horizontal profile of vertical water velocity is obtained by applying a Kalman smoother to AUV motion data. The smoother uses a linearized model for vehicle motion and vehicle data such as depth, pitch, and pitch rate to produce an optimal estimate of the state of the system, which includes other vehicle variables and the vertical water velocity. Vertical water velocity estimated by applying the smoother to data from the autonomous microconductivity temperature vehicle (AMTV) is accurate at horizontal scales from three to several hundred meters, encompassing the energy-containing scales of most oceanic turbulence. The zero-lag covariances between vertical water velocity and concurrent measurements of temperature or salinity represent the heat and salt fluxes, respectively. The authors have measured horizontal profiles of turbulent fluxes with two different AUVs in three separate polar ocean experiments using this technique. Flux magnitudes and directions are reasonable and in general agreement with fixed turbulence sensors. With this technique, one can gather boundary layer data in inaccessible regions without disturbing or affecting the surface.

1. Introduction

The vertical turbulent fluxes of heat and salt in the oceanic boundary layer are critical elements of ocean–sea-ice–atmosphere interaction. The fluxes are defined in the Reynolds decomposition of the heat and salt conservation equations as $F_{\text{heat}} = \rho C_p \langle w_w T' \rangle$, and $F_{\text{salt}} = \rho \langle w_w S' \rangle$, where w_w is the turbulent fluctuation in vertical water velocity, T' and S' are the fluctuations in temperature and salinity (in parts per thousand) from their respective means, ρ is the mean water density, and C_p is the specific heat capacity of the water. The angle brackets indicate an ensemble average over many realizations of the turbulent flow. These fluxes are difficult to measure directly primarily because it is difficult to measure w_w, especially in the open ocean where a stable measurement platform is nearly impossible to achieve. A variety of indirect methods (e.g., Osborn and Cox 1972) have been developed to estimate the fluxes based on measurements at the smallest scales of turbulence and the assumption of a steady-state energy cascade from the energy-containing turbulence scales to the dissipation scales. In general, indirect methods assume steady and homogeneous turbulence. See Fleury and Lueck (1994) for a review of indirect methods.

Direct measurements of the turbulent fluxes have been made in polar seas where the ice cover provides a stable platform from which sensitive velocity sensors can be suspended. McPhee (1994) and McPhee and Stanton (1996) describe under-ice deployment of vertical masts of turbulence instrument clusters (TICs) composed of orthogonal velocity, temperature, and conductivity sensors. McPhee and Stanton (1996) also compare direct flux measurements to fluxes estimated using a turbulent microstructure profiler and assuming a local balance between production and dissipation of turbulent kinetic energy.

However, observations in the under-ice boundary layer present their own special challenges. Chief among these is the spatial variability of the under-ice boundary layer. The ice cover may consist of large areas of thick multiyear ice, smooth new ice, and open water. Each type of surface provides a different surface boundary condition with unique fluxes of heat, salt, and momentum. The effect of this horizontal variability has become a primary area of interest in the study of air–sea-ice–ocean interaction. Notable recent efforts in this area have been the 1992 Lead Experiment (LeadEx Group 1993) and several projects as part of the 1997–98 Surface Heat Balance of the Arctic Ocean (SHEBA) program. However, in these situations the fixed sensor method of measuring boundary layer conditions is limited because it does not resolve horizontal variability, and it cannot be used under some types of surfaces [e.g., thin ice and open water]. In order to overcome these difficulties Morison and McPhee (1998, hereafter

Corresponding author address: James H. Morison, Applied Physics Laboratory, 1013 NE 40th St., Seattle, WA 98105.
E-mail: morison@apl.washington.edu

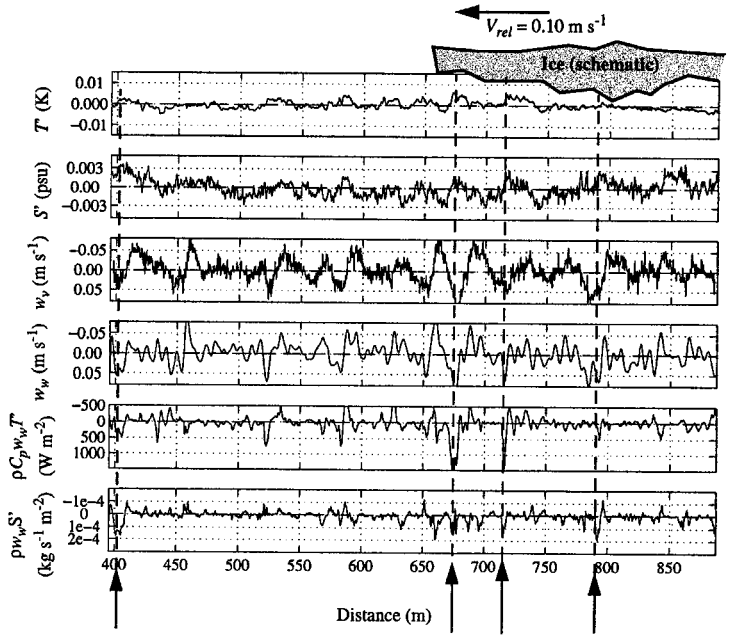

FIG. 1. ACTV data from lead 3, run 4, leg 3 of LeadEx. Mean vehicle depth was 15 m, speed was 1.65 m s^{-1}, and the mean ice–ocean relative velocity was 0.10 m s^{-1}. The data have been smoothed with a 1-m bin average, except for differentiated vehicle depth (w_v), which has been smoothed by a 5-m bin. Vertical water velocity, w_w, is estimated using a Kalman smoother on vehicle depth. See text. Several warm, salty downcurrents are indicated. The mean heat flux is 54 W m^{-2}, and the mean salt flux is 1.1 × 10^{-5} kg s^{-1} m^{-2}, positive downward. Correlation coefficients between vertical water velocity and temperature and velocity and salinity are significant at 0.23 for both.

MM98) combined measurements from the autonomous conductivity temperature vehicle (ACTV) and TICs to examine unstable haline convection from winter leads during LeadEx. The ACTV is a small, near-neutrally buoyant autonomous underwater vehicle (AUV) that travels a programmed course beneath leads and sea ice. It measures temperature and salinity with an onboard conductivity–temperature–depth (CTD) meter. MM98 found that the small rates of change of ACTV depth during a programmed level cruise appeared to be correlated with fluctuations in salinity. This is illustrated in Fig. 1 showing a sample of data from the ACTV taken during LeadEx. The panel labeled w_v is the vertical velocity of the ACTV inferred from vehicle depth. Many of the downward peaks in w are correlated with positive peaks in the salinity variation, S'. This suggests the vehicle moves downward with the saline, convective plumes. The vehicle acts roughly like a Lagrangian drifter with respect to small vertical motions, even while it moves horizontally at 1.7 m s^{-1}. Such observations led to the idea that vehicle motion could be used to estimate vertical water velocity. An ad hoc low-pass filter was used by MM98 to improve the agreement between the ACTV-derived vertical velocity and the vertical velocity spectra measured by the fixed TIC. The resulting ACTV velocity estimates were combined with the vehicle temperature and salinity measurements to directly derive horizontal profiles of the instantaneous local salt and heat fluxes, $w_w S'$ and $w_w T'$. Suitable profile averages of these agreed with estimates of fluxes made by other means and revealed among other things strong convective activity at the lead edges.

Other researchers have measured turbulent quantities with horizontally profiling instruments. Fleury and Lueck (1994) have used a shear probe on a towed vehicle to directly calculate heat and buoyancy flux on scales of 0.25–1 m. They noted that larger-scale motions that may have contributed significantly to the fluxes were contaminated by body motions. Levine and Lueck (1999) have used a shear probe on an AUV to estimate the rate of dissipation of kinetic energy along a horizontal track. Submarines have also been used by Yamazaki and Osborn (1993) to gather horizontal profiles of turbulent quantities using a shear probe. They calculated turbulent fluxes directly to validate eddy diffusivity models used by indirect techniques of estimat-

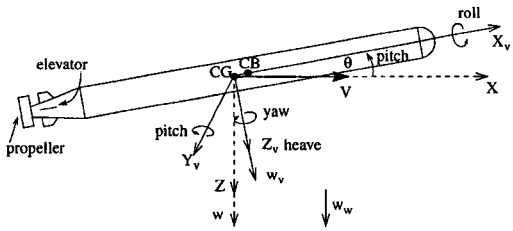

FIG. 2. ACTV schematic and both vehicle-centered and earth-centered (inertial) reference frames. The Y_v axis extends out of the page, and downward is positive in both frames. The velocity, V, is assumed known and constant. The center of gravity (CG) and center of buoyancy (CB) are indicated.

ing heat flux. However none of these efforts, besides MM98, have attempted to make direct measurement of the turbulent fluxes in the boundary layer.

The MM98 method of estimating turbulent velocity and fluxes with the ACTV data produced solid results, but it is limited. An AUV has its own dynamic response to variable vertical water velocity, especially since it has a control system that returns it to a programmed run depth. In MM98 this is accounted for partially by the ad hoc filter. However, this method is not founded on a knowledge of the AUV's dynamics. Different AUVs will behave differently in a turbulent velocity field. Thus, the ad hoc filter method is not a general solution that could be applied in other areas with confidence without TIC measurements for comparison. Here we will describe a Kalman smoothing method for deriving vertical water velocity from the motion of an AUV. The Kalman smoothing technique uses a model of vehicle dynamics to make optimum estimates of vertical water velocity from measurements of vehicle motion. It will also be shown that these velocity estimates can be used to directly compute horizontal profiles of $w_w S'$ and $w_w T'$.

Section 2 describes two AUVs and their dynamic models, the estimation technique, and the technique's performance. The technique is illustrated in section 3 by calculating turbulent fluxes of heat and salt for both Arctic and Antarctic case studies and comparing AUV and fixed turbulence mast data. Section 4 presents a brief summary. Details on vehicle models and the Kalman smoother are left to the appendixes.

2. Methods

a. Instrumentation

The Kalman smoothing method has been applied to two AUVs, the ACTV and the more sophisticated autonomous microconductivity temperature vehicle (AMTV). A schematic of the ACTV is shown in Fig. 2. The vehicle is about 1.6 m long and 9 cm in diameter, with a mass of 9.6 kg. It travels a preprogrammed, dead-reckoned course at about 1.7 m s^{-1}, measuring temperature, conductivity, and pressure. Horizontal position is recorded with an acoustic tracking system. The ACTV is described more fully by MM98. In MM98, TIC measurements of vertical water velocity are compared to the vertical velocity of the ACTV under the lead. This comparison relies on the assumption that the turbulent features may be treated as if they are frozen into the mean field and drift past the TIC at the mean flow speed (Taylor's hypothesis). This allows the time series observations of the TIC to be converted to spatial observations comparable to those made by the AUV. Spectra of TIC temperature and salinity converted to the spatial dimension in this way agree very well with the ACTV observations, confirming the applicability of Taylor's hypothesis. This method of comparison will be used here to validate the Kalman smoothing results. Samples of ACTV data from the LeadEx experiment and the 1994 Antarctic Zone Flux Experiment (ANZFLUX) experiment will be used to illustrate the Kalman smoother method.

A second vehicle, the AMTV, has been developed to take greater advantage of the Kalman smoothing scheme. It is based on the remotely operated underwater measurement system (REMUS) vehicle developed at the Woods Hole Oceanographic Institution. To more accurately estimate vehicle motion, the AMTV carries a precision Paroscientific pressure sensor and a Systron Donner Motion Pack package of accelerometers and sensitive pitch, roll, and yaw rate sensors. Of the motion pack sensors, we only use output of the forward accelerometer and pitch rate sensor in the Kalman smoother calculations. Of course the accelerometer signal is due to both acceleration of the vehicle and the effect of gravity at the pitch angle of the vehicle. For the range of vehicle motions studied here the acceleration component of the signal is less than 1% of the gravity-induced pitch angle signal. Therefore the accelerometer output is taken as a measure of pitch angle.

The AMTV employs fast-response Sea-Bird Electronics, SBE 7-02 microconductivity and SBE 7-01 microtemperature probes, as well as an upward-looking Tritech precision acoustic altimeter to measure ice draft. The AMTV is 1.6 m in length, 19 cm in diameter, and displaces 33 kg (Fig. 3). Pairs of elevator planes and rudder planes at the tail control its motion. It operates at speeds from 1.0 to 1.6 m s^{-1} under program control. Like the ACTV, a three-dimensional course is programmed into the AMTV. This may be a combination of dead-reckoning, acoustic navigation, and homing to one of two Benthos acoustic transponders. The two-dimensional position of the AMTV is displayed and recorded by 100-m baseline portable acoustic tracking range developed at the Applied Physics Laboratory (APL). The AMTV has the capability to home in on acoustic beacons, either to reach a desired checkpoint during a run, or to be recovered in a submerged panel of netting. AMTV data from the SHEBA summer lead experiment will be used to illustrate the performance of the Kalman

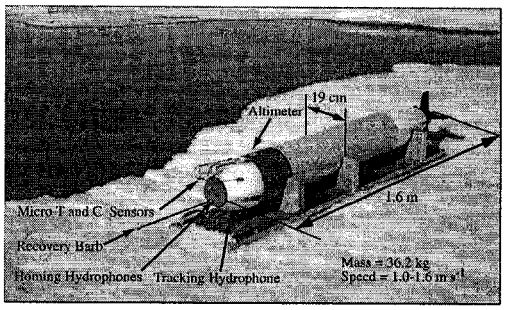

FIG. 3. The AMTV at SHEBA experiment site, Aug 1998. Specifications and vehicle components are indicated in the figure.

smoother for a vehicle in a unique setting incorporating more motion sensors.

b. Kalman smoothing

The Kalman smoother makes an estimate of system state that is an optimum combination of a dynamic model–based extrapolation and noisy measurements of a few components of the state (Gelb 1974). The smoother is founded on a linear state–space representation of the dynamic system being studied. That is, the system evolution is determined by multiple first-order differential equations for the rate of change of a vector of state variables. In our case, the position and velocity of an AUV at one time, along with the equations of motion allow us to predict its position and velocity at any later time. The motion of the vehicle is predicted from the sum of the forces acting on it, including buoyancy, the action of water flowing by it vertically, and forces exerted by the control surfaces. Because forces on the vehicle and measurements have random parts, the system model must include a random forcing function for vertical water velocity and an estimate of sensor noise to completely specify the system. The smoother uses the vehicle model and noisy observations to produce an optimal estimate of the true, unobservable state of the system. In other words, the smoother will estimate the portion of the system variability due to unforced motion of the body and due to noise. The vehicle forcing (vertical water velocity) is calculated to account for what remains of the measured variability.

In application, the Kalman smoother consists of two recursive filters that are run forward and backward over the vehicle data. Thus a smoother may only be applied after all data have been collected. For the sake of clarity and concreteness the simpler forward Kalman filter is presented here. The smoother is developed from the filter paradigm in appendix A. The filter is based on a system model (1), a measurement model (2), and initial conditions for the state vector (3):

$$\frac{d}{dt}\mathbf{x} = \mathbf{F}\mathbf{x} + \mathbf{G}\mathbf{v} \qquad \mathbf{v} \sim \text{Normal}(0, \mathbf{Q}) \tag{1}$$

$$\mathbf{z} = \mathbf{H}\mathbf{x} + \mathbf{n} \qquad \mathbf{n} \sim \text{Normal}(0, \mathbf{R}) \tag{2}$$

$$\mathbf{x} = \begin{bmatrix} w_w \\ w \\ q \\ z \\ \theta \end{bmatrix} = \begin{bmatrix} \text{vertical water velocity} \\ \text{vertical vehicle velocity} \\ \text{pitch rate} \\ \text{vehicle depth} \\ \text{vehicle pitch} \end{bmatrix}. \tag{3}$$

The system model is a first-order matrix differential equation for the vector of state variables, $\mathbf{x}$. The variables w, q, z, and θ are vehicle variables related to each other by the equations of vertical and pitching motion. The vertical water velocity, w_w, is inserted into the system model, so that it can be estimated directly by the Kalman technique. The first term on the right of (1) represents the system dynamics. Deterministic control inputs, which in our case are functions of the state vector, are subsumed into the dynamics term. The second term is the stochastic function representing the system forcing, which is assumed to be distributed normally with mean zero and noise covariance matrix $\mathbf{Q}$. The measurement vector, $\mathbf{z}$, is modeled in (2) as a combination of the true-state variables plus a normally distributed noise vector with zero mean and covariance matrix $\mathbf{R}$. In general, $\mathbf{F}$, $\mathbf{G}$, and $\mathbf{H}$ may be functions of time, but here they are constant. All vectors have zero mean.

The forward Kalman filter seeks an estimate of the state vector just after the measurement as an optimum linear combination of the state vector just before the measurement and the measurement vector itself. The unknown coefficient matrices for the linear combination are found by requiring that the error in the estimate is unbiased, then forming the matrix of error covariances and minimizing the trace of this matrix. See Gelb (1974, chapter 4) for a complete derivation. The filter consists of the following system of equations describing the evolution of the state estimate, $\mathbf{x}_f$, and the error covariance, $\mathbf{P}_f$ (Gelb 1974, p. 123). Subscripts indicate an estimate (forward in this case), and true but unknown values of $\mathbf{x}$ have no subscripts:

$$\frac{d\mathbf{x}_f}{dt} = \mathbf{F}\mathbf{x}_f + \mathbf{P}_f\mathbf{H}^T\mathbf{R}^{-1}[\mathbf{z} - \mathbf{H}\mathbf{x}_f]$$

$$\mathbf{x}_f(t = 0) = \mathbf{x}_0 \tag{4}$$

$$\frac{d\mathbf{P}_f}{dt} = \mathbf{F}\mathbf{P}_f + \mathbf{P}_f\mathbf{F}^T + \mathbf{G}\mathbf{Q}\mathbf{G}^T - \mathbf{P}_f\mathbf{H}^T\mathbf{R}^{-1}\mathbf{H}\mathbf{P}_f$$

$$\mathbf{P}_f(t = 0) = \mathbf{P}_0, \tag{5}$$

where $\mathbf{P}_f \equiv E[(\mathbf{x}_f - \mathbf{x})(\mathbf{x}_f - \mathbf{x})^T]$.

It is assumed that the random forcing, $\mathbf{v}$, and measurement noise, $\mathbf{n}$, are uncorrelated and that $\mathbf{R}^{-1}$ exists (nonzero measurement noise). Given a vector of measurements, $\mathbf{z}$, the initial value problem can easily be

solved numerically for **x** and **P** using a prepackaged ordinary differential equation (ODE) solver. The appendix A linear filter is *the* optimum filter if both system and measurement noise are truly Gaussian. If they are not, the filter is only the optimum *linear* filter (Gelb 1974, p. 107). Intuitively, the forward estimate obeys the deterministic model, **F**, when the measurement errors (**R**) are large compared to the difference between the estimated and measured state, that is, the measurements are of little value to the estimate. The vertical water velocity estimate is simply the first element of the state estimate.

A considerable portion of effort in deriving a Kalman filter is in deriving the system model **F**. This is discussed in detail for our vehicles in appendix B, but a brief summary is given here.

c. *Linearized model for autonomous underwater vehicles*

Bartlett and Schlachter (1967) and Nahon (1996) derive the complete set of equations of motion for torpedo-shaped bodies. These are for vehicle motion in still water. Here a simplified model is used for small vehicle motions in the vertical plane due to the action of vertical water velocity variations. The model is a linearized, two-dimensional system of equations. The vertical and angular motions (heave and pitch) of an underwater vehicle are best expressed in a body-centered reference frame, with the vehicle center of gravity as the origin (Etkin 1972). The oceanic boundary layer dynamics are naturally described in an earth-centered coordinate system. The vehicle- and earth-centered coordinate systems are illustrated in Fig. 2. In our initial derivations the water velocity is assumed constant over the length of the vehicle. (In a final refinement we modify this assumption.) The vehicle control system is assumed to be active, but it only attempts to constrain the vehicle to a constant run depth. The pitch (θ) and elevator deflection (δp) angles are assumed small. The equations in the vehicle-centered frame are further simplified by assuming the roll angle, roll rate, and yaw rate are zero. Vehicle horizontal velocity is assumed constant. Vehicle run data during straight and level flight analyzed here support these assumptions. The simplified equations of motion for vertical vehicle velocity (w_v) and pitch rate (q), are

$$m_T\dot{w}_v = Z_{w_v}w_{v\text{rel}} + (Z_q + m_L V)q + Z_{\text{dp}}\delta\text{p} + (mg - B) \quad (6)$$

$$J_y\dot{q} = M_{w_v}w_{v\text{rel}} + M_q q + M_{\text{dp}}\delta\text{p} + BX_{\text{CB}}. \quad (7)$$

In Eq. (6), w_v is the vertical acceleration of the AUV in the vehicle-centered coordinate system, $w_{v\text{rel}}$ is the velocity of the AUV relative to the water in the vehicle-coordinate system, q and $\dot{q}$ are the pitch rate and pitch angular acceleration, and δp is the dive plane angle relative to the vehicle. The vehicle mass is m. The apparent longitudinal and transverse masses are represented by m_L and m_T, respectively. The apparent moment of inertia is J_y. The apparent mass (inertia) terms include the mass (inertia) plus the virtual mass (inertia) that arises because the fluid that surrounds an accelerating vehicle must also be accelerated. The body force of net buoyancy ($mg - B$) and the pitching moment due to a separation of the center of gravity and the center of buoyancy (Bx_{CB}) are the constant terms in (6) and (7). One Coriolis term arises, $m_L Vq$. All other nonconstant terms on the right-hand side are the hydrodynamic forces and moments arising from the motion of the vehicle relative to the water. These forces and moments are written as state variables multiplied by subscripted Z or M coefficients derived in appendix B. The force and moment coefficients are constant, since the vehicle travels at a constant speed, V. A complete list of symbol definitions is in appendix C.

Since both the depth and water velocity are referenced to true vertical, the equations of motion need to be expressed in the earth-centered reference frame. With vertical water velocity, w_w, defined positive downward and assumed uniform across the vehicle, referring to Fig. 2, and assuming the pitch angle, θ, is small, the following transformation expresses w_v and $w_{v\text{rel}}$ in terms of the earth-centered vehicle vertical velocity, w, and water velocity, w_w:

$$w_v \approx w + V\theta \quad \text{and}$$

$$w_{v\text{rel}} = w_v - w_w\cos\theta \approx w + V\theta - w_w. \quad (8)$$

The hydrodynamic forces on the dive planes associated with the controlled deflection of planes appears as $Z_{\text{dp}}\delta$p and $M_{\text{dp}}\delta$p in (6) and (7). [The hydrodynamic forces on the planes associated with vehicle angle of attack are subsumed along with hydrodynamic forces on other parts of the vehicle in the first two terms on the right sides of (6) and (7)]. The ACTV control law states the dive plane angle at a given time is proportional to the present depth and pitch errors:

$$\delta\text{p} = K_{\theta\text{p}}(\theta - \theta_{\text{goal}}) \quad (9)$$

where

$$\theta_{\text{goal}} = K_{z\text{p}}(z - z_{\text{goal}}).$$

After incorporating the transformation (8) and the control law (9), the system with forcing may be expressed as a single linear matrix differential equation:

$$\frac{d\mathbf{x}}{dt} = \mathbf{F}\mathbf{x} + \mathbf{D}_1 + \mathbf{D}_2 + \mathbf{G}\mathbf{v}, \quad (10)$$

where

$$\mathbf{F} = \begin{bmatrix} 0 & 0 & 0 & 0 & 0 \\ \dfrac{-Z_w}{m_T} & \dfrac{Z_w}{m_T} & \dfrac{Z_q + (m_L - m_T)V}{m_T} & \dfrac{-K_{zp}K_{\theta p}Z_{dp}}{m_T} & \dfrac{VZ_w + K_{\theta p}Z_{dp}}{m_T} \\ \dfrac{-M_w}{J_Y} & \dfrac{M_w}{J_Y} & \dfrac{M_q}{J_y} & \dfrac{-K_{zp}K_{\theta p}M_{dp}}{J_y} & \dfrac{VM_w + K_{\theta p}M_{dp}}{J_y} \\ 0 & 1 & 0 & 0 & 0 \\ 0 & 0 & 1 & 0 & 0 \end{bmatrix} \quad \text{and} \tag{11}$$

$$\mathbf{D}_1 = \begin{bmatrix} 0 \\ \dfrac{(mg - B)}{m_T} \\ \dfrac{BX_{CB}}{J_y} \\ 0 \\ 0 \end{bmatrix} \qquad \mathbf{D}_2 = K_{zp}K_{\theta p}z_{goal}\begin{bmatrix} 0 \\ \dfrac{Z_{dp}}{m_T} \\ \dfrac{M_{dp}}{J_y} \\ 0 \\ 0 \end{bmatrix} \qquad \mathbf{G} = \mathbf{I}_5. \tag{12}$$

Equation (10) takes the form of (1) if the steady-state solution $\mathbf{x}_{ss}$ is subtracted, where $\mathbf{F}\mathbf{x}_{ss} + \mathbf{D}_1 + \mathbf{D}_2 = 0$. Thus in the development of the smoother the system matrix $\mathbf{F}$ of Eq. (11) is used. The lift and moment coefficients in $\mathbf{F}$ are derived in appendix B.

The equations of motion for the AMTV are basically the same as for the ACTV, but in place of a simple proportional control system, the AMTV uses a proportional-plus-integral (PI) control system. This requires the addition of two state variables to the linear system to track the integrated depth error and integrated pitch error. The integrated errors are not computed from observations, but rather estimated and used by the filter. The AMTV state vector is

$$\mathbf{x} = \begin{bmatrix} w_w \\ w \\ q \\ z \\ \theta \\ z_{errint} \\ \theta_{errint} \end{bmatrix} = \begin{bmatrix} \text{vertical water velocity} \\ \text{vertical vehicle velocity} \\ \text{pitch rate} \\ \text{vehicle depth} \\ \text{vehicle pitch} \\ \text{integrated depth error} \\ \text{integrated pitch error} \end{bmatrix}. \tag{13}$$

It is a simple exercise to modify $\mathbf{F}$ to incorporate the following PI control system (appendix B):

$$\delta p = K_{\theta p}\theta_{err} + K_{\theta i}\theta_{errint} \tag{14}$$

$$\theta_{err} = \theta - (K_{zp}z_{err} + K_{zi}z_{errint}) \tag{15}$$

$$\theta_{errint} = \int_0^t \theta_{err}(\alpha)\, d\alpha \tag{16}$$

$$z_{err} = z - z_{goal} \tag{17}$$

$$z_{errint} = \int_0^t z_{err}(\alpha)\, d\alpha. \tag{18}$$

Besides a seven-element state vector, the AMTV model differs slightly from the ACTV model due to the physical differences in mass, size, and control surfaces. The hydrodynamic coefficients for each vehicle are derived in appendix B.

d. System noise measurement parameters

It remains to specify $\mathbf{G}$, $\mathbf{H}$, $\mathbf{Q}$, and $\mathbf{R}$, as well as initial conditions for the state vector and $\mathbf{P}$. The choice of forcing and observed variables specifies $\mathbf{G}$ and $\mathbf{H}$, which are matrices of ones and zeros. The initial state vector is chosen to be the zero vector, because the smoother uses an unbiased-state vector. As discussed above, the equation for the steady state can be subtracted from the equation of motion to produce the unbiased vector and equation in the form of Eq. (1).

The choice of $\mathbf{Q}$ and $\mathbf{R}$ is a long-standing problem in Kalman smoothing. A diagonal matrix $\mathbf{R}$ consists of the variance of noise evident on the various measurement records multiplied by the time interval between measurements. This formulation of the noise arises as part of the derivation of the continuous Kalman filter from the discrete filter, which propagates variance. A discrete, purely random process with variance equaling σ_z^2 divided by the time step approximates the continuous white noise process of variance σ_z^2 in the limit of time step approaching zero (Gelb 1974, p. 121). To understand this, each discrete measurement can be viewed as an average of the continuous white noise process over the time interval. The variance of the average is the variance of the white noise process divided by the av-

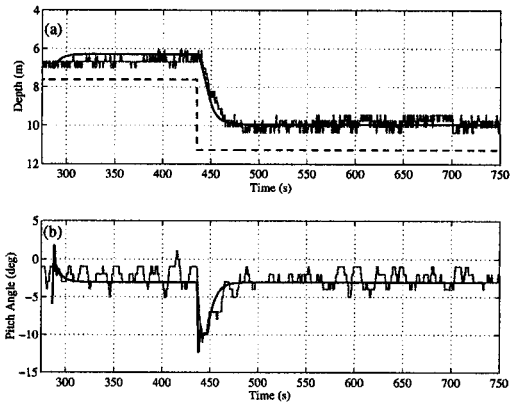

FIG. 4. Observed and simulated (a) depth and (b) pitch for the ACTV during a commanded depth change. The goal depth is indicated by the dashed line. The gray line indicates observed data. Because the dive plane angle is directly proportional to the depth error, and the vehicle is buoyant, it runs at a depth slightly offset from the goal. This run took place at lead 3 of LeadEx on 7 Apr 1992.

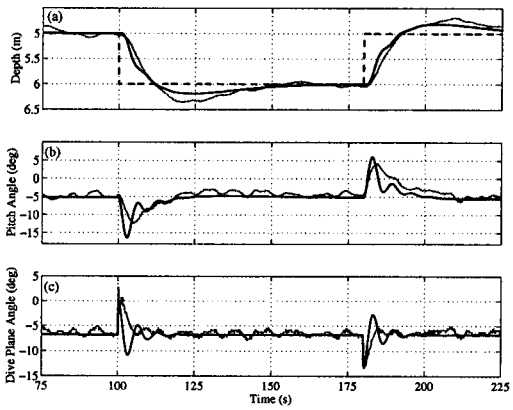

FIG. 5. Observed and simulated (a) depth, (b) pitch, and (c) dive plane angle for the AMTV during a commanded depth change for run 3 at SHEBA on 7 Aug 1998. The dashed line is the goal depth, and the gray line indicates observed data. The modeled dive plane angle has been offset by 3.5°, to match the observed value, which is difficult to calibrate to this accuracy.

eraging interval (Jenkins and Watts 1968, p. 159). Therefore, the variance of the measurement noise is multiplied by the time step to get the corresponding variance of the idealized continuous measurement noise, **R**. For the ACTV, only depth is measured so that **R** is a scalar. The AMTV measurements include pitch rate, depth, and pitch, so **R** is a 3 × 3 diagonal matrix.

The diagonal matrix **Q** represents the random noise on the state vector. The vertical water velocity has random noise, but the only noise on the other state variables is due to the water velocity through the state equation. Therefore, elements of **Q** are set at 10^{-10} except for $Q_{1,1}$, which is estimated from the variance of vertical water velocity measured independently by a turbulence mast when possible, or from the vertical velocity of the vehicle when necessary. The estimation of $Q_{1,1}$ from measurements of water velocity must be approached through the conversion process between discrete and continuous state models (Gelb 1974, 66–77). In the continuous model, the rate of change of the state is forced by the continuous white noise process, **v** [Eq. (1)]. In the analogous discrete equation, the state itself is forced by a discrete process, which corresponds to the integral of the continuous forcing, **v**, over the time step. The variance of the discrete forcing is just $\mathbf{Q}_k = \text{var}(\mathbf{v}_k)$. Taking the same variance expectation of the integral form and letting the time step approach zero gives $\mathbf{Q}_k = \text{dt} \times \text{var}[\mathbf{v}(t)] = \text{dt} \times \mathbf{Q}$ to first order. As a net result, $Q_{1,1}$ is equal to the variance in measured (discrete) water velocity divided by the filter time step.

The choice of $\mathbf{P}_0$ and derivation of $\mathbf{P}_f$ are done in the process of filtering. For a time-invariant system such as this, $\mathbf{P}_f$ tends to a steady-state value (Gelb 1974, p. 142). Here we integrate (4) and (5) using an ODE solver with an arbitrary $\mathbf{P}_0$ until a steady-state $\mathbf{P}_f$ is found, then restart with the new value of $\mathbf{P}_0$ equal to the steady-state $\mathbf{P}_f$.

e. Model and smoother tests

The vehicle system models were first tested by comparing simulations against measured responses to commanded step changes in run depth. Figure 4 shows such a comparison for ACTV depth and pitch, using the model of Eqs. (6)–(12). In this paper, depth and velocity are positive downward. The run data were obtained from LeadEx on 7 April 1992. Besides a start-up transient in the model, the depth and pitch are modeled well through both the commanded depth change and in steady state.

The analogous test of the AMTV model (Fig. 5) shows agreement between the modeled and actual depth, pitch, and dive plane angle. These run data were obtained at ice station SHEBA on 7 August 1998. On average the simulated and actual run depths agree well, though the depth response of the model to step change depth commands is slightly faster than the actual vehicle response initially and then tends to undershoot slightly. It should be noted that in applying the Kalman technique, only portions of a run where the vehicle was running straight and level will be analyzed. Depth excursions during these segments are much smaller than the commanded depth changes. Thus, the step responses of Figs. 4 and 5 are extreme tests and may force the model beyond the region where the linearized model is strictly appropriate. The model is likely to be more accurate for smaller deviations from steady state.

We investigate the extent to which the ACTV moves with the water by forcing the vehicle model with a time series of actual vertical velocity measured by a TIC at LeadEx. To force the model, the TIC data are translated

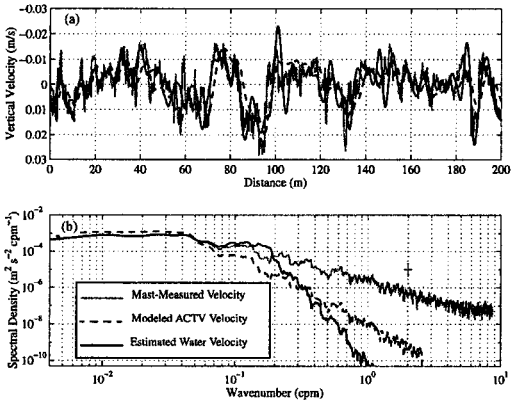

FIG. 6. (a) The vertical water velocity measured by a turbulence frame at lead 3 of LeadEx (gray line) was used to force the model ACTV, whose vertical velocity is plotted (dashed line). Shown with a black line is the Kalman smoother estimate of vertical water velocity, based only on the depth of the model ACTV plus Gaussian noise. (b) The wavenumber spectra of the series show the vehicle roughly follows vertical water velocity at scales greater than 15 m, and the smoother estimate agrees with the original forcing at all wavenumbers below 0.2 cpm (scales greater than 5 m). The spectra were calculated using the multitaper method with NW = 6 and by averaging the first 6 eigenspectra. The length of the 95% confidence interval and resolution bandwidth are shown as a criss-cross in the upper right (as in Percival and Walden 1993, p. 343).

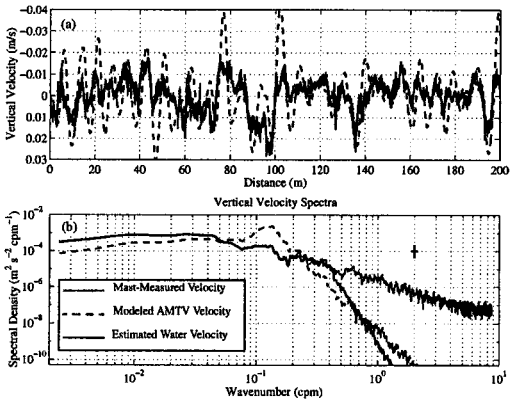

FIG. 7. Same as Fig. 6, except for the AMTV. Note the spectrum of the smoother estimate of vertical water velocity agrees with that of the forcing velocity at all wavenumbers below 0.4 cpm.

from a measurement in time to a measurement in space using Taylor's hypothesis. We then model the ACTV traveling through this turbulent field. The vertical water velocity (solid gray) and modeled vertical ACTV velocity (dashed) are shown in Fig. 6a, and Fig. 6b shows their wavenumber spectra. The simulated vertical velocity of the ACTV roughly agrees with the water velocity. This supports the idea of MM98 that the ACTV tends to track vertical water motion at the scales of boundary layer turbulence. Besides rolling off at a high wavenumber, the modeled vehicle velocity also is affected by the control system at low wavenumbers, but at the low frequencies involved, the effect on vertical velocity is small.

To test the Kalman smoothing algorithm and demonstrate that it improves estimates of vertical water velocity, the vehicle data simulated above are complimented with artificial noise and used as smoother input to recreate the forcing function. This recreation is then compared with the water velocity record that forced the model. For the ACTV test the modeled vehicle depth is used, and to it Gaussian noise is added to resemble the ACTV pressure sensor noise. Here **R** is the variance of this noise multiplied by the time interval, and is given in Table 1. The smoother uses this artificial depth measurement in the smoothing algorithm [Eqs. (4), (5), (A4), (A5)] to estimate vertical water velocity. The variance of the water velocity forcing, $Q_{1,1}$, is set based on the water velocity forcing the model and is also in Table 1. In Fig. 6 the Kalman smoother estimate of the water velocity (solid black) is compared to the water velocity that forced the model (solid gray). The smoother recovers the water velocity from the modeled vehicle depth out to a wavenumber of about 0.2 cycles per meter (cpm), or a 5-m wavelength.

The identical procedure was carried out with the AMTV model. The smoother was applied to the depth simulated by the AMTV model, and the resulting water velocity estimate is plotted in Fig. 7. See Table 1 for smoother parameters. The larger AMTV did not follow the water velocity as closely as the ACTV (Fig. 7a). However, when the smoother is used, the more accurate pressure sensor of the AMTV compensates for this and the forcing signal is recovered more accurately. The spectra of the true and estimated vertical water velocity (Fig. 7b) agree down to a wavelength of less than 3 m

TABLE 1. Kalman smoother parameters for three test cases: variance of measurement noise (**R**) and variance of vertical water velocity (**Q**).

	ACTV Figs. 6, 9–13	AMTV 1 Fig. 7	AMTV 2 Figs. 8, 14–16
$\mathbf{R}$ = dt*diag(σ_i^2) dt ~ 0.12 sec	$\sigma_z^2 = (0.015\ \text{m})^2$	$\sigma_z^2 = (0.005\ \text{m})^2$	$\sigma_a^2 = (0.1\ \text{deg s}^{-1})^2$ $\sigma_z^2 = (0.005\ \text{m})^2$ $\sigma_\theta^2 = (0.1\ \text{deg})^2$
$Q_{1,1} = \text{dt}^{-1}*\sigma_{ww}^2$ (m² s⁻³)	6×10^{-4}	3×10^{-4}	3×10^{-4}

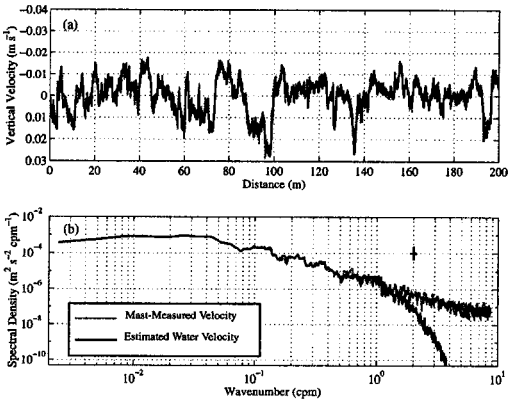

FIG. 8. As in Figs. 6 and 7. Vertical water velocity estimated from the modeled depth, pitch, and pitch rate of AMTV. Modeled vehicle velocity is identical to that in Fig. 7, and is not shown here. Prior to smoothing, Gaussian noise sequences were added to each observed variable. More observed variables results in a better water velocity estimate, whose spectrum agrees with the original forcing function spectrum at all wavenumbers below about 2 cpm.

(wavenumbers below 0.4 cpm). The improvement is over the range of wavenumbers where vehicle dynamics are expected to cause the vehicle velocity to deviate from the water velocity. The oscillatory roots of Eq. (10) for the AMTV (the complex eigenvalues of **F**) correspond to periods of 6.5 and 140 s, or assuming a vehicle velocity of 1.1 m s^{-1}, wavenumbers of 0.14 and 0.0065 cpm. The former root is dominant and is likely responsible for the peak in the vehicle velocity spectrum above 0.1 cpm. The smoother corrects for the vehicle motion at this wavenumber, resulting in an accurate estimation of the forcing function.

The AMTV smoother test was repeated using the simulated vehicle pitch rate, pitch, and depth, rather than only depth. Noise was added to each before going into the smoother. Figure 8 shows improvement in the vertical water velocity estimate for higher wavenumbers. The smoother-derived vertical velocity agrees with the true forcing out to almost 2.0 cpm (Fig. 8b).

It is important to realize that the real vehicle will not respond as the model responds to fluctuations of wavelength smaller than about 1.6 m. For both the ACTV and AMTV models, the water velocity is assumed uniform over the length of the vehicle. In practice, for variations in w_w at wavelengths much less than the hull length, the net effect on vertical motion of the vehicle is small. Vehicle motion at wavelengths near the hull length may be strongly affected by horizontal gradients in velocity. MM98 suggested that this may result in a gradient-pitching phenomenon that would amplify the vehicle response. As the vehicle moves into a region of rapidly increasing w_w (positive down) the front of the vehicle is affected first, and the vehicle will pitch down so as to amplify the depth response.

As will be discussed, the gradient-pitching phenomenon appears to be detectable in the AMTV data. Therefore an effort has been made to account for the horizontal gradient of w_w over the length of the vehicle. Our method is to include horizontal variability in the equation of the system state. The state vector [Eq. (13)] and the corresponding system matrix, **F**, are modified so that w_w is replaced by w_f, the water velocity acting on the front of the vehicle, and w_b, the water velocity acting on the back of the vehicle. The velocity w_b is a lagged version of w_f approximated by a first-order process with time-constant τ driven by w_f that is forced by white noise. The time domain w_b for a single step in w_f is

$$w_b(t) = 1.58 w_f(t_i)\left\{1 - \exp\left[-\left(\frac{t - t_i}{\tau}\right)\right]\right\}. \quad (19)$$

The proportionality constant is set so that for a step change in w_f, the amplitude of the velocity at the back of the vehicle, w_b, at time $(t_i + \tau)$ is equal to the velocity at the front of the vehicle at time t_i. The value of τ is set to 1.5 s, about the time it takes for the AMTV to travel its own hull length. The vertical water velocity estimate is for w_f. Details are left to appendix B.

3. Field test results

To illustrate the utility of the Kalman smoothing method, we have used it to analyze ACTV and AMTV data from three experiments, LeadEx, ANZFLUX, and SHEBA.

a. Arctic Lead Experiment (LeadEx)

During LeadEx the ACTV made horizontal profiles of conductivity, temperature, and depth under newly formed leads in the sea ice (LeadEx Group 1993; MM98). Instrument huts were flown to leads near a central camp, which was initially at 72°47′N, 144°W on 12 March 1992. The data were taken under and around these rapidly freezing gaps in the pack ice. Upon contact with the cold air, the seawater begins to freeze, rejecting salt, and eventually releasing dense, high salinity water (Wettlaufer et al. 2000). This results in free convection when ice velocities are low and forced convection if ice velocities are high. The data in this section were taken at lead 3: a wide (1000 m) lead with a reasonably high ice–water-relative velocity of 0.11–0.13 m s^{-1}. A TIC mast was fixed to the ice at the downstream edge of the lead and under these conditions provided reliable turbulence data with which to compare the Kalman smoother results.

The sample of vehicle data shown in Fig. 1 was gathered during run 4 at lead 3. The ACTV was traveling 1.7 m s^{-1} at about 15-m depth during this run and collecting data at 9 Hz. Detrended temperature, T', and salinity S', have been smoothed with a 1-m horizontal bin average. Vertical vehicle velocity in the third panel

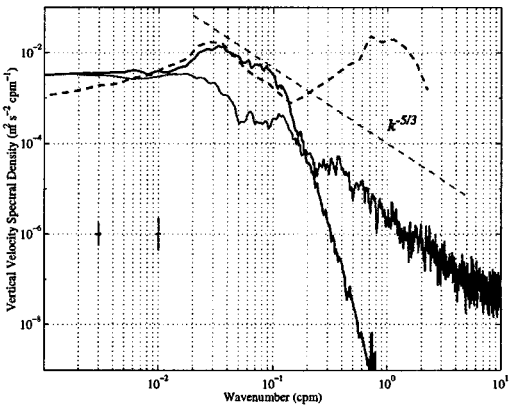

FIG. 9. Vertical velocity spectra from lead 3, run 4 of LeadEx. The smoothed average of vertical vehicle velocity spectra from ACTV leg 2 and leg 3 is shown as a dashed black line, while the average of the vertical water velocity spectra from the same 2 legs calculated by the Kalman smoother is the solid black line. The solid gray line represents the spectrum from the turbulence mast. Both instruments were taking data simultaneously: the ACTV at 15-m and the mast at 14-m depth. The ACTV was in the lead during leg 2 and half of leg 3, while the mast was at the downstream edge of the lead. A 95% confidence interval for the mast spectrum is the gray vertical bar, and the confidence interval for the vehicle-derived water velocity is the black vertical bar. A $k^{-5/3}$ line is also shown (dashed gray).

was calculated by differentiating the depth record and smoothing with a 5-m bin average. Vertical water velocity for the run has been calculated with the Kalman smoother using the vehicle model of Eqs. (9)–(12) and is shown in the fourth panel. Note the similarity to the vehicle velocity. The horizontal profiles of turbulent flux were calculated using w_w, S', T', and a mean density and heat capacity: $F_{heat} = \rho C_p w_w T'$ and $F_{salt} = \rho w_w S'$. These are shown in the fifth and sixth panels respectively. The sign convention for vertical water velocity, and therefore heat and salt flux, is positive downward. The vertical axes of the plots have been oriented accordingly. Turbulence frame measurements at 14-m depth during the same period of time included vertical water velocity, temperature, and salinity.

The wavenumber spectra of vertical velocity obtained from the TIC and from the Kalman smoothed ACTV data are compared in Fig. 9. The time series gathered by the TIC has been translated into a spatial series using the mean ice velocity (10 cm s^{-1}) and sampling frequency (0.5 Hz). The frame-derived vertical water velocity shows the wavenumber, k, rolls off with a slope of $k^{-5/3}$, indicative of the inertial subrange for turbulence. The vertical vehicle velocity spectra for the segments of run 4 under lead 3 are averaged and smoothed in Fig. 9 (dashed line). The average of the spectra of the water velocity for 2 segments of ACTV run 4 at lead 3 is also plotted (solid black line). Despite the aggressive filtering of high-frequency oscillations, spikes were evident in the smoothed water velocity spectrum at a fundamental wavenumber of 0.13 cpm and higher harmonics. The spikes every 4 s carried through from the raw depth record acquired by the vehicle and are due to the interference of the acoustic transducer. Peaks in the wavenumber spectra at the harmonics of the spike frequency were found to be significant with Thomson's F-test for periodicity (Percival and Walden 1993, 496–501). Because only the background spectrum is of interest and not the spectral peaks, the peaks have been removed.

The smoother-derived water velocity agrees with the turbulence frame at wavenumbers below 0.01 cpm and in the region around 0.2 cpm. The smoother is accounting for the control system at low wavenumbers, and for measurement noise at high wavenumbers. The smoother-derived energy is a factor of 9 higher than the TIC spectrum between 0.02 and 0.1 cpm. Similar bulges occur in every ACTV spectrum from LeadEx. A hump in filtered vehicle velocity around 0.03 cpm is also present in MM98 (their Fig. 9a). It is narrower, but about an order of magnitude above the frame levels. The peak is likely due to an unrecognized mode of vehicle motion that is not corrected for properly with the Kalman smoother. MM98 show that (their Fig. 9a) the vertical water velocity (filtered ACTV velocity) spectrum stays close to the frame spectrum at higher wavenumbers where the filter is active. In this, the ad hoc filter of MM98 does a slightly better job than the Kalman smoother because the MM98 filter was designed by matching ACTV and TIC spectra. The advantage of the Kalman smoother in this situation is that by being based only on an a priori derivation of the vehicle dynamics, its results are an independent description of the turbulent boundary layer. Therefore, in complex situations boundary layer features such as horizontal inhomogeneity are unlikely to be obscured by mechanistically constraining the AUV results to agree with the fixed sensors.

The smoother drastically reduces the energy in vehicle velocity above 0.25 cpm. The ACTV model used by the smoother has its only complex eigenvalue (or characteristic frequency) at 0.014 cpm, so at much higher wavenumbers, vehicle dynamics cannot account for large fluctuations in the vehicle velocity. The high-wavenumber energy in vehicle velocity is due to sensor noise that the smoother filters.

Even though the vertical water velocity spectrum is imperfect, the heat and salt fluxes estimated with the ACTV compare favorably with the TIC measurements. The heat and salt fluxes from the TIC and ACTV are not expected to be identical because of the episodic nature of the turbulence and because the TIC sampled at the lead edge while the ACTV sampled under and around the lead. However, as shown in Fig. 10, the spectra of heat and salt flux from the ACTV compare well to those of the TIC. The broad peak around 0.02 to 0.1 cpm in vertical water velocity has not carried through to the flux calculations. This is because the erroneous velocity fluctuations in this wavenumber

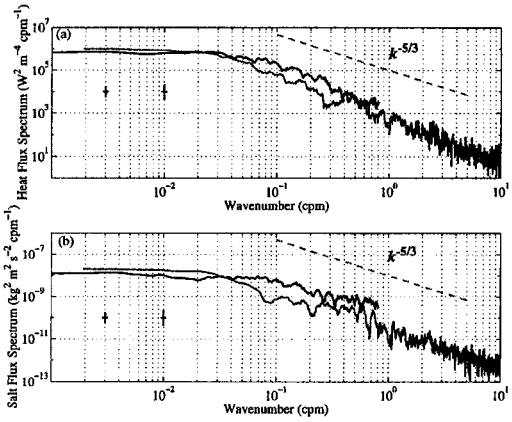

FIG. 10. As in Fig. 9, except for vertical (a) heat flux and (b) salt flux. The gray lines are the spectra for fluxes calculated using turbulence frame data. Each black line is the average of 2 ACTV flux spectra from the 2 segments of run 4 in the lead.

range are not coherent with temperature and salinity fluctuations. The average flux results are also gratifyingly similar. The heat flux averages for the ACTV (legs 2 and 3 of run 4 at lead 3) under the lead upstream of the TIC are 92 and 54 W m^{-2}. The TIC average over the same period is 78 W m^{-2}. Salt flux averages are 1.5 and 1.1 $\times$ 10^{-5} kg s^{-1} m^{-2} for the ACTV and 0.58 $\times$ 10^{-5} kg s^{-1} m^{-2} for the TIC. Temperature and salinity in both datasets are found to be significantly correlated with vertical water velocity by using the empirical probability distribution function for correlation at random lags as in MM98, Fleury and Lueck (1994), and Lueck and Wolk (1999). A correlation is considered significant if it is above the 2 standard deviation level for the distribution of correlation coefficients at random lags.

b. *Antarctic Zone Flux Experiment (ANZFLUX)*

The ANZFLUX experiment (McPhee et al. 1996) has provided the opportunity to test the Kalman smoother method with data from a different boundary layer regime. It took place during the southern winter of 1994. The goal of the experiment was to measure turbulent fluxes in the high heat flux region of the Weddell Sea. Two 6-day manned ice drift experiments were conducted. The ACTV was deployed during the second manned experiment over Maud Rise.

The relatively long run analyzed here (run 3) was carried out on 5 August 1994 (day 217) at 0917 local time. A storm caused ice velocities of up to 0.45 m s^{-1} late on day 216, while during the run early on day 217, the ice had slowed to 0.14 m s^{-1}. A box pattern at 50-m depth was run, and a lead was intersected midway through. The three-dimensional run track is shown in Fig. 11 with heat flux overlaid. The heat flux was estimated using the temperature fluctuations and Kalman

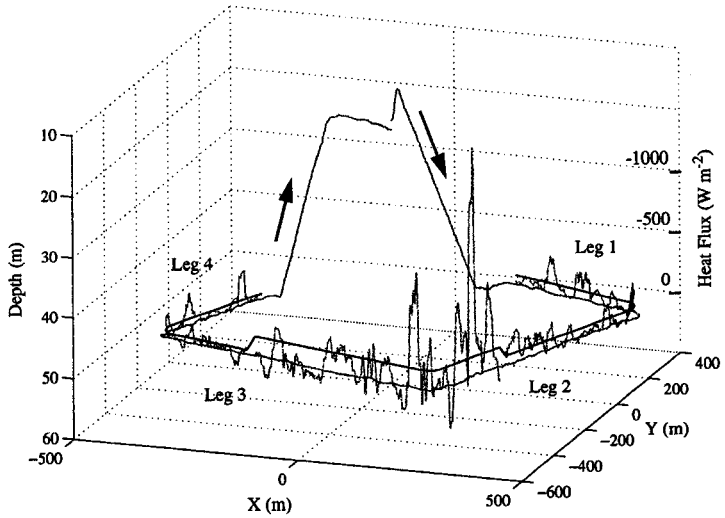

FIG. 11. Three-dimensional track of the ACTV during run 3 of ANZFLUX on 5 Aug 1994. The vehicle starts at about 15-m depth, dives to 50 m and executes a clockwise box pattern. The heat flux calculated from the ACTV motion and temperature probe is plotted in light gray, and the mean heat flux for three different regions is in black. The lead is located in the nearest corner, where there is a strong upward mean heat flux of -145 W m^{-2}. Leg 1 and the first part of leg 2 average -64 W m^{-2}, and the last part of leg 3 and leg 4 average -30 W m^{-2}. The heat flux has been smoothed with a 20-m running average.

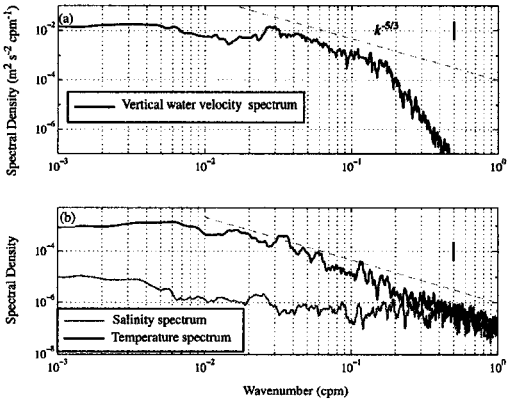

FIG. 12. (a) Vertical water velocity spectrum and (b) temperature and salinity spectra for ANZFLUX run 3, edges 2 and 3 of the box pattern (under the lead). The dashed gray lines obey the $k^{-5/3}$ law. The velocity and temperature spectra show a clear inertial subrange, but the salinity spectrum (gray solid line) does not. 95% confidence limits for the spectral estimation are shown.

smoother derived vertical water velocity. The average heat flux in three regions is also plotted.

Spectra of Kalman smoother-derived vertical water velocity, temperature, and salinity from ANZFLUX ACTV data are shown in Fig. 12. The spectrum of the vertical water velocity fluctuations varies as $k^{-5/3}$ in a broad inertial subrange between 0.03 and 0.2 cpm. The spectrum does not display the hump in energy between 0.02 and 0.1 cpm that is apparent in the LeadEx data (Fig. 9). This may be because the model best matches the 1994 vehicle configuration. As with the LeadEx data, narrow peaks in the vertical water velocity spectrum caused by acoustic transducer spikes in the depth data have been removed in Fig. 12. These spikes are uncorrelated with temperature and salinity, so they do not contribute to the mean heat or salt flux estimates. The temperature spectrum shows an inertial subrange for wavenumbers above about 0.02 cpm (Fig. 12b). The energy in salinity is low and nearly independent of the wavenumber, indicating that salinity flux is not a factor in the turbulence.

The horizontal profiles help illustrate boundary layer conditions (Fig. 13). Vertical water velocity is energetic everywhere. Large temperature spikes are present under the lead region while salinity is relatively quiet everywhere. The instantaneous heat flux is large upward in the lead region (-145 W m^{-2} average) and smaller upward away from the lead (-30 to -64 W m^{-2} average). The salt flux is quite small everywhere (0.13×10^{-5} kg s^{-1} m^{-2} average). Temperature and velocity are significantly correlated in the lead ($R = -0.21$), while the correlation between salinity and vertical water velocity is not significant in the lead ($R = 0.06$). Corre-

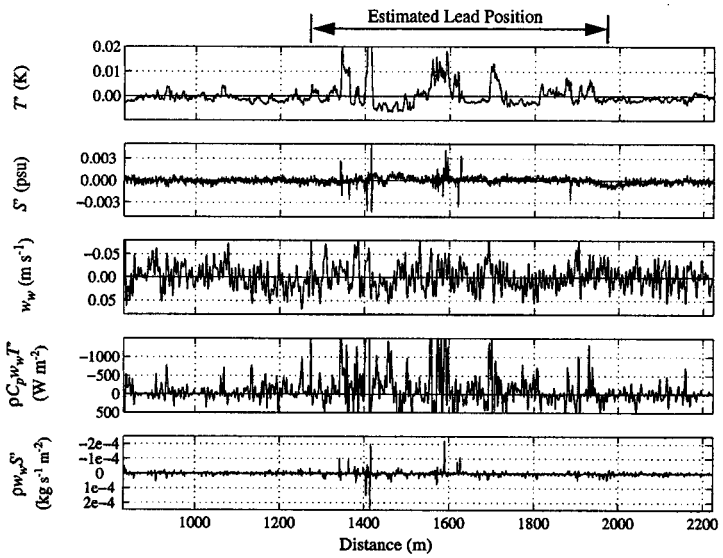

FIG. 13. ACTV data from run 3, legs 2 and 3 of ANZFLUX. Vehicle speed was 1.8 m s^{-1}; depth was 50 m, and mean ice–ocean relative velocity was 0.14 m s^{-1}. The data have been smoothed with a 1-m bin average. The mean heat flux between the 1300- and 2000-m marks (the central region of Fig. 11 and estimated lead position) is -145 W m^{-2}. The correlation coefficients in this region for temperature and salinity with velocity are -0.21 and 0.06, respectively. The latter is not significantly different from zero. All scales are the same as Fig. 1.

lation coefficient significance was tested using the same method described in section (3a).

There were no fixed masts or other measurements at the lead; the vehicle ran beyond the domain of most of the other ANZFLUX measurements. However, the ACTV results show good agreement with boundary layer conditions we expect on the basis of theory and bulk flux estimates at the surface. The heat flux from the open lead to the atmosphere was calculated to be 196 W m^{-2} upward using bulk formulas from Ruffieux et al. (1995; meteorological data courtesy of P. Guest 1999, personal communication). This is roughly in accord with our measurement of -145 W m^{-2} upward at 50 m below the surface of the lead. Heat flux to the atmosphere over the ice was about 20 W m^{-2} upward during this time (Guest 1998). The flux from the ocean to the ice was about 25 W m^{-2} (McPhee 1999) corresponding to the 30–64 W m^{-2} upward heat flux at 50 m estimated from the ACTV. Our interpretation is that the boundary layer was being well mixed by motion of the ice. Heat was being drawn upward from and through the mixed layer in rough proportion to the surface flux. Buoyancy-driven convection was not a factor under the lead because in spite of freezing air temperatures, the heat flux from the ocean was sufficient to prevent freezing of the lead surface. Indeed, the lead remained open throughout the drift (M. G. McPhee and T. Lehman, 1994, personal communication). The bottom melting suggested by the 5 W m^{-2} difference between ice–air and ocean–ice heat flux was too small to significantly stabilize the boundary layer at the time of the run. Because the salt flux was small and temperature had little effect on density near the freezing temperature, the buoyancy flux, $g\rho^{-1}\langle\rho' w_w\rangle$ was small and had little effect on the turbulence or circulation. For the observed fluxes, the ratio of the pressure gradient to the shear stress terms in the mean momentum equation, or lead number, L_0, (Morison et al. 1992) was much less than 1, meaning the shear stress dominated the buoyancy forces. This is in contrast to lead 3 of LeadEx for which L_0 was between 0.32 and 0.96 (MM98), and for which McPhee and Stanton (1996) showed that shear and buoyant production of turbulent kinetic energy were of the same order.

c. *Surface Heat Balance of the Arctic Ocean (SHEBA)*

As described by Moritz and Perovich (1996), the overarching goal of SHEBA was to improve our understanding of the local-scale processes in order to produce accurate global climate models and learn the role of the Arctic in global climate change. Our work focused on a summer lead study to measure the partitioning of solar insolation into edge melting, basal melting, and raised mixed layer temperatures. In contrast to the winter, the water input to the surface in the summer is fresher and therefore less dense than the ambient water because it consists of melted ice and snow. The fresh meltwater tends to suppress turbulence generated by wind and ice motion. On a fundamental level, the summer lead study will aid in understanding the stably stratified, horizontally varying boundary layer.

The role of the AMTV was to gather horizontal profiles of temperature and salinity variations in order to calculate heat and salt fluxes under varying surface conditions (observed by an upward-looking altimeter on the AMTV that measured the ice draft). The mode of operation was similar to that of LeadEx. The AMTV was lowered through a hole drilled a few meters from the lead edge. Four tracking hydrophones were lowered to 15-m depth in locations 50–100 m apart. A mast with a TIC of M. McPhee was placed in the water at the downstream edge of the lead. The mast was typically at the same or slightly shallower depth as the AMTV. Runs were planned such that the AMTV would cross the lead edge in the upstream and downstream directions, sampling water approximately in the path of the frame.

Forty-four runs adding up to 70 km of run track were gathered between 11 July and 7 August 1998. During this time, the station drifted with the ice pack from 78.1°N, 167°W to 78.4°N, 159°W. Data from 7 August (day 219) will be used here to discuss the performance and utility of the instrument and method because conditions were optimum for comparisons between the AMTV and TIC results: the lead upstream of the mast was over 1 km wide, the radiative fluxes were strong, the wind speed was 14 knots, and the ice–ocean relative velocity was 0.15 m s^{-1}. The AMTV went back and forth across the lead edge parallel or antiparallel to the relative surface current at about 5-m depth. The vehicle speed was approximately 1.1 m s^{-1}. Observations of vehicle depth, pitch rate, and pitch were used in estimating vertical water velocity, along with the parameters in Table 1. The heat flux was calculated using the Kalman smoother-estimated vertical water velocity and temperature fluctuations. Also on day 219, the TIC was placed a meter or so out from the ice edge with the instrument cluster at 5-m depth. It gathered temperature, conductivity, and vertical water velocity fluctuations over four 60–100-min periods that overlapped the 4 AMTV runs.

For each instrument, vertical water velocity spectra from data on 7 August 1998 are averaged and compared (Fig. 14). Four TIC spectra are averaged, and seven AMTV spectra from the under-lead segments are averaged. The estimate that uses the single-point water velocity model [state variables in Eq. (13) only] is flawed by 2 humps centered at 0.08 and 0.3 cpm. The excess energy at 0.3 cpm led us to believe that the gradient pitching phenomenon discussed earlier could be responsible. By accounting for the pitching moment due to water velocity variation across the vehicle length [see Eq. (19) and appendix B for a discussion of the model improvement], the new model produces an estimate without the broad peaks at 0.08 cpm and 0.3 cpm.

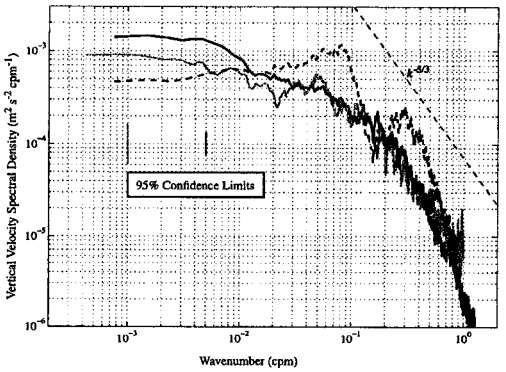

FIG. 14. Vertical water velocity spectra for data at 5-m depth on 7 Aug 1998 (day 219) at the SHEBA experiment site. The solid black line is an average of 7 spectra from different segments of 4 AMTV runs between 1300 and 2000 local time (8 h behind UTC). The dashed line shows the result before the model was modified to allow for different water velocities at the front and rear of the vehicle. The solid gray line is an average of the four TIC records taken during the same period downstream of the AMTV segments. Thin vertical bars show the 95% confidence intervals for the AMTV spectra (black) and the mast spectrum (gray).

The vertical water velocity spectrum estimated using the revised model shows excellent agreement with the turbulence mast spectrum, the 95% confidence intervals for the spectral estimation overlapping each other at all wavenumbers.

The Kalman smoother results shown in Fig. 14 are based on vehicle model coefficients derived from bench calibrations, general empirical data, and vehicle dynamics. In the course of debugging the Kalman smoother we examined the sensitivity of the smoother results to errors in vehicle model coefficients. A factor of 2 error in the model feedback coefficient for dive plane deflection relative to pitch error resulted in an estimated velocity spectrum about a factor of 4 less than the TIC spectra in a notch from 0.08 to 0.12 cpm. Moving the model hydrodynamic center of pressure on the hull 10 times farther forward and increasing the vehicle moment of inertia 25% resulted in a factor of 3 reduction in the velocity spectrum between 0.02 and 0.09 cpm. Increasing the model lift coefficient of the dive planes 50% decreased the velocity spectra a factor of 2 between 0.1 and 0.15 cpm while it raised the spectra a factor of 2 at wavenumbers below 0.01 cpm. Increasing the overall heave damping coefficient [Z_w, Eq. (B6)] 50% increased the velocity spectrum a factor of 2 below 0.06 cpm. Typically, coefficient errors of 50% resulted in localized, factor of 2–3 spectral errors. From this we suggest the Kalman smoothing approach is robust to model coefficient errors less than 10% and produces reasonable results for errors as high as 50%. It is noteworthy that the factor of 2 error in the dive plane feedback coefficient produced negligible change in the model step response shown in Fig. 5. Thus comparison of smoother-derived spectra with independently measured velocity spectra may be better than examining vehicle step responses for disclosing small errors in model parameters. This is probably because the energy levels revealed in the spectra are much finer than and rely on more data than typical step-response diagnostic vehicle maneuvers.

The utility of the Kalman smoother applied to the AMTV is best illustrated by examining a single run in detail. Run 2 was completed at 1600 local time on day 219 (0000 UTC day 220), and a portion of the data is shown in Fig. 15. The scale of each subplot is the same as Figs. 1 and 13 except the salinity deviation scale is 3 times larger, and the salt flux scale is half the size. The uppermost plot displays the ice draft measured by the acoustic altimeter on the AMTV along with temperature deviations. Salinity deviations are in the second panel. Both temperature and salinity fluctuations weaken within about 100 m downstream of the lead edge. The vertical water velocity [estimated using the improved model (B13)–(B14)] is the third panel down, and it is less energetic than the 2 winter lead experiments, likely due to the stable stratification. The magnitude and length scale of the velocity fluctuations appear to increase downstream of the lead, in contrast with the temperature and salinity fluctuations that become less energetic. The series of heat and salt flux across the lead and ice edge are shown in the fourth and fifth panels. Heat and salt fluxes are averaged over 100-m blocks: each average is shown as a solid line over the averaging domain. This averaging interval is chosen because it is likely to include several eddies of the dominant scale. A spectrum of vertical velocity plotted in an energy-preserving representation [kS vs $\log(k)$] shows a peak at a wavenumber around 0.1–0.2 cpm, so the size of the most energetic eddies was around 5–10 m. Fresh, warm water was being mixed downward in the lead, with a particularly strong event between the 1200- and 1300-m mark. For the entire lead segment shown, the average heat flux was 87 W m^{-2} (downward), and the average salt flux was -0.41×10^{-5} kg s^{-1} m^{-2} (upward). The 100-m block averages range from a heat flux of 36–214 W m^{-2} and a salt flux of -0.03 to -0.88×10^{-5} kg s^{-1} m^{-2}. The other lead segment (AMTV moving away from the ice) at 5-m depth for this run yields a heat flux of 92 W m^{-2}, and the salt flux is not available due to a nonlinear drift in conductivity. Under the ice, the first 100-m block indicates fluxes of the same magnitude and in the same direction as in the lead (87 W m^{-2} and -0.5×10^{-5} kg s^{-1} m^{-2}). The heat flux changed sign in the next downstream segment under the ice (-21 W m^{-2}), but the salt flux continued to be strongly upward (-1.1×10^{-5} kg s^{-1} m^{-2}). Average fluxes of 20 W m^{-2} and -0.9×10^{-5} kg s^{-1} m^{-2} were observed for the entire under-ice portion of Fig. 15. The role of the ice edge seems to be important, and has yet to be investigated satisfactorily.

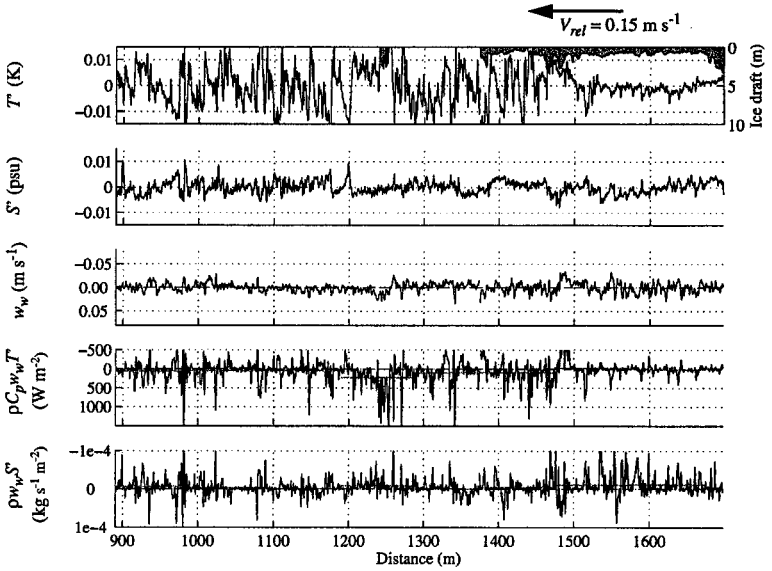

FIG. 15. AMTV data from run 2, legs 2 and 3 of SHEBA on 7 Aug 1998. Vehicle speed was 1.1 m s^{-1}, and depth was 5 m. Ice draft (from an acoustic altimeter) and mean ice–ocean relative velocity (0.15 m s^{-1}) are indicated. The data have been smoothed with a 1-m bin average. Mean fluxes in horizontal bins 100 m wide are indicated by the solid horizontal lines. In the lead the heat flux is 87 W m^{-2} (downward), and the salt flux is -0.41×10^{-5} kg s^{-1} m^{-2} (upward). Note the full scale on each plot is the same as Figs. 1 and 13, except for the salinity scale, which is 3 times larger here, and the salt flux scale, which is half the size.

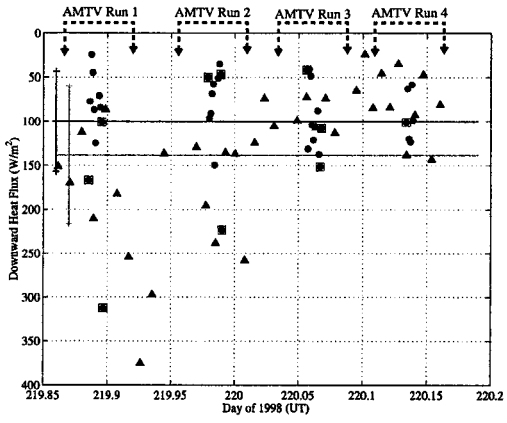

FIG. 16. Vertical heat flux at SHEBA on 7 Aug 1998 for the AMTV (circles) and the TIC (triangles). Each point represents a spatial average of 100 m (90 s of AMTV data or 11.1 min of TIC data), placed at the time of the center of the averaging interval. Only AMTV segments from in the lead upstream of the mast are plotted. AMTV blocks that are centered within 200 m of the ice edge are indicated by a box around the data point. The averages for the day are indicated by the horizontal lines, and the vertical bars indicate 1 std dev in either direction. The TIC averaged 138 W m^{-2} with a std dev of 78 W m^{-2} (gray) and the AMTV averaged 100 W m^{-2} with a std dev of 57 W m^{-2} (black).

The vertical heat and salt flux averages calculated from the TIC data are compared to the upstream averages estimated from the AMTV data in Fig. 16. Only AMTV data from under the lead are plotted. Each AMTV data point represents the heat flux averaged over a 100-m block of sampling, placed at the center time of the sampling. There are four groups of AMTV data points, each group corresponding to 1 of the 4 runs on day 219. Each TIC data block also represents 100 m, determined using the sampling time and ice drift speed (e.g., a 100-m mast data point consists of an 11.1-min average of the heat flux since the mast is moving at 0.15 m s^{-1} relative to the water), and is also placed at the center time of the block. The average for the entire day is shown as a horizontal line for the AMTV (100 W m^{-2}) and TIC (138 W m^{-2}), and a vertical bar for each indicates plus or minus 1 sample standard deviation of the block averages (57 or 78 W m^{-2}, respectively). Although the sample points from the AMTV and TIC may represent the same time, the two instruments were not in the same location, except when the vehicle crossed the lead edge. Flux averages from the mast show an increase from 90 to 375 W m^{-2} during the 2 h around AMTV run 1, followed by a decrease to values between 50 and 150 W m^{-2} over the next 6 h. The AMTV data also show the largest values near the beginning of the series, with the heat flux diminishing later in the day.

The first two AMTV runs show lower fluxes than the TIC, except when the AMTV was near the lead edge. Indeed, the largest AMTV fluxes were encountered near the downstream edge of the lead. (Boxes around the AMTV data points indicate blocks centered less than 200 m from the ice edge.) For example, the AMTV point just before the start of day 220 in Fig. 16 corresponds to the event less than 100 m upstream of the lead edge in Fig. 15. We hypothesize that the large fluxes at the lead edge were a natural consequence of an accumulation of radiative heating in the downstream direction in the upper layers of the open lead. This would result in the surface water temperature and turbulent heat flux being a maximum near the downstream lead edge. Later in the day, a steady state appears to have been reached with the AMTV data overlaying the TIC data nicely.

Despite the much larger temperature and salinity fluctuations, the vertical water velocity is actually weaker and of a higher-wavenumber character than either LeadEx or ANZFLUX. The melting pack ice is a source of freshwater that has a significant stabilizing effect and counters the shear-driven turbulence. The character of the turbulence at SHEBA is expected to be different for this reason. The turbulence likely becomes more energetic under the ice partly because the reduction of a stabilizing buoyancy flux allows shear to generate more turbulent energy. The reduced buoyancy flux under the ice also results in a larger characteristic eddy size.

4. Summary

Kalman smoothing of underwater vehicle motion leads to accurate estimates of vertical water velocity deviations. We have shown this with a comparison to the proven turbulence instrument cluster. Both the ACTV and AMTV vertical water velocity spectra show good agreement with simultaneous turbulence frame measurements, especially when one considers the limitations of the variability of the turbulent environments where the comparisons have been made. The heat (salt) fluxes were calculated directly using the Kalman smoother-derived vertical water velocity and temperature (salinity) deviations. These average fluxes from the AUVs compare well to flux estimates from the TIC. Although the ANZFLUX vehicle data were not accompanied by simultaneous TIC data, the heat and salt flux estimates are reasonable in direction and magnitude when put in the context of the surface heat fluxes.

The scales at which an AUV can gather turbulence data are on the order of a few meters to several hundred meters, at least for the AMTV. In contrast, the towed vehicle of Fleury and Lueck (1994) uses a shear probe to measure turbulent fluxes directly on scales of 25 cm–1 m. The submarine measurements of Yamazaki and Osborn (1993) include direct flux measurements in the range from 3 cm to 30 m using a shear probe, however, the operational constraints and expense of a submarine are severe drawbacks. The Kalman smoothing method can be applied to any AUV with commonplace sensors. The high-wavenumber limit of vertical water velocity estimation ultimately depends on the size of the vehicle and the sensitivity of the motion sensors.

Horizontal profiles of temperature, salinity, and vertical water velocity fluctuations are useful because they reveal the spatial variability of heat and salt flux under varied surface conditions. An AUV can take snapshots of horizontal variability at many depths without disturbing the surface. The Kalman smoothing technique greatly improves the utility of virtually any AUV because it measures turbulent vertical velocities at the energy-containing scales of ocean boundary layer turbulence. It does this with no sensors beyond the usual AUV guidance and control sensors. However, the best results are obtained when the highest quality sensors are used and pitch and pitch rate are measured in addition to depth. Perhaps the greatest benefit of the Kalman smoother method is that because it does not require comparison with fixed point measurements, it allows turbulence estimates that are robust to changing boundary layer conditions. We will use the Kalman smoothing method and the AMTV to provide essential insight to the surface heat budget calculation and under-ice boundary layer processes at SHEBA.

Acknowledgments. The authors would like to acknowledge the support of the Office of Naval Research (Grants N00014-96-1-5033 and N00014-98-1-0037) and the field support of the National Science Foundation Office of Polar Program's SHEBA project (OPP-9701831). Also thanks to Don Percival and Bradley Bell for acting as statistical consultants and Tim Peterson for his early advice. Special acknowledgments are given to Miles McPhee for providing instruments and data for all three experiments. Finally, we acknowledge Peter Guest for supplying the ANZFLUX meteorological data and Russ Light and David Morison for their critical roles in AMTV and TIC work during the SHEBA field experiment.

APPENDIX A

The Kalman Smoother

Kalman filtering and smoothing are algorithms that produce a minimum error estimate of the state of a system for which one has noisy measurements. We present the equations used for the Kalman smoother as described in Gelb, where a full derivation can be found (Gelb 1974, p. 156). On a terminology note, filtering means to estimate the state at the just-measured time using past data. Smoothing is to estimate the state using measurements before and after the time point of interest, maximizing the amount of information used.

The state estimated by the smoother is a linear combination of the states estimated by the forward and back-

ward filters. The forward filter equations are (4) and (5). The backward filter is similar to the forward filter except when solving the differential equations, one must integrate backward in time (see below). Obviously the backward filter can only be applied after all data has been collected from $t = 0$ to $t = T$. With forward- and backward-state estimates and error covariance matrices at each time step, an optimal smoother can be derived. The optimum linear combination of the forward and backward estimates is found by requiring that the smoother estimate is unbiased and that the smoother error covariance is minimized. The optimum smoother is given by the following equations (Gelb 1974, p. 158). The subscripts refer to smoothed, forward, and backward estimates, and the $\mathbf{P}$ matrices are defined similarly to $\mathbf{P}_f$:

$$\mathbf{P}_s^{-1} = \mathbf{P}_f^{-1} + \mathbf{P}_b^{-1} \tag{A1}$$

$$\mathbf{x}_s = \mathbf{P}_s(\mathbf{P}_f^{-1}\mathbf{x}_f + \mathbf{P}_b^{-1}\mathbf{x}_b). \tag{A2}$$

To integrate the backward filter, we define a new time variable $\tau = T - t$, and integrate from $\tau = 0$ to T. A problem arises when specifying the initial conditions for the backward estimate because at the end of the observation interval ($\tau = 0$), we only have that the forward estimates of both $\mathbf{x}$ and $\mathbf{P}$ must be the same as the smoothed estimates. This implies $\mathbf{P}_b^{-1}(\tau = 0) = \mathbf{0}_{\text{mxm}}$, where m is the length of the state vector. We do not have enough information to get an initial condition on $\mathbf{x}_b$, so we transform the backward filter by defining a new quantity, $\mathbf{s}$:

$$\mathbf{s} = \mathbf{P}_b^{-1}\mathbf{x}_b. \tag{A3}$$

Since $\mathbf{x}_b(\tau = 0)$ is finite, $s(\tau = 0) = 0$. Transforming the backward filter leads to the following equations that are integrated from $\tau = 0$ to T (Gelb 1974, p. 160):

$$\frac{d\mathbf{s}}{d\tau} = (\mathbf{F}^{\mathrm{T}} - \mathbf{P}_b^{-1}\mathbf{G}\mathbf{Q}\mathbf{G}^{\mathrm{T}})\mathbf{s} + \mathbf{H}^{\mathrm{T}}\mathbf{R}^{-1}\mathbf{z}$$

$$\mathbf{s}(\tau = 0) = \mathbf{0}_{\text{mx1}} \tag{A4}$$

$$\frac{d\mathbf{P}_b^{-1}}{d\tau} = \mathbf{P}_b^{-1}\mathbf{F} + \mathbf{F}^{\mathrm{T}}\mathbf{P}_b^{-1} - \mathbf{P}_b^{-1}\mathbf{G}\mathbf{Q}\mathbf{G}^{\mathrm{T}}\mathbf{P}_b^{-1} + \mathbf{H}^{\mathrm{T}}\mathbf{R}^{-1}\mathbf{H}$$

$$\mathbf{P}_b^{-1}(\tau = 0) = \mathbf{0}_{\text{mxm}}. \tag{A5}$$

The optimal linear smoother is then the set of Eqs. [(4), (5), (A1), (A2), (A4), (A5)]. The set of equations has been implemented in MATLAB in the continuous formulation. Once initial conditions and matrix values are set, an ODE solver is called every time step, utilizing new measurements and the just-estimated state vector. Code is available from the authors. Before calculating the smoothed estimates (A1) and (A2), one must reverse the time series of $\mathbf{s}$ and $\mathbf{P}_b^{-1}$ to convert them from functions of τ to functions of t. The smoother outputs time series for the complete state vector and for the error covariance matrix.

APPENDIX B

Hydrodynamic Model for an Autonomous Underwater Vehicle

a. Hydrodynamic forces and moments

To find the hydrodynamic coefficients in Eqs. (6) and (7), we rewrite the hydrodynamic force terms as the sum of the lift forces of all vehicle components (B1). Drag is not included because the component of the drag forces in the vertical direction is balanced by the propulsion system:

$$F_h = \sum_j \frac{\rho}{2} AV^2 C_{lj}(\alpha) \approx \frac{\rho}{2} AV^2 \sum_j C_{l\alpha_j}\alpha_j$$

$C_{lj}(\alpha)$ = dimensionless lift coefficient for vehicle component j

α_j = angle of attack of component j

$$C_{l\alpha_j} = \frac{\partial}{\partial\alpha} C_{lj}(\alpha). \tag{B1}$$

The dimensionless coefficients, C_{lj}, depend on Reynolds number, shape of the particular component, and most importantly angle of attack. For small angles of attack and with the other factors held constant, C_{lj} can be written as a power series in α_j, in which all but the linear term are neglected, as in Eq. (B1). The hydrodynamic moments can be expressed in a similar fashion:

TABLE B1. ACTV and AMTV lift and moment coefficients and distances of the center of pressure from the center of gravity. The source of each value is indicated.

	Lift coefficient $C_{l\alpha j}$		Moment coefficient $C_{m\alpha j}$		Center of pressure X_j (m)	
	ACTV	AMTV	ACTV	AMTV	ACTV	AMTV
Hull	0.5[a]	0.343[c]	1.01[a]	1.48[c]	0.226[c]	0.081[c]
Dive planes	0.8[b]	1.92[c]	0.372[d]	0.909[d]	0.764[c]	0.773[c]
Ring	1.2[b]	—	0.615[d]	—	0.843[c]	—

[a] Hoerner (1975).
[b] Brosseau and Ulbrich (1971).
[c] Bottaccini (1954).
[d] Calculated using other entries in the table [Eq. (B16)].
[e] Measured.

$$L_h = \sum_j \frac{\rho}{2} V^2 A L C_{mj}(\alpha) \approx \frac{\rho}{2} V^2 A L \sum_j C_{m\alpha j} \alpha_j. \quad \text{(B2)}$$

Formulas for lift and moment coefficients ($C_{l\alpha}$ and $C_{m\alpha}$) for many shapes have been determined, so we can regard them as known for each component composing the vehicle. Next, the angle of attack of each vehicle component is written in terms of the velocity of that component relative to the water at its center of pressure. The ACTV components are the hull, a ring protector around the propeller, and the dive planes while the AMTV lacks the ring:

$$\alpha_{\text{hull}} = \text{atan}\left(\frac{w_{\text{vrel}}}{u_v}\right) \approx \frac{w - w_w + V\theta}{V} \quad \text{(B3)}$$

$$\alpha_{\text{ring}} \approx \frac{w - w_w + V\theta + X_{\text{ring}} q}{V} \quad \text{(B4)}$$

$$\alpha_{\text{dp}} \approx \left(\frac{w - w_w + V\theta + X_{\text{dp}} q}{V} + \delta \text{p}\right). \quad \text{(B5)}$$

Substituting Eqs. (B1)–(B5) for the hydrodynamic terms in (6) and (7) and using (8) gives the following result:

$$\begin{aligned}
Z_w &= -\frac{1}{2}\rho V A (C_{l\alpha\text{hull}} + C_{l\alpha\text{ring}} + C_{l\alpha\text{dp}}) \\
Z_q &= -\frac{1}{2}\rho V A \\
&\quad \times \left(2\frac{\text{vol}}{A} k_1 + X_{\text{hull}} C_{l\alpha\text{hull}} + X_{\text{ring}} C_{l\alpha\text{ring}} + X_{\text{dp}} C_{l\alpha\text{dp}}\right) \\
M_w &= \frac{1}{2}\rho V A (L C_{m\alpha\text{hull}} - X_{\text{ring}} C_{l\alpha\text{ring}} - X_{\text{dp}} C_{l\alpha\text{dp}}) \\
M_q &= -\frac{1}{2}\rho V A (X_{\text{hull}}^2 C_{l\alpha\text{hull}} + X_{\text{ring}}^2 C_{l\alpha\text{ring}} + X_{\text{dp}}^2 C_{l\alpha\text{dp}}) \\
Z_{\text{dp}} &= -\frac{1}{2}\rho V^2 A C_{l\alpha\text{dp}} \\
M_{\text{dp}} &= -\frac{1}{2}\rho V^2 A L X_{\text{dp}} C_{l\alpha\text{dp}}.
\end{aligned} \quad \text{(B6)}$$

Unlike the other components, the effect of the hull on Z_q and M_q has not been incorporated through the angle of attack, α, in Eq. (B3), following Bottaccini (1954, p. 51).

b. Coefficients for vehicle body

For a symmetrical torpedo body, several authors have reported numerical values or empirical curves for lift coefficients (Nahon 1996; Bottaccini 1954). A good starting point is Eq. (B7) from Nahon (1996), although the ACTV required a number almost twice as large:

$$C_{l\alpha\text{hull}} = \frac{2(k_2 - k_1)A}{\text{vol}^{2/3}}. \quad \text{(B7)}$$

Bottaccini (1954, 25–28) suggests the following for lift and moment coefficients:

$$\begin{aligned}
C_{l\alpha\text{hull}} &= 0.005\left(\frac{L}{d}\right)^2 + 0.96\frac{\text{vol}}{AL} \\
&\quad + 5.71\left|0.835 - \frac{\text{vol}}{AL}\right| - 0.012\omega
\end{aligned} \quad \text{(B8)}$$

$$C_{m\alpha\text{hull}} = 2\frac{\text{vol}}{AL}(k_2 - k_1) - \frac{X_{\text{hull}} C_{l\alpha\text{hull}}}{L} \quad \text{(B9)}$$

$$X_{\text{hull}} = 0.78(L - X_B)(1 - 0.0111\omega). \quad \text{(B10)}$$

All symbols are defined in appendix C. The angle, ω, is the trailing-edge angle in degrees, formed by a vertical at the rear tip of the vehicle and a line joining the tip with the boundary of the tapered tail section. These equations are only to be used for a trailing-edge angle between 7° and 90°, a ratio of length to diameter between 5 and 13, and a prismatic coefficient (vol A^{-1} L^{-1}) between 0.7 and 0.95. Although valid for the AMTV, these requirements are not met by the ACTV, so the lift coefficient and moment coefficients for the vehicle body are obtained from Hoerner and Borst (1975, p. 19-6, their Fig. 8).

c. Coefficients for control surfaces

The lift coefficient for the dive planes is determined from Bottaccini (1954, pp. 17, 46):

$$C_{l\alpha\text{dp}} = \frac{S}{A_0}\left[1 - \left(\frac{d_T}{b}\right)^2\right]\frac{2\pi A_R}{(A_R^2 + 4)^{0.5} + 2}. \quad \text{(B11)}$$

Again, the parameters are defined in appendix C. The distance from the origin to the center of pressure of the fins is X_{dp}. The center of pressure is located at the quarter-chord point (the point one-fourth of the way from the leading edge of the fins on the root chord), and the moment coefficient follows [Eq. (B12)]:

$$C_{m\alpha\text{dp}} = \frac{X_{\text{dp}} C_{l\alpha\text{dp}}}{L}. \quad \text{(B12)}$$

The values for the lift coefficient of the ACTV control planes and the ring protector were obtained from a report on the predecessor vehicle prepared by Lockheed Missiles and Space Company (Brosseau and Ulbrich 1971). The distance from the origin to the center of pressure of the ring surrounding the ACTV propeller is measured. The moment coefficient for the ring is also determined with Eq. (B12). The numerical values for the ACTV and the AMTV are in Table B1.

d. Modification for a horizontal variation in water velocity over the vehicle length

The AMTV model is expanded by one dimension to include two separate vertical water velocities: one for

the back half of the vehicle, w_b, and one for the front half, w_f. The time–lag relationship between the 2 velocities is given in Eq. (19). Since the control surfaces are at the rear of the vehicle, the control surface angle of attack involves w_b instead of w_w in Eq. (B5). The hull angle of attack uses the average of the front and back water velocities in place of the single water velocity in Eq. (B3). We also include a pitching moment that acts on the hull due to a water velocity that could be different at the front and rear hull sections. This torque is due to the difference between the average water velocity acting on the center of gravity and the water velocities at the front and rear sections. The lift forces are centered at $\pm L/4$, and we assume a lift coefficient of unity. The new pitching moment and heave due to water velocity are Eqs. (B13)–(B14). The terms shown are in addition to those in Eqs. (6)–(7) that are not related to vertical water velocity:

$$m_T\dot{w} = \frac{1}{2}\rho VA\left[C_{l\alpha\text{hull}}\frac{w_f + w_b}{2} + C_{l\alpha\text{dp}}w_b\right] + \text{others} \tag{B13}$$

$$J_y\dot{q} = -\frac{1}{2}\rho VA\left[LC_{m\alpha\text{hull}}\frac{w_f + w_b}{2} + 2\left(\frac{L}{4}\right)\frac{w_f - w_b}{2} - X_{\text{dp}}C_{l\alpha\text{dp}}w_b\right] + \text{others}. \tag{B14}$$

Equations (11)–(13) change to reflect the new parameterization of vertical water velocity, as well as the PI control system:

$$\mathbf{x} = \begin{bmatrix} w_b \\ w_f \\ w \\ q \\ z \\ \theta \\ z_{\text{errint}} \\ \theta_{\text{errint}} \end{bmatrix} = \begin{bmatrix} \text{vertical water velocity—back section} \\ \text{vertical water velocity—front section} \\ \text{vertical vehicle velocity} \\ \text{pitch rate} \\ \text{vehicle depth} \\ \text{vehicle pitch} \\ \text{integrated depth error} \\ \text{integrated pitch error} \end{bmatrix} \tag{B15}$$

$$\mathbf{F} = \begin{bmatrix} -\frac{1}{\tau} & \frac{1.58}{\tau} & 0 & 0 & 0 & 0 & 0 & 0 \\ 0 & 0 & 0 & 0 & 0 & 0 & 0 & 0 \\ \frac{Z_{w_b}}{m_T} & \frac{Z_{w_f}}{m_T} & \frac{Z_w}{m_T} & \frac{Z_q + (m_L - m_T)V}{m_T} & \frac{-K_{zp}K_{\theta p}Z_{dp}}{m_T} & \frac{VZ_w + K_{\theta p}Z_{dp}}{m_T} & \frac{K_{zi}K_{\theta p}Z_{dp}}{m_T} & \frac{-K_{\theta i}Z_{dp}}{m_T} \\ \frac{M_{w_b}}{J_Y} & \frac{M_{w_f}}{J_Y} & \frac{M_w}{J_Y} & \frac{M_q}{J_y} & \frac{-K_{zp}K_{\theta p}M_{dp}}{J_y} & \frac{VM_w + K_{\theta p}M_{dp}}{J_y} & \frac{K_{zi}K_{\theta p}M_{dp}}{J_y} & \frac{-K_{\theta i}M_{dp}}{J_y} \\ 0 & 0 & 1 & 0 & 0 & 0 & 0 & 0 \\ 0 & 0 & 0 & 1 & 0 & 0 & 0 & 0 \\ 0 & 0 & 0 & 0 & -1 & 0 & 0 & 0 \\ 0 & 0 & 0 & 0 & K_{zp} & -1 & -K_{zi} & 0 \end{bmatrix} \tag{B16}$$

$$\mathbf{D}_1 = \begin{bmatrix} 0 \\ 0 \\ \frac{(mg - B)}{m_T} \\ \frac{BX_{\text{CB}}}{J_y} \\ 0 \\ 0 \\ 0 \\ 0 \end{bmatrix} \qquad \mathbf{D}_2 = z_{\text{goal}}\begin{bmatrix} 0 \\ 0 \\ K_{zp}K_{\theta p}\frac{Z_{dp}}{m_T} \\ K_{zp}K_{\theta p}\frac{M_{dp}}{J_y} \\ 0 \\ 0 \\ 1 \\ -K_{zp} \end{bmatrix} \qquad \mathbf{G} = \mathbf{I}_8. \tag{B17}$$

Four new coefficients are then defined based on Eqs. (B13)–(B14):

$$Z_{w_b} = \frac{1}{2}\rho VA\left(\frac{C_{l\alpha\text{hull}}}{2} + C_{l\alpha\text{dp}}\right) \qquad Z_{w_f} = \frac{1}{2}\rho VA\left(\frac{C_{l\alpha\text{hull}}}{2}\right)$$

$$M_{w_b} = -\frac{1}{2}\rho VA\left(\frac{LC_{m\alpha\text{hull}}}{2} - \frac{L}{4} - X_{\text{dp}}C_{l\alpha\text{dp}}\right)$$

$$M_{w_f} = -\frac{1}{2}\rho VA\left(\frac{LC_{m\alpha\text{hull}}}{2} + \frac{L}{4}\right). \tag{B18}$$

APPENDIX C

List of Symbols

All quantities are in the mks system, and angles are in radians, unless otherwise noted. Short descriptions and sign conventions are presented.

A = maximum cross-sectional area of vehicle
A_R = aspect ratio of dive planes = b^2/S
b = lateral span of planes
B = total buoyancy of body; positive quantity
C_p = specific heat of seawater at constant pressure
d = maximum vehicle body diameter
dp = angle of dive plane relative to body; positive means front edge up
d_T = average diameter of the body portion intersected by fins
g = gravitational constant
I_y = moment of inertia for a cylinder of uniformly distributed mass = $mL^2/12$;
J_y = apparent moment of inertia = $I_y(1 + k'\rho\text{vol}/m)$
k = horizontal wavenumber, in cycles per meter (cpm)
k_1 = $\alpha_0/(2 - \alpha_0)$
k_2 = $\beta_0/(2 - \beta_0)$
k' = $\dfrac{\beta_0 - \alpha_0}{\left(\dfrac{L^2 + d^2}{L^2 - d^2}\right)\left[2 - (\beta_0 - \alpha_0)\left(\dfrac{L^2 + d^2}{L^2 - d^2}\right)\right]}$
K_{zi} = proportionality constant between dive plane command and integrated depth error; positive
K_{zp} = proportionality constant between dive plane command and depth error; positive
$K_{\theta i}$ = proportionality constant between dive plane command and integrated pitch error; positive
$K_{\theta p}$ = proportionality constant between dive plane command and pitch error; positive
L = body length
m = mass of vehicle, including fluid in any flooded sections
m_L = apparent longitudinal mass = $m + k_1\rho\text{vol}$
m_T = apparent transverse mass = $m + k_2\rho\text{vol}$
q = vehicle pitch rate; positive means nose moving up
S = planform area of dive planes
S' = salinity deviations; detrended absolute salinity in psu
T' = temperature deviations; detrended absolute temperature
V = speed of vehicle relative to water
vol = geometric volume of vehicle
w = vertical vehicle velocity; positive downward; in earth-centered frame
w_b = vertical water velocity at back half of vehicle; in earth-centered frame
w_f = vertical water velocity at front half of vehicle; in earth-centered frame
w_v = vertical vehicle velocity; in vehicle-centered frame
$w_{v\text{rel}}$ = vertical vehicle velocity relative to water; in vehicle-centered frame
w_w = vertical water velocity; in earth-centered frame
X_B = location of center of buoyancy; distance behind nose of vehicle
X_{CB} = location of center of buoyancy; distance forward of center of gravity (CG)
z = depth of vehicle; positive downward; in earth-centered frame
z_v = depth of vehicle; positive downward; in vehicle-centered frame
α_0 = $\dfrac{2d^2}{L^2 - d^2} \times \left\{\dfrac{L}{(L^2 - d^2)^{0.5}} \ln\left[\left(\dfrac{d}{L - (L^2 - d^2)^{0.5}}\right) - 1\right]\right\}$
β_0 = $\dfrac{L^2}{L^2 - d^2} \times \left\{1 - \dfrac{d^2}{L(L^2 - d^2)^{0.5}} \ln\left[\dfrac{d}{L - (L^2 - d^2)^{0.5}}\right]\right\}$
θ = pitch of vehicle; positive means nose up
ρ = mean seawater density
ω = trailing-edge angle for vehicle tail section in degrees (zero deg for body with no tapered tail)

REFERENCES

Bartlett, M. C., and T. L. Schlachter, 1967: Fundamental principles of torpedo dynamics. U.S. Navy Mine Defense Laboratory Tech. Note 134, 97 pp.

Bottaccini, M. R., 1954: The stability coefficients of standard torpedoes. U.S. Naval Ordnance Test Station 909, NAVORD Rep. 3346, 94 pp.

Brosseau, J. A., and H. G. Ulbrich, 1971: Hydrodynamic analysis and test of the APL target vehicle. Lockheed Missiles and Space Company Rep. D244667, 45 pp.

Etkin, B., 1972: *Dynamics of Atmospheric Flight.* Wiley, 579 pp.

Fleury, M., and R. G. Lueck, 1994: Direct heat flux estimates using a towed vehicle. *J. Phys. Oceanogr.*, **24,** 801–818.

Gelb, A., Ed.,1974: *Applied Optimal Estimation.* The MIT Press, 374 pp.

Guest, R. S., 1998: Surface longwave radiation conditions in the eastern Weddell Sea during winter. *J. Geophys. Res.*, **103** (C13), 30 761–30 771.

Hoerner, S. F., and H. V. Borst, 1975: *Fluid-Dynamic Lift.* L. A. Hoerner, 502 pp.

Jenkins, G. M., and D. G. Watts, 1968: *Spectral Analysis and Its Applications.* Holden-Day, 525 pp.

LeadEx Group, 1993: The LeadEx Experiment. *Eos, Trans. Amer. Geophys. Union,* **74,** 393, 396–397.

Levine, E. R., and R. G. Lueck, 1999: Turbulence measurement from an autonomous underwater vehicle. *J. Atmos. Oceanic Technol.,* **16,** 1533–1544.

Lueck, R. G., and F. Wolk, 1999: An efficient method for determining the significance of covariance estimates. *J. Atmos. Oceanic Technol.,* **16,** 773–775.

McPhee, M. G., 1994: On the turbulent mixing length in the oceanic boundary layer. *J. Phys. Oceanogr.,* **24,** 2014–2031.

——, and T. P. Stanton, 1996: Turbulence in the statically unstable oceanic boundary layer under Arctic leads. *J. Geophys. Res.,* **101** (C3), 6409–6428.

——, and Coauthors, 1996: The Antarctic Zone Flux Experiment. *Bull. Amer. Meteor. Soc.,* **77,** 1221–1232.

Morison, J. H., and M. G. McPhee, 1998: Lead convection measured with an autonomous underwater vehicle. *J. Geophys. Res.,* **103** (C2), 3257–3281.

——, ——, T. B. Curtin, and C. A. Paulson, 1992: The oceanography of winter leads. *J. Geophys. Res.,* **97** (C7), 11 199–11 218.

Moritz, R. E., and D. K. Perovich, Eds.,1996: Surface heat budget of the Arctic Ocean Science Plan. ARCSS/OAII Rep. 5, 64 pp. [Available from Polar Science Center, Applied Physics Lab, 1013 NE 40th St., Seattle, WA 98105.]

Nahon, M., 1996: A simplified dynamics model for autonomous underwater vehicles. *Proc. 1996 Symp. on Autonomous Underwater Vehicle Technology,* New York, NY, IEEE, 373–379.

Osborn, T. R., and C. S. Cox, 1972: Oceanic fine structure. *Geophys. Fluid Dyn.,* **3,** 321–345.

Percival, D. B., and A. T. Walden, 1993: *Spectral Analysis for Physical Applications: Multitaper and Conventional Univariate Techniques.* Cambridge University Press, 583 pp.

Ruffieux, D., P. O. G. Persson, C. W. Fairall, and D. E. Wolfe, 1995: Ice pack and lead surface energy budgets during LEADEX 1992. *J. Geophys. Rev.,* **100** (C3), 4593–4612.

Wettlaufer, J. S., M. Grae-Worster, and H. E. Huppert, 2000: Solidification of leads: Theory, experiment, and field observations. *J. Geophys. Res.,* **105** (C1), 1123–1134.

Yamazaki, H., and T. R. Osborn, 1993: Direct estimation of heat flux in a seasonal thermocline. *J. Phys. Oceanogr.,* **23,** 503–516.

VITA

Daniel Reiner Hayes

Born:	December 10, 1973
Parents:	Claude W. Hayes
	Harriet M. Hayes
Siblings:	Heidi C. Hayes
	Timothy C. Hayes
Spouse:	Sophia C. Hayes
Children:	Constantinos C. Hayes
High School:	Corning, Iowa
B.A. in Physics and Math:	Luther College, 1996
M.S. in Oceanography:	University of Washington, 1999
Ph.D. in Oceanography:	University of Washington, 2003